Design and Simulation of Electron and Hole Transport Layer for Lead-Free Perovskite Solar Cell Application

A Thesis

Submitted in fulfilment of the requirement for the award of the degree

of

DOCTOR OF PHILOSOPHY

in

Electronics and Communication Engineering

Submitted by

NEELIMA SINGH

Reg. No. 901706018

Under the Supervision of

Dr. Mohit Agarwal
Assistant Professor
TIET, Patiala (Punjab), India

Dr. Alpana Agarwal
Professor and Head of Department
TIET, Patiala (Punjab), India

THAPAR INSTITUTE
OF ENGINEERING & TECHNOLOGY
(Deemed to be University)

Electronics and Communication Engineering Department

Thapar Institute of Engineering and Technology, Patiala-147001

September-2021

CERTIFICATE

I, Neelima Singh hereby declare that the thesis entitled "Design and Simulation of Electron and Hole Transport Layer for Lead-Free Perovskite Solar Cell Application," which is being submitted by me to the Department of Electronics and Communication Engineering, Thapar Institute of Engineering and Technology, Patiala for the award of the degree of Doctor of Philosophy for the research work carried out under the supervision of Dr. Alpana Agarwal and Dr. Mohit Agarwal. The content present in the thesis does not contain any content which is previously published or written by any other person exempting the reference are provided in the text. The result presented in the thesis has not been submitted in part or full to any other institute or university for the award of the degree.

Date 15/9/21

Neelima Singh

Neelima Singh

(Reg. No. 901706018)

This is to certify that the above statement made by the candidate is correct and true to the best of our knowledge and belief. She has worked under our supervision and fulfilled the criteria for the submission of this thesis.

Dr. Mohit Agarwal
Assistant Professor, ECED
T.I.E.T., Patiala-147001, India

Dr. Alpana Agarwal
Professor and Head, ECED
T.I.E.T., Patiala-147001, India

ACKNOWLEDGEMENT

Foremost, I owe my sincere thanks to the Thapar Institute of Engineering and Technology for providing me an opportunity to become a part of this most satisfactory journey of my life. Further, I would like to thank those individuals without whom this journey would not be possible.

I express my heartiest gratitude to my respected supervisors, "**Dr. Alpana Agarwal**" and "**Dr. Mohit Agarwal**" for sharing their immense knowledge and support, to continue my journey with much confidence. I always feel blessed for getting an opportunity to work under their supervision. With a lot of patience, they consistently listened to my all problems and provide extremely valuable suggestions and motivation to overcome the problem in the most effective way. I always admire them for their humble attitude and for their precious time due to which the work is completed in a more effective manner.

Further, I would like to extend my gratitude towards my respected doctoral committee members, Dr. Manu Bansal, Dr. Sumit Vyas, and Dr. B.C. Mohanty for providing their continuous support and valuable suggestion to effectively enhance the quality of the research work. In addition, I would also extend my token of appreciation to the numerous reviewers for their valuable suggestions that led to the improvement in the work presented. Moreover, I wish to express my appreciation to Prof. (Dr.) Marc Burgelman and his research team from the University of Ghent, Belgium for providing access of the SCAPS 1D software.

Finally, I would like to express my sincere thanks to my parents Dr. Abhimanyu Singh and Mrs. Pushpa Chauhan, my siblings Mr. Aurnabh Singh, Mrs. Arunima Singh, Mrs. Shalini Singh for their continuous support and encouragement. I would also like to thanks to friends Ms. Ruby Garg, Mrs. Kanika Nagpal and Mr. Vishal Narula and my respected seniors Ms. Deepa Negi, Ms. Kanwarpreet Kaur, Ms. Navneet Kaur, Mr. Hari Shankar, Mr. Amit Kumar, my dearest friends Mrs. Sristi Maurya, Mr. Sumit Kumar, Mr. Ashwani Yadav, Ms. Anuradha Venbanshee, and Ms. Sugam Preeti who continuously stood for me during my even and odds for the entire course of this research.

Neelima Singh

Thapar Institute of Engineering and Technology

Patiala, Punjab, India.

TABLE OF CONTENTS

ABSTRACT

The perovskite solar cells are an emerging photovoltaic technology as it reaches 25.5% efficiency within a decade. Due to this rapid advancement researchers have developed various perovskite absorber layers, charge transport layers, transparent conducting oxides and metal contacts. However, it is quite complicated to fabricate numerous combinations of these layers and hence the simulation is an efficient way to analyse the best possible combination which can result in higher device performance. In the present thesis work, the numerical simulation of lead-free perovskite solar cells is performed using SCAPS 1D software.

The current study brings forth the numerical simulation of various lead-free perovskite alternatives having narrow and wide bandgap configurations. For the narrow bandgap configuration, the $FA_{0.75}MA_{0.25}Sn_{0.25}$ $Ge_{0.5}I_3$ and $CsSnGeI_3$ based perovskite layers are considered. However, for the wide bandgap application, the $CH_3NH_3GeI_3$ based perovskite layer is considered. The perovskite solar cells using these layers are optimized based on charge transport layers, perovskite absorber layer thickness, perovskite absorber defect density and their energy band alignment with respect to the contacts. To investigate the effect of charge transport layers (*i.e.,* hole transport layer and electron transport layer), the work shows that the correlation of V_{OC} with the built-in potential (V_{bi}). The results disclosed that to attain better V_{OC} and PV performance, the device should exhibit the better V_{bi} and proper band alignment that allows the efficient facilitation of charge carriers, along with good charge carrier mobility. Thus, it is suggested that for the proper transport of electrons, the conduction band minimum of the electron transport layer (ETL) must lie below the conduction band minimum of the perovskite layer. Similarly, in the case of hole transport, the valence band maximum of the hole transport layer must lie above that of the perovskite layer. Thus, the simulation study mainly suggests the possible combination of the ETL and HTL alternatives for less explored perovskite solar cell configuration.

Further, it is found that to optimize the solar cells the thickness of the absorber layer should be carefully chosen. Also, the study shows that the defects of the absorber layer exhibit a significant impact on the device performance as the higher defect led to the creation of more recombination centres and thus reduces the overall PV performance. Thus, it is obtained that the defect density of the perovskite layers should not be greater than 1×10^{14} cm^{-3}.

The front and the back contact metal work functions depict a crucial role in determining the device efficiency. If the back metal work function is less than 5 eV it provides a barrier for the charge carrier however high metal work function saturates its PCE and thus 5 eV is recommended. In addition, for the front contact, it is suggested to have the work function should be below 4.4 eV.

After, optimizing the standalone configuration, the study is extended to the lead-free all-perovskite multijunction solar cell configuration. This present work proposes a novel realization of ($CH_3NH_3GeI_3$-$CsSnGeI_3$) and ($CH_3NH_3GeI_3$-$FA_{0.75}MA_{0.25}Sn_{0.25}Ge_{0.5}I_3$ ($FAMASnGeI_3$)) for the first time. It is obtained that by proper control of the perovskite layer thickness and defect density, by selecting the suitable charge transport layer, the PV performance of multijunction solar cells can be improved. In addition, the simulated multijunction solar cell depicts the device efficiency greater than 26% which is considered as a significant improvement in the field of the lead-free all-perovskite multijunction solar cell. The study and analysis provide a significant insight to the researchers fabricating the highly efficient lead-free all-perovskite multijunction solar cells.

Furthermore, the present study is extended towards the realization of lead–free double–perovskite ($Cs_2AgBi_{0.75}Sb_{0.25}Br_6$, *i.e.,* mixed antimony bismuth halide double-perovskite) solar cells. The double-perovskite solar cell is optimized with respect to their charge transport layer and it has been found that the device PV performance improves significantly. However, the proposed lead-free double perovskite solar cell depicts the device efficiency up to 18.18 % which is considered as a significant alternative for the lead-free perovskite solar cell along with the satisfactory device photovoltaic performance.

All the proposed structures for perovskite solar cell configuration are novel structures and provide better parameters in most cases when compared to the latest existing perovskite structures.

LIST OF FIGURES

LIST OF TABLES

LIST OF ABBREVIATIONS

Abbreviation	Full Name
2T	Two terminals
4T	Four terminals
ALD	Atomic layer deposition
Al_2O_3	Aluminum oxide
A.M.1.5D	Air mass 1.5 direct
A.M.1.5G	Air mass 1.5 global
APMJSC	All-perovskite multijunction solar cell
APTSC	All-perovskite tandem solar cell
C60	Buckminsterfullerene
$CaTiO_3$	Calcium titanate
CB	Conduction band
CBO	Conduction band offset
CBM	Conduction band minimum
CdS	Cadmium sulphide
CdTe	Cadmium telluride
$Cd_{1-x}Zn_xS$	Cadmium zinc sulphide
$CH_3NH_3GeI_3$	Methyl ammonium germanium iodide
$CH_3NH_3PbI_3$	Methyl ammonium lead iodide
$CH_3NH_3PbI_{3-x}Cl_x$	Methyl ammonium lead mixed halide
$CH_3NH_3SnI_3$	Methyl ammonium tin iodide
CIGS	Copper indium gallium diselenide
Cs-AFM	Current sensing atomic force microscopy
C-Si	Crystalline silicon
$Cs_2AgBiBr_6$	Cesium silver bismuth bromide double perovskite
$Cs_2AgBi\ Sb_{0.25}\ Br_6$	Cesium based mixed antimony-bismuth halide double perovskite
$CsGeI_3$	Cesium germanium triiodide
$CsSnGeI_3$	Cesium tin germanium iodide
$CsSnI_3$	Cesium tin triiodide
CTL	Charge transport layer
$CuAlO_2$	Copper aluminate
$CuGaO_2$	Copper gallium oxide
CuI	Copper(I) iodide
Cu_2O	Copper(I)oxide

$CuSbS_2$	Copper antimony sulphide
CuSCN	Copper(I) thiocyanate
CZTS	Copper zinc tin sulphide
CZTSe	$Cu_2ZnSnSe_4$ (Kesterite)
DFT	Density functional theory
DMA	Dimethylammonium
DMF	Dimethylformamide
DMSO	Dimethyl sulfoxide
DOS	Density of states
EBD	Energy band diagram
ETL/ETM	Electron transport layer/electron transport material
E_{C_ETL}	Conduction band minimum of ETL
E_{C_PVK}	Conduction band minimum of perovskite layer
EDS	Energy dispersive X-ray spectroscopy
E_{V_HTL}	Valance band maximum of hole transport layer
E_{V_PVK}	Valence band maximum of perovskite layer
$E_{C\_PVK/ETL}$	Conduction band energy level between ETL and perovskite
$E_{C\_PVK/HTL}$	Conduction band energy level between perovskite and hole transport layer
FA	Formamidinium
$FAGeI_3$	Formamidinium germanium triiodide
FAI	Formamidinium iodide
$FAMASnGeI_3$	$FA_{0.75}MA_{0.25}SnGe_{0.75}I_3$
$FAPbI_3$	Formamidinium lead iodide
$(FAPbI3)_{1-x}(MAPbBr_3)_x$	Formamidinium methylammonium lead iodide bromide
$FASnI_3$	Formamidinium tin triiodide
FF	Fill factor
FTO	Fluorine doped tin oxide
GaAs	Gallium arsenide
GaInP	Gallium indium phosphide
GuaSCN	Guanidinium thiocyanate
GZO	Gallium doped zinc oxide
HOMO	Highest occupied molecular level
HTL/HTM	Hole transport layer/material
IGZO	Indium gallium zinc oxide
I-V	Current-voltage

ITO	Indium tin oxide
J_{SC}	Short circuit current density
J-V	Current density -voltage
KCL	Kirchhoff's current law
Li-TFSi	Lithium bis (trifluoromethylsulphonyl)imide
LUMO	Lowest unoccupied molecular level
$MAGeBr_3$	Methylammonium germanium tribromide
$MAGeCl_3$	Methylammonium germanium trichloride
$MAPbBr_3$	Methylammonium lead tribromide
$MAPbI_3$	Methylammonium lead triiodide
$MASnBr_3$	Methylammonium tin bromide
mp-TiO_2	Mesoporous titanium oxide
NiO	Nickel(II)oxide
P3HT	Poly(3-hexythiophene)
Pb	Lead
Pb-free	Lead-free
PCBM	Phenyl-C61-butyric acid methyl easter
PCE	Power conversion efficiency
PEDOT:PSS	Poly(3,4-ethyelenedioxythiophene) polystyrene sulfonate
PEI	Poly(ethyleneimine)
PSC	Perovskite solar cell
PV	Photovoltaics
PVK	Perovskite
PYS	Photo yield spectroscopy
QE	Quantum efficiency
SCAPS 1D	Solar cell capacitance simulator
Si	Silicon
a-Si	Amorphous silicon
a-Si:H	Hydrogenated amorphous silicon
SnI_2	Tin iodide
SnO_2	Tin oxide
SpiroOMeTAD	2,2',7,7'-tetrakis (N,N-di(4-methoxyphenyl)amino-9,9'-spirobiflourine
SRH	Shockley-read-hall
SRV	Surface recombination velocity
STO	Strontium tin oxide

SWCNT	Single walled carbon nanotube
TA	Transient absorption
t-BP	4-tert-butylpyridine
TCAD	Technology computer aided design
TCNQ	Tetracyanoquinodimethane
TCO	Transparent conductive oxide
THz	Tera hertz
TiO_2	Titanium oxide
UV	Ultraviolet
V_{bi}	Built-in voltage
VBM	Valence band maximum
VBO	Valence band offset
V_{OC}	Open circuit voltage
WS_2	Tungsten disulfide
XPS	X-ray photoelectron spectroscopy
XRD	X-ray diffraction
ZnO	Zinc oxide
ZnOS	Zinc oxysulfide
ZnSe	Zinc selenide
ZnTe	Zinc telluride

GLOSSARY OF SYMBOLS

Symbol	Full Name
A_e/A_h	Capture cross section area of electron/hole
c	Speed of light
D_n/D_p	Diffusion constant for electron/hole
E	Electric field
E_a	Activation energy
E_g	Band gap
eV	Electron volt
G	Generation rate
h	Plank's constant
I	Total current
I_D	Diode current
I_L	Light generated current
I_O	Saturation current
I_{SH}	Shunt current
J_n/J_p	Current density of electron and holes
K	Boltzmann constant
λ	Wavelength
η	Power conversion efficiency
η'	Diode ideality factor
N_A	Acceptor density
N_C	Conduction band density of states
N_D	Donor density
N_V	Valence band density of states
P_{in}	Input power
P_{MPP}	Maximum power point
P_t	Total power
q	Electronic charge (1.6×10^{-19} C)
r_A, r_B, r_X	Radius of A, B and X element
R_s	Series resistance
R_{SH}	Shunt resistance
T	Temperature
t	Tolerance factor
τ_p,τ_n	Lifetime of hole and electron

μ	Octahedral factor
μ_n/ μ_p	Mobility of electron/hole
U_p,U_n	Recombination rate for electron and holes
σ	Capture cross section of charge carriers by defect level
Φ_{BC}	Work function of back contact
Φ_{FC}	Work function of front contact
ν	Frequency of light
V_{SH}	Shunt voltage
V_D	Diode voltage
$v_{th,e}$,v_{thh}	Thermal velocity of electron and hole
χ	Electron affinity
χ_{ETL}	Electron affinity of electron transport layer

CHAPTER 1

1.1 Introduction

To meet the burgeoning energy demand, the fossil resources are extensively utilized. The limited availability of fossil resources and their serious detrimental impact on the environment diverted researcher's attention towards the exploration of a renewable energy alternatives. There are various renewable energy resources available such as wind energy, hydroelectric energy, biomass, solar energy, geothermal energy *etc*. In the midst of these alternatives, solar energy manifests the promising substitute for the application of clean, low cost, sustainable renewable energy resources. The major benefit of solar energy that it does not produce any pollutants and byproducts which are harmful to environment. In 1839, to extract the electricity from the solar energy, Sir Edmond Becquerel's experiment consisting of two electrodes present in an electrolyte solution were exposed to the sunlight resulted to the formation of electricity[1].

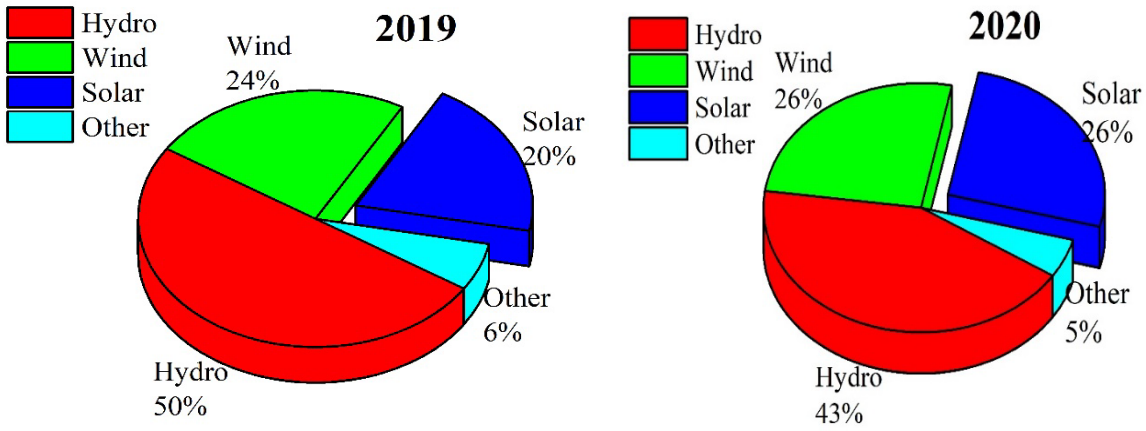

Fig. 1.1. Rapid annual enhancement of energy resources for solar cell technology development [2][3]

The phenomenon which converts the sunlight energy to an electricity is termed as photovoltaic effect which unlocks the opportunity towards the development of solar cells[4]. The dependance of the renewable energy resources gains a huge attention among researchers. Fig. 1.1 exhibits the rapid annual enhancement *i.e.,* a 6 % increment on the

production of renewable energy [2][3], which exhibits the urge for the demand and exploration of solar cells for technological development.

1.2 Working Principle of Solar Cell

Solar cell is one of the semiconducting devices that works on the principle of conversion of electricity directly from light energy came from the sun as an input source. The device schematic of solar cell is shown in Fig**.** 1.2[5].

The principle of photovoltaic is divided into three parts

(a) Absorption of photons

(b) Separation of charge carriers

(c) Collection of carriers across the electrode.

When the light falls onto the solar cell absorbing material, the photons get absorbed which generates the electron and hole pair inside the device. The absorption of particular energy photons depends on the bandgap of absorbing material. Due to the diffusion of charge carriers, the donor ions and acceptor ions are present at the junction of solar cell. The presence of these charge carriers lead to the creation of electric field inside the device. This electric field is responsible for the creation of drift current and the electrons and holes are separated at n and p region. After separation of the charge carriers the charge carriers get collected towards the electrode as shown in Fig. 1.3.

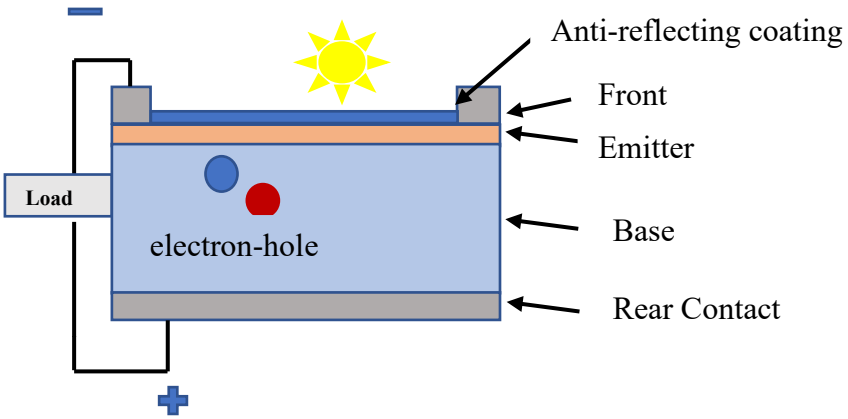

Fig. 1.2. Schematic of p-n junction solar cell

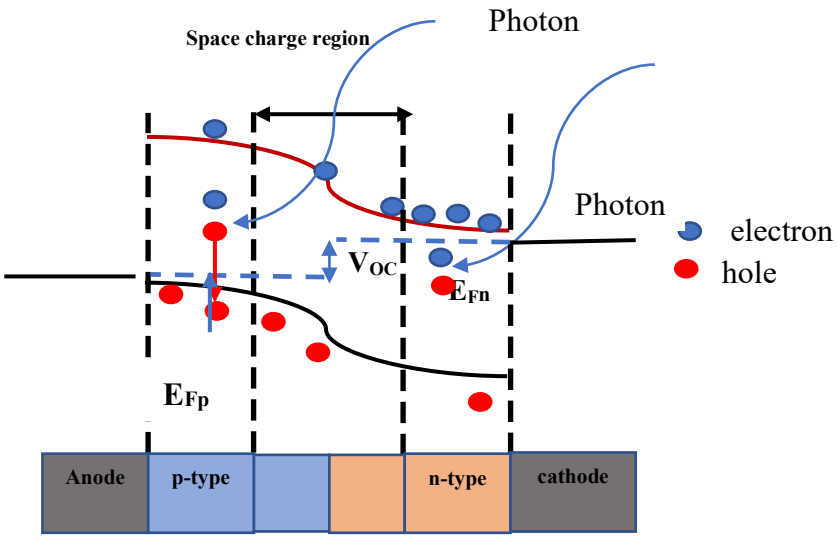

Fig. 1.3. Working mechanism of P-N junction solar cell

1.3 Fundamental Parameters of Solar Cell

The fundamental parameters associated with the solar cell is described.

1.3.1 Open Circuit Voltage (V_{OC})

The important parameter of the solar cell is open circuit voltage (V_{OC}) and it is attained at the condition of infinite load resistance *i.e.,* no external load is connected to the solar cell. The V_{OC} is defined as the maximum voltage attained by the solar cell. The open circuit voltage can be determined from the I-V graph of the solar cell, as depicted in Fig**.** 1.4. It is the intercept of the I-V curve at voltage axis. The equation of open circuit voltage is given in Eq. 1.1.

$$V_{OC} = \frac{KT}{q}\, ln\, (\frac{I_L}{I_o} + 1) \qquad \textbf{Eq. 1.1}$$

where,

K is the Boltzmann constant, I_L is the current measured in light condition, I_0 is the dark reverse current

Also, the saturation current depends on the amount of recombination of charge carries in the device.

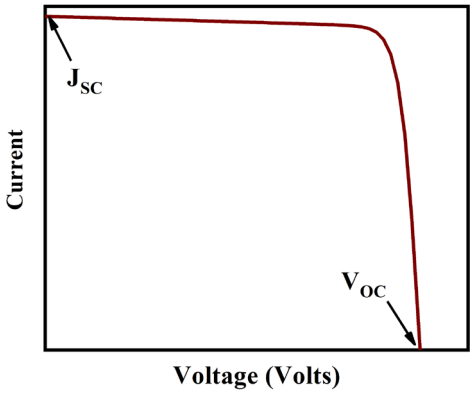

Fig. 1.4. The current voltage characteristics of solar cell

1.3.2 Short Circuit Current (I_{SC})

The short circuit current is defined as the maximum current when the voltage across the device is zero as shown in Fig. 1.4. The short circuit current density depends on the incident photons number, incident light spectrum, area of solar cell, collection probability as well as optical properties of solar cell. To maximize the short circuit current density, light absorption should be high. Also, the thickness of the absorber layer should be thick enough, so that it can absorb photons without recombining the photogenerated charge carriers.

1.3.3 Fill Factor (FF)

The fill factor defines the squareness of the I-V curve which further decides the quality of the solar cell and is obtained by dividing the maximum power point (P_{MPP}) to the product of V_{OC} and J_{SC} of the solar cell as depicted in Fig. 1.5. However, at the condition of open circuit voltage and short circuit current density, no power is generated from the solar cell. The maximum power is attained at the point where the product of I and V is maximum. To realize the good solar cell, the FF should be high.

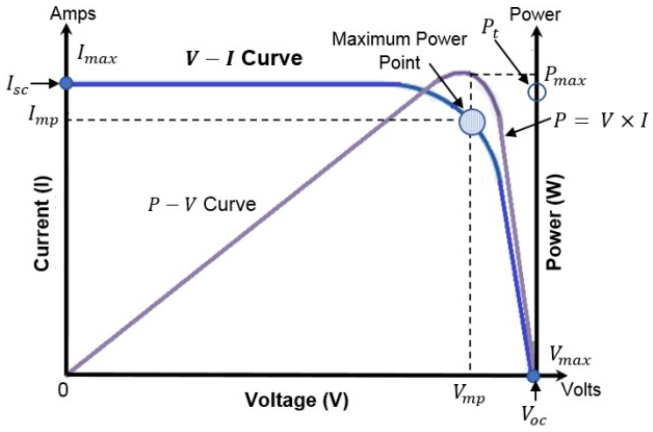

Fig. 1.5. The I-V curve shows the fill factor of solar cell

1.3.4 Power Conversion Efficiency (PCE)

The other important parameter of the solar cell is defined by the percentage of power generated from the solar cell to the incident power of the solar cell and called as a PCE. It is the ratio between the output power from the solar cell to the power obtained from the sun in the form of input energy as shown in Eq. 1.2.

$$PCE = \frac{P_{max}}{P_{in}} = \frac{V_{oc} J_{sc}\, FF}{P_{in}} \qquad \textbf{Eq. 1.2}$$

The PCE mainly depends on the incident solar cell light intensity and the working temperature of solar cell.

1.3.5 Quantum Efficiency (QE)

To find out the quantum response of the solar cell, the ratio of the number of photons that are collected at the solar cell to the total number of the incident photons on the solar cell is defined by the quantum efficiency. The QE is either represented in terms of photon wavelength or photon energy as shown in Fig. 1.6[6]. In an ideal case, if all the incident photons of certain wavelengths are get absorbed then the resulted QE is unity.

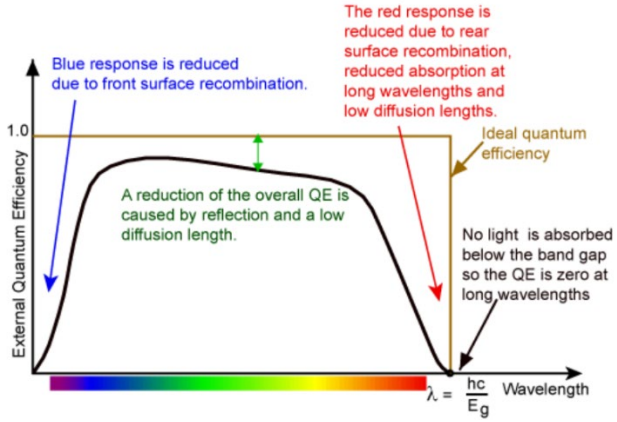

Fig. 1.6. Quantum efficiency of solar cell [6]

However, the QE of those photons having energy less than the bandgap energy is zero. In the condition of unity QE, the resulted QE having unity value is shown in Fig. 1.6. However, due to the recombination losses, the quantum efficiency curve variates from the unity curve. As explained in Fig. 1.6. due to the front surface passivation effect, the generated carriers near the surface get affected and thus reduces the quantum efficiency. As the wavelength increases, the smaller energy photons will not get absorbed by the device and thus the overall response reduces as shown in Fig. 1.6.

1.3.6 Series Resistance (Rs)

The series resistance of the solar cell is defined as the slope that is obtained from the light generated I-V curve when the current through the device is zero *i.e.,* open circuit condition as shown in Eq. 1.3.

$$R_s = \frac{1}{\frac{\partial I}{\partial V}} \Big|_{V=VOC} \qquad \textbf{Eq. 1.3}$$

The series resistance occurs between the metal contact and the semiconducting layer, the resistance arises between the front and rear contact of solar cell.

1.3.7 Shunt Resistance (R_{SH})

The shunt resistance of the device is determined from the slope of the light generated I-V curve when the voltage through the device is zero *i.e.,* short circuit condition as shown in Eq. 1.4.

$$R_{sH} = \frac{1}{\frac{\partial I}{\partial V}} |_{V=0} \qquad \textbf{Eq. 1.4}$$

Moreover, due to the presence of defects associated during fabrication is the prime cause for the shunt resistance. Due to the presence of these parasitic resistances the rectangle of J-V curve deviates resulting in the variation of fill factor and efficiency of the solar cell.

1.3.8 Equivalent Circuit of Solar Cell

To get the thorough understanding of the working principle of solar cell the study of the equivalent circuit model is crucial. In a practical solar cell, a light generated current source is connected in parallel with the diode.

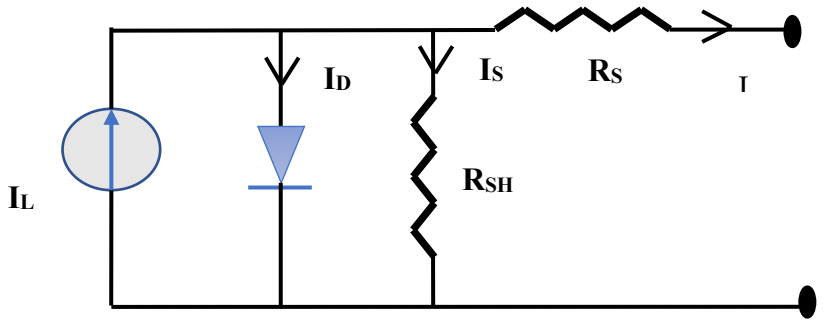

Fig. 1.7. Equivalent circuit of the solar cell

From the equivalent circuit as shown in Fig. 1.7, the total current represented as I, which is obtained using Kirchhoff's current law (KCL) as depicted in Eq. 1.5, Eq. 1.6 and Eq. 1.7 [7].

$$I = I - I_D - I_{SH} \quad \text{Eq. 1.5}$$

$$\text{Also, the } I_D = I_0 \exp\left(\frac{qV_D}{\eta' KT}\right) - 1 \text{ and } I_{SH} = \frac{V_{SH}}{R_{SH}} \quad \text{Eq. 1.6}$$

Where I_D is defined as diode current, R_{SH} is shunt resistance
I_{SH} is the shunt current

Hence, the overall resultant current is

$$I = I_L - I_0\left(\frac{\exp(q(V + IR_s))}{\eta' KT} - 1\right) - \left(\left(\frac{V + IR_S}{R_{SH}}\right)\right) \quad \text{Eq. 1.7}$$

Where I_L is the light generated current and η' is diode ideality factor

1.4 Different Generation of Solar Cells

The photovoltaic technology can be classified into three generations depending on their absorber or active materials namely first generation (Si-based solar cell), second generation (Semiconductor compound) and third generation (Emerging or novel materials) as shown in Fig. 1.8 [8].

The different generations are beneficial for different applications. The first generation solar cell provides highly efficient and expensive solar cells. The second generations solar cell consists of the less efficient solar cells but is also inexpensive as compared to the first generation solar cell. To overcome this low efficiency and high-cost trade-off, the third generation or novel material technologies provides relatively high efficiency and low-cost fabrication methods.

1.4.1 First Generation Solar Cell

It is one of the mature photovoltaic technologies consists of monocrystalline silicon and polycrystalline silicon solar cells. The exploitation of silicon in the first generation solar cells is due to its non-toxic and stable nature. In addition, it is considered the second most abundant material in the earth crust, due to which the raw materials are convenient in nature. Moreover, the silicon-based technology is compatible with other devices of the microelectronics industry makes silicon a suitable candidate for the photovoltaics industry[9]. The first generation solar cell can be further classified as crystalline silicon and amorphous silicon-based solar cells [8].

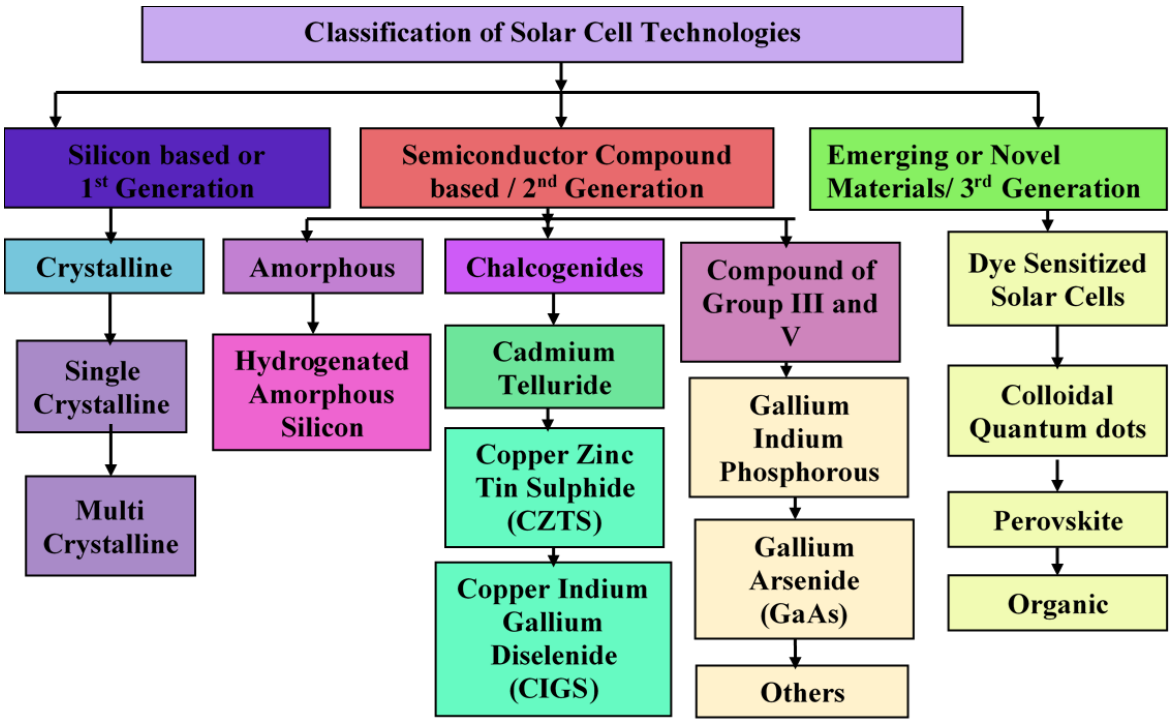

Fig. 1.8. Different Generation of solar cells [8]

1.4.2 Second Generation Solar Cell

The semiconductor-compound[10] based technology consists of chalcogenides materials and compounds of III-V based group material is known as second generation solar cell. Mainly, the solar cells made by thin-film process comes under the category of second

generation solar cells. The major focus on this technology consists of amorphous silicon (a-Si), copper indium gallium selenide (CIGS), copper zinc tin sulfide (CZTS), gallium indium phosphide (GaInP)[11], hydrogenated amorphous silicon [12], gallium arsenide (GaAs) and cadmium telluride (CdTe)[13]. The primary aim of the second generation solar cells is to reduce the cost of the solar cell compared to the first generation solar cell. The second generation solar cell offers some advantages over first generation solar cells [8].

1.4.3 Third Generation Solar Cell

With the progressive achievement of materials and growth of device engineering, the researcher's attention diverted towards the production of low-cost high-efficiency solar cell technology leading to the development of 3rd generation solar cells. The 3rd generation solar cell technology is drifted towards commercialization as they utilize nanostructured based materials which depict the high device efficiency. In addition, the third generations solar cells are easily processed via solution processing technique at a large scale and are reaches towards the high-efficiency limit within a limited period of time. As given in Fig. 1.8, it includes the dye-sensitized solar cell, organic solar cells[14], colloidal quantum dots solar cells[15] and perovskite solar cells, *etc* [8].

Fig. 1.9 shows the classification of different generations of solar cells based on their cost and efficiency. It can be stated from Fig. 1.9 that the first generation solar cell corresponds to high cost and high-efficiency solar cell. The second generation solar cell shows low cost but low-efficiency solar cell. The third generation solar cell depicts low-cost high-efficiency solar cell makes the third generation solar cell the most prominent technology for future photovoltaics[16].

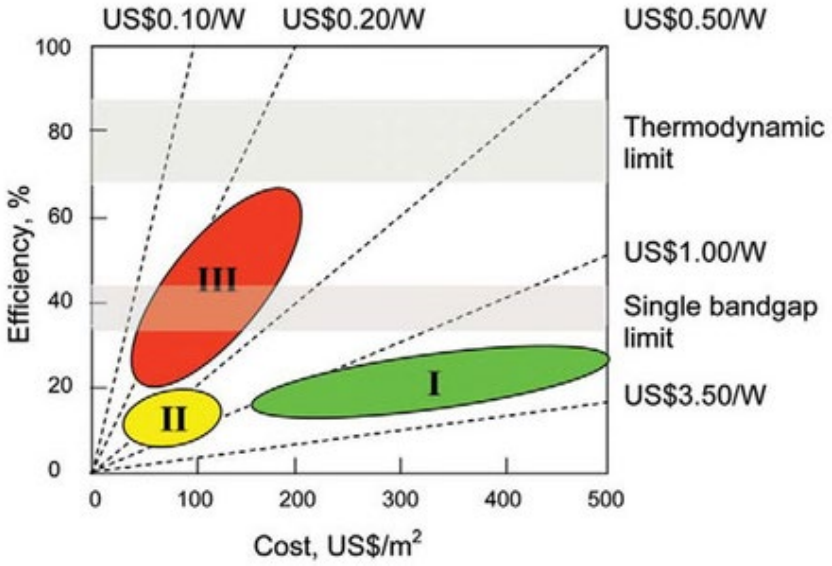

Fig. 1.9. Classification of the generation of solar cells based on their efficiency and cost[16]

1.5 Introduction to Perovskite Solar Cells (PSC)

The PSC has attracted considerable attention of researchers due to its extraordinary properties including large charge carrier's diffusion length, high absorption coefficient, ability to alter its bandgap, inexpensive, high dielectric constant to facilitate proper charge transportation, high mobility, long charge carrier lifetime, *etc* and being compatible with solution-processed deposition technique [17][18][19][20][21][22][23][24][25][26][27]. These astonishing properties led to the enhancement of perovskite photovoltaic performance from 3.8 %[17]in 2009 to 25.5% [27][28][29]. Perovskite material is a mineral like $CaTiO_3$, which was initially discovered in 1839 by Gustav Rose in Ural Mountain[30]. The mineral is named after Russian mineralogist Lev Alekseyevich von Perovski (L.A. Perovski). The crystal structure of perovskite is ABX_3 where A represents generally monovalent organic cation (MA^+, FA^+, Cs^+ *etc*), B represents a divalent cation (Pb^{2+}, Sn^{2+}) and X shows a halide anion (I^-, Br^-, Cl^-). The perovskite solar cell offers several advantages over the other solar cell technologies such as it shows less carrier recombination, allows the substitution of cation and anion for bandgap tuning as well as flexible in nature[31]. These outstanding properties make perovskite solar cells as a strong competitor among emerging photovoltaic technologies. Additionally, the

perovskite solar cell shows few challenges that need to be addressed. The control of the layer morphology, material parameters, the toxicity of lead material, high degradation against moisture and stability of perovskite solar cells are various issues that need to be resolved for the successful commercialization of flexible perovskite solar cell technology.

1.5.1 Structural Properties of Perovskite Solar Cell

The structural properties of any material are analyzed by the octahedral and tolerance factor. In the perovskite structure consists of ABX_3, the tolerance factor and octahedral factor should lie in the range of $0.813<t<1.107$ and $0.442<\mu<0.895$[32]. The tolerance factor (t) and octahedral factors (μ) as mentioned in Eq. 1.8

$$t = \frac{r_A + r_x}{\sqrt{2}(r_B + r_X)} \text{ and } \mu = \frac{r_B}{r_X} \qquad \textbf{Eq. 1.8}$$

where,

r_A, r_B, r_X, is defined as the radius of A, B and X element

1.5.2 Schematic and Working of Perovskite Solar Cells

Depending upon the light that enter into the cell the perovskite solar cell is classified as n-i-p or p-i-n based solar cell. Fig. 1.10a shows the schematic of a n-i-p based solar cell. The structure of perovskite solar cells consists of a transparent electrode that allows light to enter into the absorber materials.

The electron and hole transport layers are used to facilitate the proper transportation of electrons and holes respectively. The perovskite layer is the main absorber layer that allows the photons to get absorbed and thus generates the electron and hole pair. The main function of the electron transport layer is to allow the transport of electrons and block the holes also termed as hole blocking layer. Similarly, the hole transport layer allows the transfer of holes to collect as the back electrodes and block the electrons also termed as hole blocking layer.

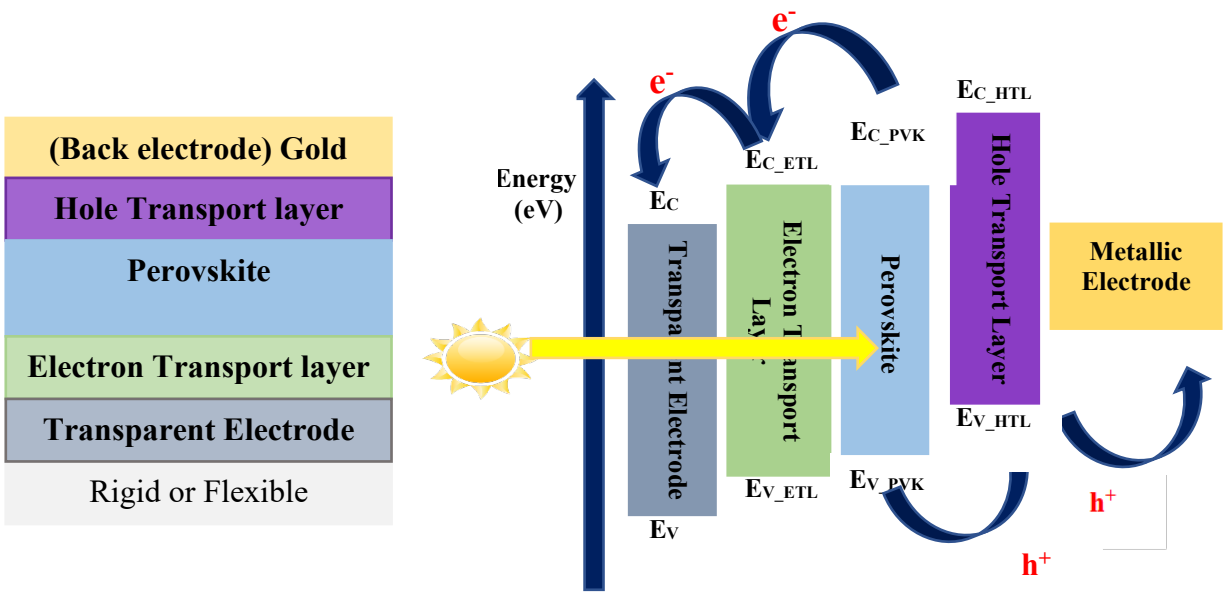

Fig. 1.10. (a) Schematic of perovskite solar cell **(b)**Working of perovskite solar cell

Fig. 1.10b, shows the working principle of the perovskite solar cell. When the light falls onto the perovskite layer the absorption of photons takes place within the perovskite layer with the condition of ($h\nu \geq E_g$) *i.e.*, those photons are absorbed having energy greater than the bandgap of the material. The absorption of photons generates the electron and hole pairs and subsequently excites them onto their LUMO (lowest unoccupied molecular level) and HOMO (highest occupied molecular level). In the presence of the built-in electric field between the ETL, and HTL, the electrons and holes are get separated accordingly. Later, the electrons and holes are collected by their respective back and front electrodes.

1.6 Motivation Towards the Perovskite Solar Cell Technologies

In 2009, the foremost PSC shows the PCE of 3.8% developed using a solution-processed technique as shown in Fig. 1.11[17]. Afterwards, several modifications had been introduced to enhance the perovskite solar cell device PCE. These modifications include the perovskite-quantum dots solar cell using TiO_2 surface modification, the low-cost solution-processed methodology, compositional engineering, *etc*. However, the certified PCE of perovskite solar cells reaches up to 25.5% [28] as shown in Fig. 1.11. Despite the

progressive advancement of these layers, the toxicity of the Pb and its composites in the perovskite, remains a huge obstacle that will impede its potential towards the commercialization of an efficient perovskite solar cell. To mitigate these challenges there is an urge to explore the lead-free alternatives in the perovskite solar cell.

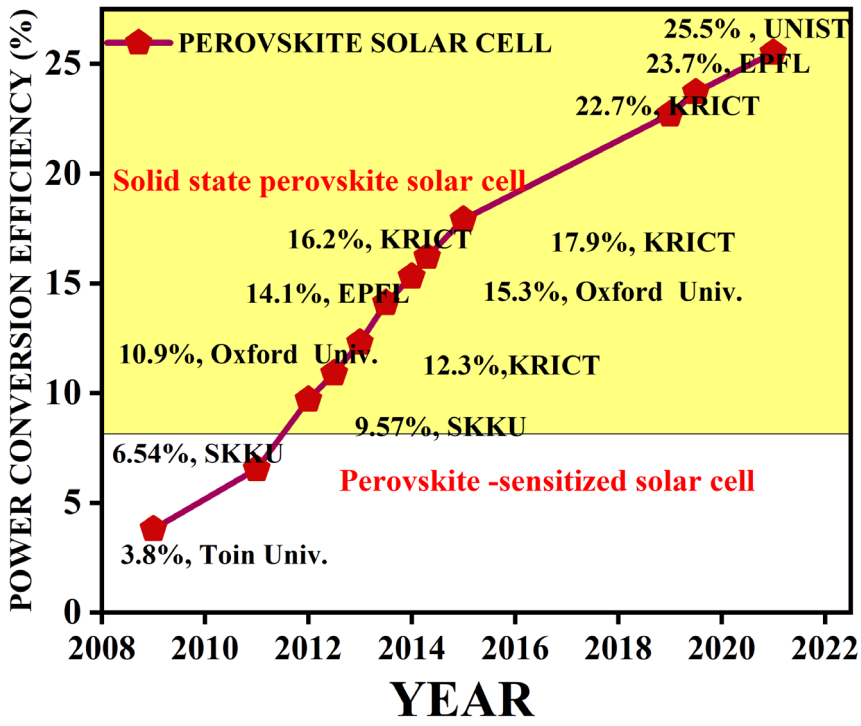

Fig. 1.11. Technological development of the perovskite solar cell

It has been observed from the literature that there are numerous perovskite layers are available and many of them have been already explored in terms of device performance. However, the efficiency is still limited as the proper selection of electron transport layer (ETL) and hole transport layer (HTL) for a particular perovskite layer also shows a crucial role to decide the PV performance. It is extremely difficult to optimize all possible combinations of perovskite and charge transport layers through the fabrication route. Hence, there is a stringent requirement to explore the simulation of PSC based on different perovskite layers and their combination with charge transport layers. However, the solar cell performance is also limited due to the unavailability of the perovskite layer which has the wide absorption of solar cell spectrum owing to the bandgap limitation. Hence, to enhance the PCE of solar cell, researchers are working more towards the exploration of the multijunction solar cell[33][34][35][36][37][38][39]. As in the

standalone wide and narrow bandgap perovskite solar cells, less photovoltaic performance is achieved. This is mainly due to the unavailability of the absorption of the wider spectrum. Therefore, by using multijunction/tandem perovskite solar cell the device efficiency can be further improved because it allows the absorption of the wider range of solar spectrum.

To achieve this, the main challenge is to optimize the narrow and wide band gap lead-free perovskite layers along with their proper band alignment with the charge transport layers in such a way that the multijunction perovskite solar cell should exhibit superior device performance. Moreover, there is extremely limited literature available for the understanding of the effect of various parameters on the PV performance of lead-free APMJSC [40]. In the proposed thesis work, different perovskite layers have been taken for simulation which has shown the successful fabrication of the perovskite solar cell but not widely explored to their best in the literature. Further, the optimization of perovskite solar cells using these layers are performed in terms of different ETL and HTLs. Moreover, the numerical simulation of Pb-free APMJSC is performed. Further investigation includes, the study of various effects (such as the effect of defect density, the impact of thickness *etc.*) is also explored.

CHAPTER 2

LITERATURE REVIEW

This chapter includes the literature review of the perovskite solar cell. A comprehensive study based on the Pb-free PSC alternatives is discussed. The subsection of the chapter includes the literature based on the methylammonium tin halide ($CH_3NH_3SnI_3$), methyl ammonium germanium halide ($CH_3NH_3GeI_3$), cesium tin-germanium triiodide ($CsSnGeI_3$) based PSC and ($FAMASnGeI_3$) based PSC. In addition, the literature based on the double-perovskite *i.e.,* mixed antimony bismuth halide ($Cs_2AgBi_{0.75}Sb_{0.25}Br_6$) based perovskite solar cell (PSC) is discussed. Furthermore, the literature based on the all-perovskite tandem/multijunction solar cell is also presented. After a comprehensive literature review, the identified research gaps and the objectives have been defined.

2.1 Lead-Free Perovskite Solar Cell Alternatives

A comprehensive review of different Pb-free PSC alternatives is included in this subsection.

2.1.1 Methyl Ammonium Tin Halide ($CH_3NH_3SnI_3$) Perovskite Solar Cells

Foremost Neol. *et al.* proposed the $CH_3NH_3SnI_3$ based Pb-free perovskite solar cell with device efficiency up to 6% under complete sunlight environment with the solar cell structure of FTO/c-TiO_2/mp-TiO_2/ $CH_3NH_3SnI_3$/ spiroOMeTAD/Au[41]. However, it is deduced from the THz mobility and its lifetime of charge carriers that by optimizing the material in terms of doping density, the $CH_3NH_3SnI_3$ is considered a suitable as an alternative to nontoxic perovskite solar cells. However, $CH_3NH_3SnI_3$ film shows an unstable nature due to the rapid formation of Sn^{2+} to Sn^{4+}, and hence the experiment is carried out under a nitrogen (N_2) glove box. Hence, it can be concluded from the work that the device efficiency is limited due to the self oxidation and hence it is significant to focus on the new method to reduce the Sn oxidation and development of a stable lead-free perovskite material[41].

Ma.Lin. *et al.* studied the photophysics of Pb-free $CH_3NH_3SnI_3$ based perovskite layer using broad transient absorption spectroscopy and time-resolved fluorescence spectroscopy. The hot carrier relaxation is also explored by using transient absorption (TA) measurement[42]. It is obtained from broadband transient absorption spectroscopy that the absorption coefficient of $CH_3NH_3SnI_3$ is 2×10^4 cm^{-1}. Also, it is observed that $CH_3NH_3SnI_3$ exhibits low binding energy. The fluorescence quenching measurement is performed to find out the electron and hole diffusion length. The ETL and HTL in this structure is considered as TCNQ and SpiroOMeTAD and the diffusion coefficient for the electron and holes are found to be 1.28±0.73 cm^2/s and 0.59±0.27 cm^2/s. The electron and hole mobility is estimated as 2000 cm^2/Vs and 300 cm^2/Vs. Hence, it is depicted from the work that the diffusion length of $CH_3NH_3SnI_3$ based perovskite layer depends on the purification process and the quality of the material. Further to improve the photovoltaic performance the addition of 20% of SnF_2 into the precursor material. The presence of SnF_2 leads to reduce the defect concentration of the material which in turn enhance the device performance. Still, less device efficiency is observed due to the low absorption of photons, low absorption coefficient and a high carrier recombination rate is also obtained. However, the work does not provide any information regarding the perovskite film morphology and the optimum thickness needed for the perovskite absorber layer [42]**.**

Lefanova *et al.* synthesize low-temperature solution processing $CH_3NH_3SnI_3$ based perovskite layer. The optical, electrical and structural properties are examined on the dimethyl formamide (DMF) and dimethylsulfoxide (DMSO) with gamma butyrolactone[43]. It is obtained that $CH_3NH_3SnI_3$ shows metallic behaviour as well as exhibits the bandgap of 1.3eV. The optical properties of DMF and DMSO based PSC is studied and it depicts the broad absorption edge of 950 nm which exhibits the optical bandgap of 1.3 eV. The $CH_3NH_3SnI_3$ shows higher absorption characteristics in the case of DMF rather than DMSO. To obtain the photocurrent, current sensing atomic force microscopy (CS-AFM) is performed and the obtained short circuit photocurrent in the case of DMF based $CH_3NH_3SnI_3$ is -23.9 pA and for DMSO it is around 1pA. The calculated mobility for DMF and DMSO based $CH_3NH_3SnI_3$ achieved is 0.59 cm^2/Vs and 0.09 cm^2/Vs respectively. Moreover, it is obtained from the literature that at the dark condition no detectable photocurrent is obtained. This is attributed to the insufficient built-in electric field in the device resulted in the limited charge collection. In addition, in

the light condition, the obtained photocurrent shows an S-shape curve which is attributed to the poor charge carrier collection[43].

Mandadapu *et al.* simulated the Pb-free $CH_3NH_3SnI_3$ based PSC with TiO_2 and CuI as an ETL and HTL[44]. In addition, the effect of absorber layer thickness is studied. The impact of the absorber defect density is realized by varying the defect density from 10^{13} cm^{-3} to 10^{18} cm^{-3}. The optimized perovskite thickness and the defect density is found to be 0.6 μm and 10^{14} cm^{-3}, respectively. Moreover, the impact of the perovskite bandgap and the temperature is also investigated. The optimized absorber layer bandgap is found to be 1.3 eV with the optimized device temperature is obtained as 300 K. However, no study has been performed on the impact of the different charge transport layers. Nevertheless, this work prompts an opportunity that one can also explore the other lead-free alternatives of perovskite solar cells using the simulation method[44].

Anwar *et al.* proposed a $CH_3NH_3SnI_3$ based numerical model with the variation of several HTMs. This study includes the investigation of the variation of thickness of absorber layer, the impact of interface defect states at both interfaces *i.e.,* HTM/absorber and absorber/ETM, the effect of density of states and the effect of different back electrode contact[45]. The thickness of the absorber layer is varied between 300 nm to 1000 nm and the optimized thickness is obtained as 650 nm. It also includes the effect of interface defect density for (ETL/perovskite and perovskite /HTL interface) by altering the interface defect density from $10^{10}cm^{-3}$ to $10^{16}cm^{-3}$ and the optimized interface defect density is found to be $10^{12}cm^{-3}$. In addition, the effect of several back electrode metal work functions is studied by varying the back contact from Ag, Fe, Cu, Au, Ni, Pt and graphite sheet out of which the Au with 5.1 eV metal work function is obtained as the optimized back contact. Moreover, the effect of the various hole transport layer is also studied and the optimized hole transport layer is obtained as Cu_2O with the device efficiency enhances up to 20.23%. Despite the significant study, limited HTLs are realized. In addition, the impact of the various electron transport layer on the PV performance is also not reported by the authors[45].

Baig *et al.* numerically modelled the solar cell by considering $Cd_{1-x}Zn_xS$ and $MASnBr_3$ as ETL and HTL respectively. Further study includes the effect of HTL, perovskite thickness, and absorber layer doping concentration[46]. The HTLs are optimized by

using the band offset technique and has reported that $MASnBr_3$ as an HTL exhibits the spike, due to which the E_a (activation energy) is equivalent to the bandgap energy of the solar cell and thus enhances the V_{OC}. Later, the absorber layer thickness is altered from 0.1 μm to 1 μm and the optimized thickness of the absorber is found to be 0.5μm. Moreover, the effect of ETL and the electron affinity is also realized. It is deduced from the work that conduction band offset (CBO) shows a major influence on the PV performance of the solar cell. Due to the E_g tunability, the bandgap of CdS is altered by adding Zn on it and the CBO effect is studied. It is obtained that CBO directly relates the PCE of the solar cell as the positive CBO resulted in the increase in the PCE. However, the negative CBO reduces the PCE of the solar cell due to the formation of the spike in between the ETL and absorber layer interface, which impedes the carrier collection, thereby reduces the overall photovoltaic performance of the solar cell. The resulted optimized PV performance enhances up to 18.71%. In this article, the optimized ETL is a cadmium-based layer that is toxic in nature. Hence the reported paper opens a window to find some other non-toxic ETL to realize non-toxic perovskite solar cells [46].

Kumari *et al.* proposed an experiment and simulation of $CH_3NH_3SnI_3$ based perovskite solar cell with ZnTe as an HTL[47]. The ZnTe is an inorganic hole transport layer that belongs to the II-VI group of the periodic table. The bandgap of the ZnTe layer is 2.26 eV, with high hole mobility *i.e.,* 80-100 cm^2/Vs. The density of states value for ZnTe is considered as $1.17\times10^{18}/cm^3$. It is found from the simulation that the solar cell with ZnTe as an HTL, and TiO_2 as an ETL shows the device efficiency of 22.96%. Later, in simulation, the absorber layer thickness is found to be 0.400 μm, doping density of HTL is optimized which is found to be $10^{19}/cm^3$, resulted in the PCE to elevates up to 22.96%. The ZnTe is deposited in a form of nanoflower as HTL which leads to the increase of the surface area available for the absorption which in turn improve the device performance. However, the same fabricated configuration depicts the 8.41 % PCE. Nonetheless finding an alternative of HTL, no comparative analysis of the existing HTLs is performed. Moreover, the effect of the other ETL alternatives is also not realized. In addition, no significant study of the absorber layer thickness and its defects configuration is also not realized in this work[47].

2.1.2 Methyl Ammonium Germanium Halide ($CH_3NH_3GeI_3$) Based PSC

In the perspective of the Pb-free alternatives, the Sn based PSC are widely explored. However, the rapid oxidation of the Sn^{2+} to Sn^{4+} causes structural instability in the tin-based perovskite solar cells[48][49][41][42]. Hence, there is a requirement for the exploration of any other viable alternative in place of Sn cation. Moreover, germanium-based PSC proves to be a significant replacement of the tin alternative in the perspective of Pb-free perovskite solar cell[50][51][52].

This is mainly due to the reason, as the germanium (Ge) shares the same group to that of Pb and Sn in the periodic table and hence it depicts the analogous optoelectronic properties to that of Pb and Sn along with high conductivity. However, limited literature is available for the extensive exploration of methyl ammonium germanium perovskite, hence there is a need to explore the methyl ammonium germanium perovskite to further enhance the PV performance of the solar cell. In addition, the methyl ammonium germanium halide perovskite solar cell depicts the wide bandgap[50] and hence it can be considered as a promising alternative for the perspective of wide-bandgap perovskite layer in the application of lead-free APTSC.

Foremost, Stompus *et al.* proposed the synthesis of Pb-free germanium halide perovskite. The variety of germanium halide based structures with diverse bandgap is studied using the solution processing method. The device structural configuration, non-linear optical properties, second harmonic generation properties for the series of structures are explored in this paper. The optical absorption properties of various structures are explored and it is reported that due to the molecular vibration of organic cations some of the structures are suitable for nonlinear optical properties[50].

Krishnamoorthy *et al.* performed computational screening based DFT first principle calculation to reveal that Ge can be considered as a potential candidate as a B site for Pb-free ABX_3 based perovskite structure. Nine different structures are studied, and it has been found that three candidates namely $RbSbBr_3$, $CsSnBr_3$, $CsGeI_3$ are predicted to be stable. However, experimentally $MAGeI_3$, $FAGeI_3$ $CsGeI_3$, based structure are explored[51]. Among the three synthesized structures, the $CsGeI_3$ is stable whereas

$MAGeI_3$ is easily decomposed in a single step and $FAGeI_3$ exhibits unstable nature. The estimated value of the bandgap is obtained as 1.63 eV, 2.0 eV and 2.35 eV for $CsGeI_3$ $MAGeI_3$, and $FAGeI_3$ based solar cell. These bandgap value proves to be suitable for the application of Pb-free tandem solar cell. The CBM and VBM values are also obtained for these compounds using photoemission spectroscopy. Further, the fabrication of the $CsGeI_3$, $MAGeI_3$, and $FAGeI_3$ based solar cell is performed and the PV performance is measured with TiO_2 and spiroOMeTAD is considered as ETL and HTL respectively. The resulted PV performance suggested that due to the poor film quality of $FAGeI_3$ based solar cells no photocurrent is attained. However, photocurrent of 5.7 mA/cm^2 and 4 mA/cm^2 is obtained for $CsGeI_3$ and $MAGeI_3$ based solar cells, respectively. Therefore, it is deduced from the computational screening that Ge based perovskite solar cell can be considered as a future candidate for Pb-free PSC[51].

Sun *et al.* studied the optoelectronic, structural properties of Pb-free Ge-based perovskite solar cells using DFT calculations. Various lead-free alternatives are explored such as $MASnI_3$, $MAGeI_3$. $MAGeBr_3$, $MAGeCl_3$. The ideal range of tolerance factors for perovskites lies in the range of 0.81-1.11. However, the tolerance factor of $MAGeI_3$, $MAGeBr_3$, $MAGeCl_3$ are obtained as 0.965, 0.988, 1.005 which closely matches with the ideal perovskite tolerance factor ($0.813<t<1.107$) [52]. In terms of bond length and bond angle, $MAGeI_3$ shows similar characteristics to that of $MAPbI_3$ and $MASnI_3$ based solar cells. The order of formation energy for different perovskite is found to be $MAPbI_3$> $MAGeI_3$>$MASnI_3$>$MAGeCl_3$>$MAGeBr_3$. Mainly, a minute difference is obtained in the stability of $MAPbI_3$ and $MAGeI_3$ and thus, $MAGeI_3$ is considered as a suitable candidate for Pb-free PSC. However, $MAGeI_3$ based perovskite depicts better carrier transport properties than $MAPbI_3$ and $MASnI_3$ based solar cells. Further, the optical properties of several considered perovskites are explored. In the case of $MAGeI_3$, unlike $MAPbI_3$ it shows weak absorption in the UV spectrum range. However, good absorption in the visible range is obtained[52].

Kanoun *et al*. simulated the lead-free methyl ammonium germanium iodide ($CH_3NH_3GeI_3$) based PSC using SCAPS 1D[53]. The effect of diverse hole transport layers (HTLs) is realized on the effect of PV performance. Based on the charge carrier mobility and the band alignment the optimized HTL obtained is Cu_2O. The influence of the variation of perovskite thickness is varied for various HTLs. It is thus obtained from

the simulation, that the device shows better PV performance if the thickness is kept in the range of 600 nm to 700 nm. Later, the influence of defect density on the PV performance is also investigated. It is obtained that as the defect density enhances the device performance decreases due to the creation of recombination centres at the absorber layer. The defect density is varied between 1×10^{14} cm^{-3} to 1×10^{18} cm^{-3} and the optimized value attained is 1×10^{14} cm^{-3}. However, as the defect density of the absorber layer increases the overall device performance degrades [53]. It is recommended, that the noble metal electrodes show the best device performance as compared to others. Moreover, the effect of the operating temperature of solar cells is studied, and the optimized temperature is found to be 300K [53].

Lakhdar *et al.* numerically simulated the $MAGeI_3$ based perovskite solar cell using SCAPS 1D. The effect of different kind of ETLs, the thickness of ETLs, the thickness of the perovskite layer is investigated[54]. The device simulation structure considered is ITO/PEDOT:PSS/$MAGeI_3$/ETL/Ag with the charge transport layer (CTL) thickness and absorber layer thickness considered as 30 nm and 400 nm respectively. The initial simulated device structure depicts the 11.6% PCE. The optimized ETL was found to be C60 and the optimized thickness of CTL and perovskite absorber layer is found to be 50 nm and 650 nm. Upon optimization, the PCE enhances up to 13.5% [54].

Hima *et al.* reported a numerical simulation of lead-free methyl germanium halide based PSC. The simulation mainly focuses to improve the device efficiency by exploring the diverse HTLs[55]. The simulated device configuration considered is a p-i-n based PSC in which C60 and PEDOT: PSS is considered as an initial HTL and ETL. Several HTL incorporated such as PEDOT: PSS, CuSCN, $CuSbS_2$, NiO out of which $CuSbS_2$ exhibits the highest device efficiency of 23.58 % and the reported V_{OC}, J_{SC} and FF is found to be 1.66 V, 23.59 mA/cm^2, 60.29%[55].

2.1.3 Cesium Tin Germanium Triiodide ($CsSnGeI_3$) Based PSC

In the context of the Pb-free alternative, the demand for stable perovskite solar cells grabs wide attention among researchers [56][57][58]. Despite showing the progressive achievement of tin halide and the germanium perovskite solar cell the need for the air-stable perovskite alternative is raising rapidly [59][60][61]. To attain this instability,

initially, $CsSnI_3$ is considered as a promising alternative still the photovoltaic performance is inadequate along with the instability[62][63][64]. Hence, it is found that mixing Ge with the Sn to form $CsSnGeI_3$ as a perovskite layer depicts a promising strategy as it exhibits ultrahigh stability along with better air tolerance[65]. Still, the $CsSnGeI_3$ based perovskite layer is not widely explored. Also, it shows a promising narrow bandgap and solution processing compatibility due to which it proves to be a considerable candidate for the application of narrow bandgap layer in tandem perovskite solar cell application[66].

Chen.M. *et al.* mainly focuses on the removal of perovskite toxicity and stability issues. For this perspective, they demonstrate the lead-free all-inorganic perovskite absorber layer that depicts high stability and fabricate via the solution-processed method. Surprisingly, it was obtained that by addition of Ge on $CsSnI_3$ *i.e.,* $CsSnGeI_3$ based perovskite layer resulted a highly stable, air tolerant, perovskite solar cell. Because of the high oxidation of Ge, a stable native oxide layer of ultrathin <5nm is formed. The $CsSnGeI_3$ based PSC shows better optical absorption, bandgap of 1.50 eV. As the perovskite is exposed to air a stable oxide layer is formed shows it higher air stability. In addition, the device degradation is less even after 500 h as the PCE reduces from 6.79 % to 6.23%. Moreover, the presence of Sn also increases its moisture stability. The PSC with $CsSnGeI_3$ as an absorber layer depicts 7.11% PCE. Therefore, $CsSnGeI_3$ is considered a promising candidate for the progress of Pb-free PSC [65].

Raghvendra *et al.* proposed a drift-diffusion model for Pb-free $CsSnGeI_3$ based PSC using Sentarus TCAD. The device structure considered for the simulation consists of $CsSnGeI_3$ as a perovskite absorber layer, SpiroOMeTAD, PCBM as an HTL and ETL layer respectively[66].

The device performance after the simulation is obtained as V_{OC} = 0.61 V, J_{SC}=18.45 mA/cm^2, FF= 69.50, η= 7.81% which meticulously resembles the experimental result reported by Chen.M. *et.al.*,. Further, the influence of defect density, interface defect density, the influence of absorber layer thickness and the impact of ETL and HTLs are carefully examined[66]. The influence of perovskite thickness and the doping density is also studied. The perovskite thickness altered from 100 nm to 600 nm and the optimum thickness of $CsSnGeI_3$ is obtained as 300 nm.

The influence of absorber doping concentration is also examined by varying the doping concentration of the absorber layer from 1×10^{14} cm^{-3} to 1×10^{17} cm^{-3}. The optimized N_A obtained is found to be 4×10^{16} cm^{-3} resulted the enhancement of PCE to 9.01%.
Moreover, the defect density of $CsSnGeI_3$ based perovskite layer is altered from 1×10^{14} cm^{-3} to 1×10^{18} cm^{-3} . It is obtained from the simulation study that as the defect density reduces the photovoltaic performance enhances up to 10.18%. Later, the effect of several HTL is also observed. Among various HTL, Cu_2O shows the best device performance reaches the PCE up to 13.29% which is a promising efficiency for Pb-free PSC[66].

Islam *et al.* simulated a c-Si/perovskite tandem based structure and compare the device performance with the lead and lead-free based PSC. The $CsSnGeI_3$ is considered as a perovskite absorber layer for the top subcell configuration. The current matching condition for the 2T (two-terminal) tandem solar cell is obtained by changing the thickness of the absorber layers. The optimum thickness for the $CsSnGeI_3$ and $MAPbI_3$ based PSC was found to be 1.3 µm and 1.8 µm that depicts the PCE of 15.84% to 24.21%[67].

The influence of defect density and interface defect density is also studied. The optimized defect density is found to be 10^{14} cm^{-3}. The optimum interface defect density for HTL/perovskite interface is 10^{14} cm^{-3} and for perovskite/ETL interface is 10^{15} cm^{-3}. However, with optimized parameters, the overall PCE of tandem based solar cells is found to be 28.53%. In comparison, it is found that $CsSnGeI_3$ proves to be a suitable perovskite layer for lead-free tandem solar cell application. As the device performance is found to be comparable to $MAPbI_3$ based solar cells [68].

2.1.4 $FA_{0.75}MA_{0.25}Sn_{0.25}Ge_{0.5}I_3$ (FAMASnGeI$_3$) Based Perovskite Solar Cells

To further enhance the device efficiency of Pb-free PSC the mixed Sn-Ge based perovskite layers shows a significant role. It is obtained from the literature that the mixed Sn-Ge based perovskite layers exhibit the high air stability attributed to the doping of the Ge cation [69][70]. Moreover, the mixed Sn-Ge based perovskite layers show high charge carrier mobility. However, the mixed $FAMASnGeI_3$ based perovskite layer exhibits better device numerical parameters, hence it has the potential to further elevate the photovoltaic

performance by using some band offset, and charge transport layer engineering, Despite having significant properties of $FAMASnGeI_3$ based perovskite layer, extremely limited literature is available [69][70]. Also, due to its low bandgap, it exhibits a promising candidate for the application of a narrow bandgap layer in APMJSC applications.

Ito. *et al.* fabricated a lead-free mixed Sn-Ge based perovskite material. The $FAMASnGeI_3$ based material shows a promising bandgap of 1.4 eV to 1.5 eV which is an ideal range of bandgap for the solar cell application [69]. In addition, XRD analysis, optical properties, surface morphology studies are done. It is obtained from the PYS measurement that the upshift of the valence band is obtained by adding the Ge into the $FAMASnI_3$ based perovskite. It had been found from the surface roughness technique that the roughness is initially decreasing with the increasing Ge concentration. Later, an increase in the surface roughness trend is obtained with respect to the varying concentration. Further, the PV performance of the $FAMASnI_3$ and $FAMASnGeI_3$ based PSC is measured and it has been obtained that $FAMASnGeI_3$ depicts better performance than $FAMASnI_3$ based perovskite solar cell. The high J_{SC} of $FAMASnGeI_3$ is mainly due to better photon absorption [69].

Minemoto *et al.* numerically investigated the Pb-free mixed Ge-Sn based perovskite solar cell with PCBM and PEDOT: PSS is considered as an ETL and HTL respectively. Initially they theoretically analyse the built-in potential to attain high V_{OC}. Later, the effect of conduction band offset and impact of the difference between CB of perovskite and back contact work function (E_{C_PVK}-Φ_{BC}) is analysed. Primarily, four different combinations are realized by altering the E_{V_HTL} and Φ_{BC} of the perovskite solar cell. Initially, the relation between the built-in potential and V_{OC} is examined [70].
The further investigation includes the outcome of CBO of PVK/ETL and E_{C_PVK}- Φ_{BC} on the perovskite photovoltaic performance. This investigation consists of mainly two cases *viz* ($\chi_{ETL} > \Phi_{BC}$) and ($\chi_{ETL} \leq \Phi_{BC}$).

In the case of $\chi_{ETL} < \Phi_{BC}$ the V_{bi} variates from -0.50 eV to 0.10 eV. In this condition, the V_{bi} is primarily influenced by E_{C_ETL}-E_{V_HTL} which shows the minor changes in V_{OC}. However, on the contrary in the condition of $\chi_{ETL} > \Phi_{BC}$ V_{bi} elevates with E_{C_PVK}- Φ_{BC} and is mainly governed by Φ_{BC}-E_{V_HTL} [70].

2.1.5 Lead-Free Double Perovskite Solar Cell

Double perovskite solar cell proves to be a compatible candidate with the current state-of-art for the Pb-free PSC alternatives [71]. To improve the structural stability of ABX_3 based perovskite structure, the divalent cation is replaced with the monovalent cation and trivalent cation. In general, the double-perovskite solar cell exhibits $A_2M^{1+}M^{3+}X_6$ structure where A represents a small cation such as caesium (Cs), M^{1+} represents monovalent metal ions (such as Na^+, K^+) and M^{3+} represents a trivalent metal cation (such as Bi^{3+}, Sb^{3+}) and X represents anions (such as Br^-, I^-, CN^-). Moreover, the double perovskite solar cell depicts a better optical bandgap, large absorption coefficient, large lifetime of charge recombination and variable optoelectronic properties[68][71]. In particular, $Cs_2AgBiBr_6$ based double perovskite solar cells (DPSC) are extensively explored and considered as a viable option for solar cell application[71]. Nevertheless, the PCE of the $Cs_2AgBiBr_6$ based PSC is limited *i.e.,*~ 5%[68][71]. This limited PV performance of $Cs_2AgBiBr_6$ is due to its wide bandgap of 2.2 eV which proves to be an inadequate bandgap for optoelectronic application [72]. Further, various strategy is introduced to reduce the bandgap by incorporating the (Tl^{3+}, Sb^{3+}) cations. It is acquired from the literature, that by replacing Bi with 25 % of Sb to make $Cs_2AgBi_{0.75}Sb_{0.25}Br_6$ based perovskite layer the bandgap is reduced to ~ 1.6 eV which is considered as a better alternative bandgap for solar cell application [73].

2.1.5.1 Mixed Antimony and Bismuth Based Double Perovskite Solar Cell ($Cs_2AgBi_{0.75}Sb_{0.25}Br_6$)

Pantaler *et al.* fabricate the lead-free mixed antimony bismuth (Sb-Bi) based double perovskite solar cell using the solution-processed technique. The effect of the PV performance on the different compositions of Sb is investigated. The structural composition, optical properties and electronic structure are determined. The presence of Sb on the $Cs_2AgBi_{0.75}Sb_{0.25}Br_6$ is confirmed by X-ray diffraction (XRD) analysis. With the help of the UV-vis measurement technique, the optical bandgap and the transmittance of the double-perovskite is determined. In addition, the chemical composition is obtained by XPS and EDX measurements. It is determined that the energy band shift is obtained upon the addition of the Sb cation. However, it is recommended that a further

investigation on the defect analysis of $Cs_2AgBi_{0.75}Sb_{0.25}Br_6$ based solar cells needs to be investigated [73].

Madan *et al.* simulate the two-terminal (2T) all-perovskite tandem solar cells by considering $Cs_2AgBi_{0.75}Sb_{0.25}Br_6$ as the top subcell having 1.8 eV bandgap and $FACsPb_{0.5}Sn_{0.5}I_3$ as the bottom subcell with a bandgap of 1.2 eV are considered. Primary, each standalone structure is simulated and the device photovoltaic performance is measured. Both the standalone structure are optimized based on their thickness and the optimized thickness of 380 nm and 400 nm is obtained for the top and bottom subcell [40].

Hossain. A. *et al.* realize the lead-free tandem solar cell with $Cs_2AgBi_{0.75}Sb_{0.25}Br_6$ as top subcell having 1.8 eV bandgap and $CH_3NH_3SnI_3$ as bottom subcell of 1.3 eV. They presented a complete non-lead-based perovskite solar cell with a tandem configuration.
The wide and narrow bandgap perovskite solar cell shows 15.55 mA/cm^2 and 30.13 mA/cm^2. However, the obtained V_{OC} is attained 1.13 V and 0.84 V for wide and narrow bandgap perovskite solar cells. It is obtained from the analysis, that the optimized thickness of the wide band gap layer is 400 nm and the narrow band gap layer is 426 nm is achieved. The wide band gap perovskite layer shows the PCE of 10.32% and the narrow bandgap perovskite layer shows the PCE of 14.54%. In addition, the tandem configuration shows the device PV performance depicts 24.86% power conversion efficiency [74].

2.1.6 Current State of Art for the Perovskite, Electron and Hole Transport Layers in Perovskite Solar Cell Technology

It is obtained from Table 2.1 and Table 2.2 that the PV performance of the solar cell mainly depends on the hole and electron transport layer. Hence, to realize an efficient solar cell the charge transport layer should be carefully chosen. Moreover, it has resulted from Table 2.1 and Table 2.2 that there is an extensive study performed using the various ETL and HTL is mainly on the lead-based perovskite solar cell. However, the toxicity of the lead material is the major roadblock towards the commercialization of these solar cells. To remove the toxicity issue, there is a stringent requirement to explore the effect of various charge transport layers on the PV performance of Pb-free PSC.

Table 2.1 Current state of the art for the various hole transport layer for perovskite solar cells

HTM Type	Device Structure	V_{OC}	J_{SC}	FF	η	References
SpiroOMeTAD	ITO/SnO_2/PVSK/PEAI /spiro-OMeTAD/Au	1.160	1.16	81.40	23.56	[75]
SpiroOMeTAD	ITO/SnO_2/PVSK/spiro-OMeTAD/Au	1.120	23.86	80.60	21.64	[76]
SpiroOMeTAD	FTO/c-TiO_2/CHI-$CsPbI_3$/spiro-OMeTAD/Ag	1.110	20.23	82.00	18.40	[77]
SpiroOMeTAD	ITO/SnO_2/$CsPbI_2Br$/Spiro-OMeTAD/MoO_3/Ag	1.120	15.40	81.50	14.05	[78]
SpiroOMeTAD	FTO/cp-TiO_2/mp-TiO_2/PVSK/spiro-OMeTAD/Au	1.162	23.78	78.80	22.00	[79]
SpiroOMeTAD	FTO/cp-TiO_2/mp-TiO_2/PVSK/spiro-OMeTAD/Au	1.120	23.98	79.62	21.38	[80]
PEDOT:PSS	ITO/PEDOT:PSS/PTAA/PVSK/PCBM/Ag	1.070	21.58	82.59	19.04	[81]
PEDOT:PSS	ITO/PEDOT:PSS/PVSK/PC61BM/Ag	1.040	22.22	80.00	18.46	[82]
PEDOT:PSS	ITO/PEDOT:PSS/PVSK/PCBM/Au	1.100	20.90	79.00	18.20	[83]
PEDOT:PSS	ITO/PEDOT:GO/PVSK/PCBM/ZnO/Ag	1.02	21.55	82.30	18.09	[84]
PEDOT:PSS	ITO/PEDOT:PSS/PVSK/PCBM/BCP/Ag	1.020	21.93	76.00	17.22	[85]
P3HT	FTO/cp-TiO_2/mp-TiO_2/PVSK/P3HT/Au	1.024	23.19	68.60	16.27	[86]
P3HT	FTO/cp-TiO_2/mp-TiO_2/PVSK/P3HT/Au	0.970	23.90	62.00	14.40	[87]

CuI	FTO/Cu@CuI/PVSK/PCBM/ZnO/Ag	1.060	23.31	76.10	18.80	[88]
CuI	FTO/CuI/PVSK/PCBM/Al	1.040	21.06	62.00	13.58	[89]
CuI	FTO/TiO_2/PVSK/CuI/Au	0.780	16.70	57.00	7.50	[90]
CuI	FTO/cp-TiO_2/mp-TiO_2/PVSK/CuI/Au	0.550	17.80	62.00	6.00	[91]
WS_2	ITO/WS_2/PVSK/C60/BCP/Al	0.970	21.22	73.00	15.00	[92]
CuSCN	FTO/cp-TiO_2/mp-TiO_2/PVSK/CuSCN/rGO/Au	1.112	23.24	78.20	20.40	[93]
CuSCN	FTO/cp-TiO_2/mp-TiO_2/PVSK/Pr-ITC ? Ph-DITC/ CuSCN/Au	1.071	23.49	76.21	19.17	[94]
CuSCN	FTO/cp-TiO_2/mp-TiO_2/PVSK/CuSCN/Au	1.040	23.10	75.30	18.00	[95]
CuSCN	ITO/SnO_2/PVSK/PDMS/CuSCN/Au	1.017	23.90	78.30	19.04	[96]
CuSCN	ITO/SnO_2/PVSK/PDMS/CuSCN/Au	1.000	21.90	75.80	15.60	[97]

Table 2.2 Current state of the art for the various electron transport layer for perovskite solar cell

ETM Type	Device Structure	V_{OC}	J_{SC}	FF	η	References
STO	FTO / STO/$Cs_{0.07}FA_{0.73}MA_{0.70}PbI_{2.53}Br_{0.47}$/SpiroOMeTAD/Au	1.14	23.021	72.10	19.0	[98]
STO	FTO/c-TiO_2/mp-STO/$CH_3NH_3PbI_{3-x}Cl_x$/Spiro-OMeTAD/Au	0.93	14.85	54.60	7.55	[99]

SnO_2	FTO/SnO_2 / $CH_3NH_3PbI_{3-x}Cl_x$/SpiroOMeTAD /Au	1.13	22.34	76.00	19.22	[100]
SnO_2	FTO/SnO_2/$(FAPbI_3)(MAPbBr_3)_{0.15}$/SpiroOMeTAD /Au	1.14	21.30	0.74	18.40	[101]
IGZO	ITO/IGZO/Perovskite/Spiro-OMeTAD/Au	1.14	22.70	66.82	17.36	[102]
IGZO	ITO/IGZO/Perovskite/Spiro-OMeTAD/Au	1.10	20.47	67.04	15.11	[103]
PCBM	ITO/PEDOT:PSS/ $CH_3NH_3PbI_{3-x}Cl_x$/PCBM/Ag	0.95	17.08	61.80	10.05	[104]
PCBM	ITO/PEDOT:PSS/$CH_3NH_3PbI_3$/PCBM/ZnO/ITO	0.87	11.20	67	6.5%	[105]
WS_2	ITO/WS_2/perovskite/SpiroOMeTAD	1.12	22.24	0.73	18.21	[106]
ZnSe	FTO/ZnO/ZnSe/CH3NH3PbI3/SpiroOMeTAD/Au	0.94	20.75	0.57	11.10	[107]
ZnSe	ITO/PTAA/perovskite/C60/ZnSe/Ag[108]	1.09	21.89	0.72	17.16	[109]
TiO_2	FTO/bl- TiO_2/mp- TiO_2 /$FAPbI_3$/SpiroOMeTAD/ Au	1.08	23.83	76.00	19.71	[110]
TiO_2	FTO/bl- TiO_2/mp- TiO_2 /perovskite/PTAA/Au	1.06	24.70	77.50	20.20	[111]
TiO_2	TiO_2 /$MAPbI_3$/PTAA/Au	1.10	20.40	75.00	16.80	[112]
ZnO	ITO/ZnO/$CsPbI_2Br$/SpiroOMeTAD/Ag	1.20	14.77	78.53	13.92	[113]
ZnO	FTO/ZnO/perovskite/SpiroOMeTAD/Ag	1.13	17.29	66.92	13.04	[108]
ZnO	ITO/PEDOT:PSS/perovskite/ZnO	0.81	10.40	28	2.4	[114]

2.1.7 All-Perovskite Tandem/Multijunction Solar Cell

The multijunction solar cell consists of the combination of wide and narrow bandgap material that allows the effective absorption of wider (high energy photons and low energy photons) portion of visible spectrum eventually leads to the enhancement of the device photovoltaic performance. However, the charge recombination layer is also considered as one of the most crucial constraints to effectively realize all-perovskite multijunction solar cells. To effectively utilize the function of multijunction solar cells it should possess low fabrication cost, compatibility with the adjacent layers, better optical management as well as wide-scale manufacturing ability. For a constructive realization of the solar cell, several strategies are utilized such as bulk passivation strategy [37], halide alloying [35], mixed cation engineering [36][38], use of nucleation layer *etc* [115]. A detailed literature survey adopting these strategies are mentioned below.

Madan *et al.* simulate the two-terminal all-perovskite tandem solar cells by considering $Cs_2AgBi_{0.75}Sb_{0.25}Br_6$ as the top subcell having 1.8 eV bandgap and $FACsPb_{0.5}Sn_{0.5}I_3$ as the bottom subcell with a bandgap of 1.2 eV are considered. Primary, each standalone structure is simulated and the device photovoltaic performance is measured. Both the standalone structure are optimized based on their thickness and the optimized thickness of 380 nm and 400 nm is obtained for the top and bottom subcell [40].

Jiang *et al.* synthesized the charge recombination layer (CRL) for two-terminal perovskite-perovskite tandem solar cells using the solution processing method. The proposed CRL comprises Spiro-OMeTAD/PEDOT:PSS/PEI/PCBM:PEI which permits efficient recombination of charges. In addition, the proposed CRL prevent the perovskites layer from degradation as the processing of the perovskite layer is crucial [40]**.**
Noteworthy, to maintain the J_{SC} of the solar cell the bottom subcell fabrication should be smooth and non-porous in nature. Moreover, the device performance is compared based on the different electrodes such as Ag and highly conductive (hc)-PEDOT:PSS electrode, in which the hc-PEDOT:PSS show inferior J_{SC} as compare to the Ag based electrode. In the case of single-junction solar cell, the Ag and highly conductive (hc)-PEDOT:PSS exhibits 11.7% PCE and 10.1% PCE. Further, the ETM is changed from PCBM to PEI:PCBM and the device performance improves significantly and reaches up to 11.4% and 8.3% in the case of the top subcell. Further, the tandem perovskite solar cell is

explored which depicts the PCE of 7 % with the open-circuit voltage of 1.89 V which is the addition of the two sub-cell of the perovskite solar cell [46].

Im *et al.* realized a perovskite-perovskite tandem structure by laminating and pressing technique of the top and bottom subcells. The tandem device configuration consists of FTO/bl-TiO_2/$MAPbBr_3$/hole conductor/PCBM/$MAPbI_3$ perovskite/PEDOT:PSS/ITO. To the efficient realization of the series tandem cell, a recombination layer is considered as the tandem solar cell mainly influenced by effective charge carrier transportation and recombination. Moreover, the HTL with some additives exhibits better photovoltaic performance as compare to the HTL without additives. For this purpose, they considered the HTM with Li-TFSi and t-BP as a conductive layer additive that enhances hole conductivity and allows high transportation of holes resulted to the improvement in the device photovoltaic performance. The tandem solar cell shows V_{OC} and J_{SC} of 2.25 Volts, 8.3 mA/cm^2 respectively. However, the FF and η obtained for a tandem solar cell are 56% and 10%. Surprisingly, it is obtained that the tandem cell shows high V_{OC} but exhibit less efficiency as compare to their standalone perovskite structure. This is basically due to the improper working of the recombination layer and lesser hole conductivity of the hole transport layer [34].

Rajagopal *et al.* investigated an integrated perspective to improve the tandem solar cell open-circuit voltage by bandgap engineering optimization along with smaller loss in V_{OC}. For the suitability of tandem structure initially, the wide (1.8 eV) and narrow (1.2 eV) bandgap layers are studied and optimized. The $MAPbSn_{0.5}I_3$ based perovskite layer is considered for the application of a narrow bandgap perovskite layer with a bandgap of 1.2 eV. In the case of the narrow bandgap perovskite solar cell, C_{60} is considered as an ETL which provide the PCE even less than 10 %. To alleviate the PV performance of $MAPbSn_{0.5}I_3$ based perovskite layer, the C_{60} layer is replaced with another fullerene based indene-C_{60}-bis-adduct $IC_{60}BA$ as an ETL layer and PEDOT:PSS as an HTL layer is considered [35].

Eperon *et al.* fabricate two-terminal (2T) and four-terminal (4T) perovskite solar cells. In the realization of two-terminal tandem solar cell, the narrow bandgap absorber layer ($FA_{0.75}Cs_{0.25}Sn_{0.5}Pb_{0.5}I_3$) possess a bandgap of 1.2 eV with 14.8% PCE. In the case for wide bandgap absorber layer ($FA_{0.83}Cs_{0.17}Pb(I_{0.5}Br_{0.5})_3$), it exhibits the bandgap of 1.8 eV

which depicts the PCE of 17.5% in a standalone configuration. Further, using these combinations the tandem perovskite solar cell is implemented with the device efficiency of 20.3% [36].

Zhao *et al.* propose an opportunity to reduce the electronic disorder of low bandgap perovskite layer $(FASnI_3)_{0.6}(MAPbI_{3-x}Cl_x)_{0.4}$ by incorporation of the chlorine (Cl) using bulk passivation strategy. This bulk passivation strategy allows the facile fabrication of a low bandgap (1.25 eV) perovskite layer without the suffering of the voltage and fill factor loss. Further, the proposed low bandgap perovskite layer is combined with the top perovskite layer along with the interconnecting layer between to realize a mixed Sn-Pb based tandem solar cell which depicts the 21% PCE [37].

Later, the all-perovskite 2T tandem solar cell is fabricated with 1.75 eV and 1.25 eV (2.5% of Cl) top and bottom subcell. The obtained tandem solar cell presents the 21% PCE. The limited PCE is attained due to the open-circuit voltage loss on the top subcell and the limited short circuit current density of the bottom subcell. This is mainly due to the halide segregation of the wide bandgap absorber layer. Hence it is concluded by the author's that the presented work opens a new opportunity for the development of highly efficient all-perovskite tandem solar cells [37].

Tong *et al.* perform an attempt to enhance the device performance of PCE of tandem solar cells greater than 30% for Pb and Sn based PSC. To enhance the device performance, the GauSCN is incorporated as an additive in the low bandgap sub cell ($(FASnI_3)_{0.6}(MAPbI_3)_{0.4}$) of the tandem solar cell. It is revealed from the analysis that with the addition of GauSCN the structural, electrical, optical properties are improved due to the reduction of defect density of the absorber layer of around 10 times. This reduction of defect density of the low bandgap perovskite allows the enhancement of the PCE (at least > 20%) of the perovskite solar cell [38].

Palmstrom *et al.* propose an opportunity to overcome the major challenges occurs in the fabrication of all-perovskite tandem solar cell. These challenges include the formation of a facile recombination layer which prevents the damage of top cells while fabricating the bottom subcell[115]. The second challenge includes attaining the high open-circuit voltage from the wide bandgap perovskite layer. To overcome these challenges, they

develop a novel strategy that includes improvement of the nucleation properties of buffer layer prepared via atomic layer deposition (ALD). For the low bandgap perovskite $FACsPbI_3$ layer is considered with the bandgap of 1.27 eV. Generally, the range of wide-bandgap perovskite lies in the range of 1.7 eV to 1.85 eV along with the inclusion of halide content such as Br in it. It is obtained from the literature that the presence of Br content led to the halide segregation of the perovskite layer which in turn reduces the open-circuit voltage and degrades the stability of the solar cell. To mitigate these issues, the bandgap widening method is introduced by mixing the dimethylammonium formamidinium and cesium (DMA and Cs) to form 1.7eV $FA_{0.6}Cs_{0.3}$ $DMA_{0.1}$ $Pb_{0.4}$ $Br_{0.6}$ perovskite layer. Further, using these combinations of layers (DMA modified perovskite) the tandem solar cell is fabricated which enhance the PCE up to 23.1% [115].

Singh *et al.* investigated the drift-diffusion model based all-perovskite tandem solar cell by optimizing the thickness and bandgap of top and bottom subcell. The cell architecture consists of C60 (ETL)/bottom cell perovskite/ HTL (PEDOT:PSS)/recombination layer/ETL (PCBM)/top cell perovskite/HTL (NiO).By using drift-diffusion simulation model, the effect of interface and bulk defects, effect of the mobility of the perovskite layer is studied. In addition, the doping of the charge carriers, the effect of contact work function is investigated. It is obtained from the theoretical calculations, that with the thickness of 350 nm of each layer the maximum efficiency of 36.6% is achieved with the corresponding bandgap of top and bottom cell is 1.5 eV and 0.95 eV. Further, the traps are introduced between the perovskite /ETL and perovskite /HTL interface as well as in the bulk of the perovskite. The increment of traps leads to the reduction of the device performance. The optimized trap time of 10^{-9} s is obtained for the interface and for the bulk 5×10^{-7}s trap time is achieved. These combinations of trap time will eventually enhance the PCE, reaches up to 29.8% [116].

2.2 Research Gaps

- Regardless of the progressive achievement of the perovskite solar cell, toxicity remains a primary concern. Hence, the demand for lead-free perovskite solar cells attracted wide attention among researchers.

- Moreover, despite perovskite absorber layers, the charge transport layers also play a significant role in the perovskite performance. Depend on the band alignment, different charge transport layers possess different photovoltaic characteristics. Thus, there is a stringent requirement for the investigation of various charge transport layers on less explored perovskite layers.
- For the application of lead-free all-perovskite tandem solar cells, limited wide and narrow bandgap perovskite layers are explored. Hence there is a requirement to explore several other wide and narrow band gap perovskite alternatives for the application of lead-free tandem solar cells.
- Also, no literature is available to investigate the effect of charge transport layers on the all-perovskite tandem solar cell performance.

2.3 Research Objectives

- Design and simulation of perovskite solar cells using different high/low bandgap perovskite layers.
- Design and simulation of perovskite solar cells using different electron/hole transport layer combinations.
- Proposing a multijunction lead-free perovskite solar cell using a simulated structure.

2.4 Organization of Thesis

The thesis is summarized into the following chapters and the chapter wise summary is given below.

Chapter 1 includes the basic theoretical concepts of the solar cell. The different generation of the solar cell is presented in this chapter.

Chapter 2 presents a detailed literature review of the lead-free perovskite solar cell based on different perovskite layers. The chapter divides into subparts such as (i) Methylammonium tin halide ($CH_3NH_3SnI_3$) based perovskite solar cell (ii) Methylammonium germanium halide ($CH_3NH_3GeI_3$) based perovskite solar cell (iii)

Cesium tin-germanium triiodide ($CsSnGeI_3$) based perovskite solar cell (iv) Mixed germanium and tin halide ($FAMASnGeI_3$) based perovskite solar cell (v) Double-perovskite *i.e.,* mixed antimony bismuth halide ($Cs_2AgBi_{0.75}Sb_{0.25}Br_6$) based perovskite solar cell is presented. Moreover, the literature based on the all-perovskite tandem solar cell is also included in this chapter. In addition, the need for the study of lead-free perovskite solar cells, the identified research gaps, research objectives and the organization of the thesis is also documented in the chapter.

Chapter 3 presents the basic introduction of the software and further, the numerical simulation of lead-free wide and narrow bandgap perovskite layers for the application of perovskite solar cells. Further study includes the effect of several hole transport layers on standalone lead-free perovskite layers. In addition, the effect of each absorber layer defect density is studied. Moreover, the effect of the back electrode metal work function of the standalone structure is also explored. Additionally, the effect of temperature on standalone perovskite structure is studied.

Chapter 4 consists of a numerical simulation of the lead-free double-perovskite solar cell. In this study, the effect of different electron transport layers and the effect of the hole transport layer is realized by correlating the built-in potential with the open-circuit voltage. Later, the effect of lead-free double-perovskite absorber layer thickness is optimized to attain the optimum device efficiency of perovskite solar cells.

Chapter 5 includes the numerical simulation of the lead-free all-perovskite multijunction solar cell. The proposed study includes the effect of the electron transport layer on the photovoltaic performance of the solar cell. In addition, the effect of perovskite absorber layer thickness is also explored and optimized for multijunction perovskite solar cells. Moreover, the effect of absorber layers defects density on the photovoltaic performance is realized. Later, the effect of the front electrode work function is also explored. Our proposed work depicts all-perovskite multijunction solar cells with improved photovoltaic performance.

Lastly, in chapter 6 the concluding remarks and the future scope of the proposed work are presented.

2.5 Contribution of the Research Work

Depend on the proposed objectives the original contribution of the research work is listed below:

- This thesis provides an extensive simulation of the effect of different parameters of the various layers on lead-free perovskite solar cells performance.

- This thesis also suggests the different combinations of low and high band gap layers for high-efficiency multi-junction solar cells.

- The best possible charge transport layers for various perovskite layers based on extensive band alignment engineering is also a major contribution of this thesis.

CHAPTER 3

NUMERICAL SIMULATION OF HIGHLY EFFICIENT LEAD-FREE PEROVSKITE SOLAR CELLS

Numerical simulation plays a crucial role in the expansion of the photovoltaic industry as it allows the implementation of the complex mathematical model, provides an analytical solution as well as is desirable for a thorough understanding of the device performance. It is quite complicated to fabricate numerous combinations of the charge transport layer, perovskite absorber layers and hence the simulation of numerous layers is an efficient way to attain higher device performance. The numerical simulation method allows the researchers to save their fabrication cost and time at the same time allows it to pave a new path that will emphasize computer-based learning. The SCAPS 1D (solar cell capacitance simulator) is a one-dimensional tool, developed by Prof. Marc Bulgerman from the Department of Electronics and Information System, University of Ghent, Belgium (ELIS, Belgium). The SCAPS software is a window-oriented application program usually written in C code also freely and easily available [117][118]. The SCAPS was originally developed for CIGS (copper indium gallium arsenide) and CdTe (cadmium telluride) solar cells. Later, it was upgraded and made compatible to simulate other solar cell structures[119]. The SCAPS utilizes finite difference method to solve the differential equations. The software provides the analysis of semiconductor properties such as current density, carrier density, occupation probability of deep defects of carriers, energy band diagram analysis. Additionally, it also calculates the I-V (current-voltage) characteristics, solar cell photovoltaic parameters, QE (quantum efficiency) calculations. To analyze these basic semiconducting properties the material parameters are provided such as bandgap, electron affinity, conduction band density of states, valence band density of states, electron/hole thermal velocity, electron/hole mobility *etc*. It allows the calculation of current in both dark and light conditions. Several spectrums are provided for illumination purposes such as A.M 1.5G (Air mass 1.5 global), A.M 0, A.M.1.5 D, *etc*.
The SCAPS solves the basic semiconducting equations which are discussed below:

(1) Current density equation:

It is well evident that the current conduction inside the semiconductor mainly consists of two basic phenomena *i.e.,* drift current and diffusion current. The drift current is caused due to the electric field within a device and the concentration gradient present inside the semiconductor leading to the diffusion current as given by Eq. 3.1 and Eq. 3.2.

$$J_n = q\mu_n nE + qD_n\frac{dn}{dx} = q\mu_{n(}E + \frac{KTdn}{q\ dx})$$

Eq. 3.1

$$J_p = q\mu_p pE + qD_p\frac{dp}{dx} = q\mu_{p(}E + \frac{KTdp}{q\ dx})$$

Eq. 3.2

where,

E is defined as the electric field,

μ_n,μ_p are mobilities of electron and hole,

J_n, J_p are current densities for electron and hole,

D_n,D_p are diffusion constant for electron and hole, respectively.

(2) Continuity equation:

The semiconductor includes several transport mechanisms. The continuity equation is the time-dependent mechanism that includes the generation and recombination of charge carriers under low-level injection. Due to the drift, diffusion, direct and indirect generation and recombination mechanism, the carrier concentration varies with respect to time. The continuity equation is also explained as the net charge carrier concentration of the semiconductor is defined as the difference between the generation and recombination rate and the net current flowing inward and outward for a particular region. The continuity equation of the semiconductor is given by Eq. 3.3 and Eq. 3.4

$$-\frac{\partial J_n}{\partial x} - U_n + G = \frac{\partial n}{\partial t}$$

Eq. 3.3

$$-\frac{\partial J_p}{\partial x} - U_p + G = \frac{\partial p}{\partial t} \quad \textbf{Eq. 3.4}$$

where,

G is defined as the generation rate, and U_n,

U_p are recombination rates for electron/holes

(3) Poisson's equation:

Poisson's equation correlates the space charge distribution with the electrostatic potential. The Poisson's equation is given in Eq. 3.5

$$\frac{d^2\varphi}{dx^2} = -\frac{dE}{dx} = -\frac{\rho_s}{\epsilon} = -q\,(p - n + N_D - N_A) \quad \textbf{Eq. 3.5}$$

Φ is the electrostatic potential, N_D and N_A are the donor and acceptor carrier concentration.

3.1 Results and Discussion

This chapter includes the simulation study of perovskite solar cells using two standalone lead-free perovskite layers (*i.e.,* $CH_3NH_3GeI_3$ and $CsSnGeI_3$ based perovskites). Further investigation includes, the studies of the effect of different hole transport layers, absorber defect density, metal work function and the effect of temperature for both $CH_3NH_3GeI_3$ and $CsSnGeI_3$ based perovskite layers. However, initially, to optimize the performance of Pb-free , the numerical simulation is validated by regenerating the experimental results performed by Zhou.*et al.* as shown in Fig. 3.1[120]. The result shows the close match between the simulated results and the experimental ones.

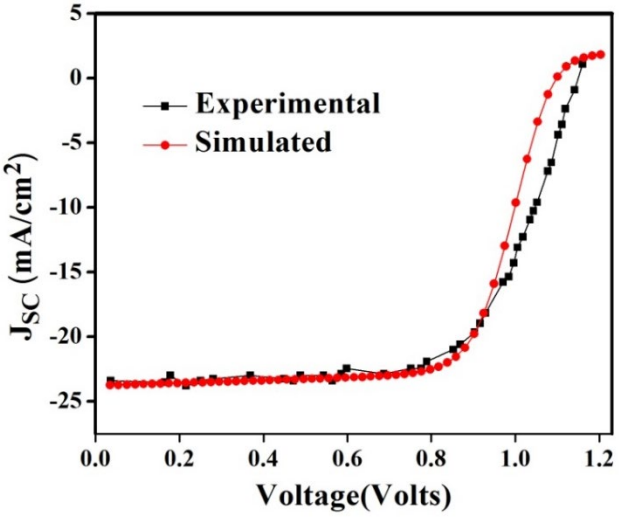

Fig. 3.1. Verification of simulated results to the experimental results[120]

3.2 Device Structure

For simulation, the device parameters chosen are given in Table 3.1- 3.2. Initially, the simulations of $CH_3NH_3GeI_3$ and $CsSnGeI_3$ based perovskite structures have been carried out and their performance parameter have been measured. The device structure of $CH_3NH_3GeI_3$ and $CsSnGeI_3$ based perovskite structures are shown in Fig. 3.2(a-b).

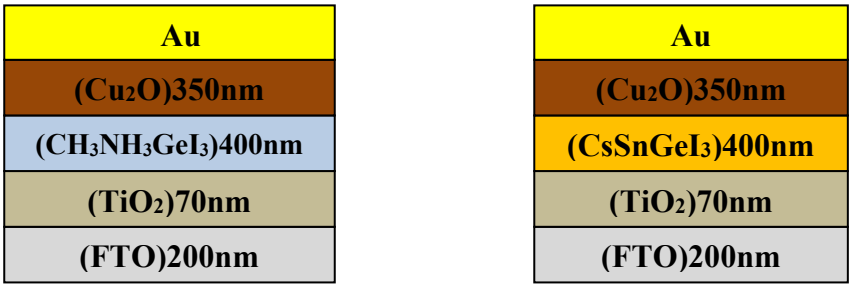

Fig. 3.2. Structures of the simulated configuration (a) $CH_3NH_3GeI_3$ based (b) $CsSnGeI_3$ based perovskite solar cells

Table 3.1 Device material parameters of the hole transport layer, absorber layers, electron transport layer and transparent conductive oxide

Parameters	Cu_2O	$CH_3NH_3GeI_3$	$CsSnGeI_3$	TiO_2	TCO
Thickness (μm)	0.350	0.400	0.400	0.070	0.200
Band gap(eV)	2.17	1.900	1.5	3.200	3.500
Electron affinity (eV)	3.2	3.98	3.9	3.9	4.00
Dielectric Permittivity	7.11	10.00	28	32.00	9.00
Conduction Band Density of States (N_c) (cm^{-3})	2.02×10^{17}	1×10^{16}	3.1×10^{18}	1×10^{19}	2.2×10^{18}
Valence Band Density of States (N_v) (cm^{-3})	1.1×10^{19}	1×10^{16}	3.1×10^{18}	1×10^{19}	1.8×10^{19}
Electron thermal velocity (cm/s)	1×10^{7}	1×10^{7}	1×10^{7}	1×10^{7}	1×10^{7}
Hole Thermal Velocity (cm/s)	1×10^{7}	1×10^{7}	1×10^{7}	1×10^{7}	1×10^{7}
Electron mobility (cm^2/Vs)	200	1.62×10^{5}	974	20	20
Hole mobility (cm^2/Vs)	80	1.01×10^{5}	213	10	10
N_D (cm^{-3})	0	1×10^{9}	0	1×10^{17}	1×10^{18}
N_A (cm^{-3})	1×10^{18}	1×10^{9}	1×10^{14}	0	0
N_t(cm^{-3})	1×10^{14}	1×10^{16}	1×10^{16}	-	-
References	[121]	[53]	[66]	[53]	[122]

Table 3.2 Numerical parameters taken for different HTM

Parameters	Spiro-OMeTAD	PEDOT:PSS	NiO	CuI	CZTSe	P3HT
Thickness (μm)	0.350	0.350	0.350	0.350	0.350	0.350
E_g(eV)	3.06	2.2	3.8	2.98	1.4	1.85
qχ (eV)	2.45	2.9	1.46	2.1	4.1	3.1
Dielectric Permittivity	3	3	10.70	6.5	9	3.4
N_c(cm^{-3})	2.2×10^{18}	2.2×10^{15}	2.8×10^{19}	2.8×10^{19}	2.2×10^{18}	1×10^{22}
N_v (cm^{-3})	1.8×10^{19}	2.2×10^{17}	1×10^{19}	1×10^{19}	1.8×10^{19}	1×10^{22}
Electron Thermal Velocity (cm/s)	1×10^{7}	1×10^{7}	1×10^{7}	1×10^{7}	1×10^{7}	1×10^{7}
Hole Thermal Velocity (cm/s)	1×10^{7}	1×10^{7}	1×10^{7}	1×10^{7}	1×10^{7}	1×10^{7}
Electron mobility (cm^2/Vs)	2×10^{-4}	2	12	1.7×10^{-4}	100	1×10^{-4}
Hole mobility (cm^2/Vs)	2×10^{-4}	2	2.8	2×10^{-4}	12.5	1×10^{-3}
N_A (cm^{-3})	2×10^{18}	1×10^{17}	1×10^{18}	1×10^{18}	1×10^{19}	3.17×10^{13}
References	[53]	[122]	[123]	[122]	[123]	[124]

Initially, the simulation of perovskite solar cells using individual layer $CsSnGeI_3$ with low band gap and $CH_3NH_3GeI_3$ having high band gap have been performed. The perovskite absorber thickness is kept constant at 400 nm during the simulation. However, the absorber defect density of $CH_3NH_3GeI_3$ and $CsSnGeI_3$ perovskite layers have been

considered as 1×10^{16} cm^{-3} as shown in Table 3.1. Fig. 3.3 shows the J-V characteristics of the simulated PSC. It has been elucidated from the J-V curve of both the structure that organic $CsSnGeI_3$ based devices exhibit better device performance than $CH_3NH_3GeI_3$ perovskite solar cells. As shown in Fig. 3.3a, using methyl ammonium germanium halide the device achieves maximum efficiency of 18.01% (V_{OC} =1.34 V, J_{SC}= 15.55 mA/cm^2, fill factor (FF) =82.73%). However, tin-based configuration achieved efficiency of 20.58% (V_{OC} =1.00 V, J_{SC}= 25.75 mA/cm^2 and FF =79.21%) as shown in Fig. 3.3b. The V_{OC} value for $CH_3NH_3GeI_3$ is 1.34 V whereas 1 V of V_{OC} is obtained for $CsSnGeI_3$ based perovskite solar cells. This is mainly due to the fact, that $CH_3NH_3GeI_3$ has a higher band gap as compared to the $CsSnGeI_3$. However, the J_{SC} value is very less for $CH_3NH_3GeI_3$ as compare to the $CsSnGeI_3$ based PSC. This is mainly due to the fact, that the $CH_3NH_3GeI_3$ based perovskite solar cells absorb less solar spectrum as compare to the $CsSnGeI_3$ based perovskite solar cells.

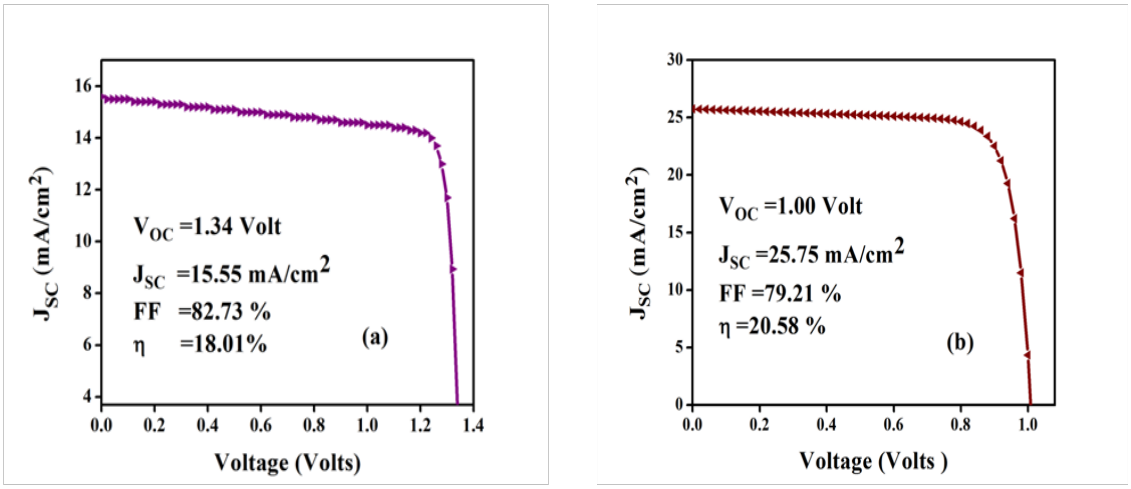

Fig. 3.3. J-V curve of (a) $CH_3NH_3GeI_3$ based solar cell (b) $CsSnGeI_3$ based solar cell

Further, the PV performance of the different PSCs ($CH_3NH_3GeI_3$ and $CsSnGeI_3$) has been explored in terms of the different HTL (hole transport layer), the defect density of perovskite layers, metal work function, and the temperature.

3.3 Effect of Different HTL (Hole Transport Layer) on the Photovoltaic Performance of Perovskite Solar Cells

The different HTLs have been taken to further simulate the individual $CH_3NH_3GeI_3$ and $CsSnGeI_3$ based PSC as given in Fig. 3.4(a-f) and Fig. 3.8(a-f). The layers are arranged according to their electron affinity and band gap. The energy band alignment diagram for $CH_3NH_3GeI_3$ based PSC is shown in Fig. 3.4(a-f). However, the obtained EBD from simulation for $CH_3NH_3GeI_3$ based PSC is shown in Fig. 3.5(a-f). However, Table 3.3 shows the obtained photovoltaic parameters of different HTLs for $CH_3NH_3GeI_3$ based perovskite solar cells. Fig. 3.6 (a-b) shows the obtained photovoltaic parameters for $CH_3NH_3GeI_3$ based perovskite solar cell whereas Fig. 3.7 shows the J-V curve of the different HTL for $CH_3NH_3GeI_3$ based PSC.

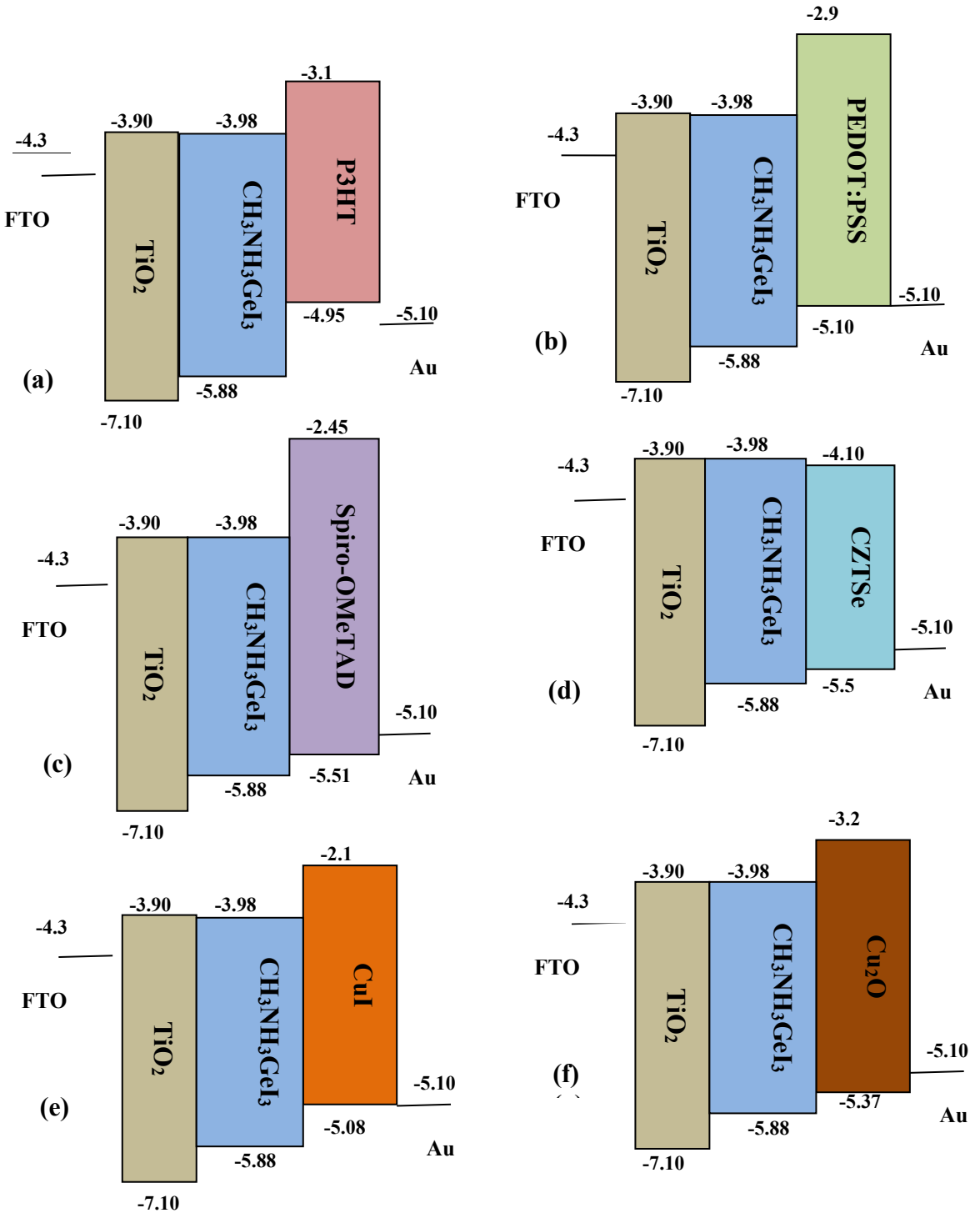

Fig. 3.4. Energy band alignment diagram of different HTL for the simulation of $CH_3NH_3GeI_3$ based PSC (a) P3HT (b) PEDOT:PSS (c) spiro-OMeTAD (d) CZTSe (e) CuI (f) Cu_2O

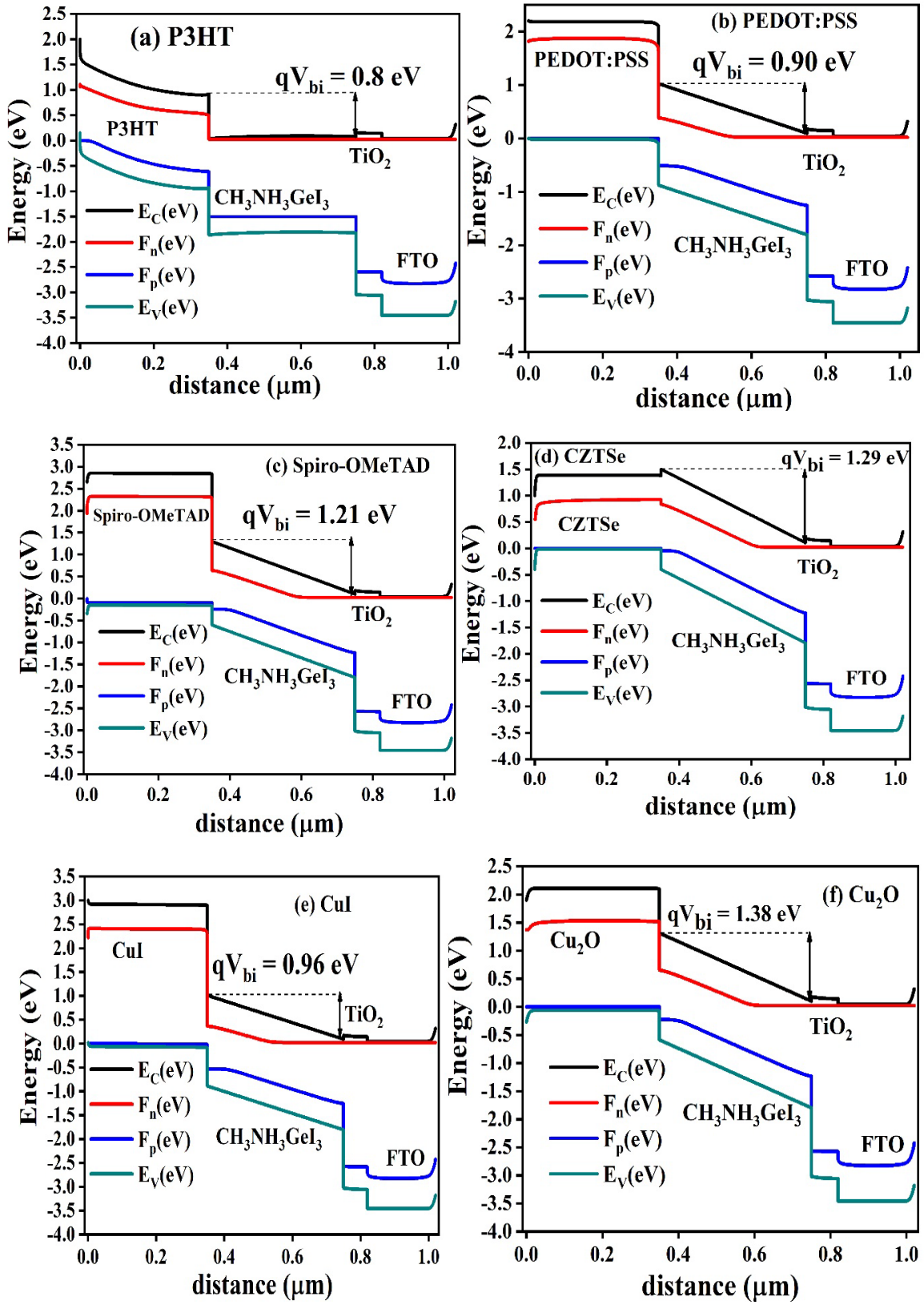

Fig. 3.5. Energy band diagram of different hole transport layer for $CH_3NH_3GeI_3$ based perovskite solar cell (a) P3HT (b) PEDOT:PSS (c) spiro-OMeTAD (d) CZTSe (e) CuI (f) Cu_2O

Table 3.3 Effect of E_{C_ETL}- E_{V_HTL}, ϕ_{BC}-E_{C_ETL}, V_{bi}, V_{OC}, J_{SC}, FF, η on the device photovoltaic performance on $CH_3NH_3GeI_3$ based perovskite solar cell

Different HTL layers	E_{C_ETL} – E_{V_HTL} (eV)	Φ_{BC}-E_{C_ETL} (eV)	V_{bi} (V)	V_{OC} (Volts)	J_{SC} (mA/cm^2)	FF (%)	η (%)
P3HT	1.05	1.20	0.80	0.87	15.40	47.44	6.61
PEDOT:PSS	1.20	1.20	0.90	1.11	15.54	81.77	14.74
Spiro-OMeTAD	1.41	1.20	1.21	1.39	15.55	78.82	17.79
CZTSe	1.60	1.20	1.29	1.14	15.51	83.22	15.33
CuI	1.18	1.20	0.96	1.05	15.55	81.23	13.90
Cu_2O	1.47	1.20	1.38	1.34	15.55	82.73	18.01

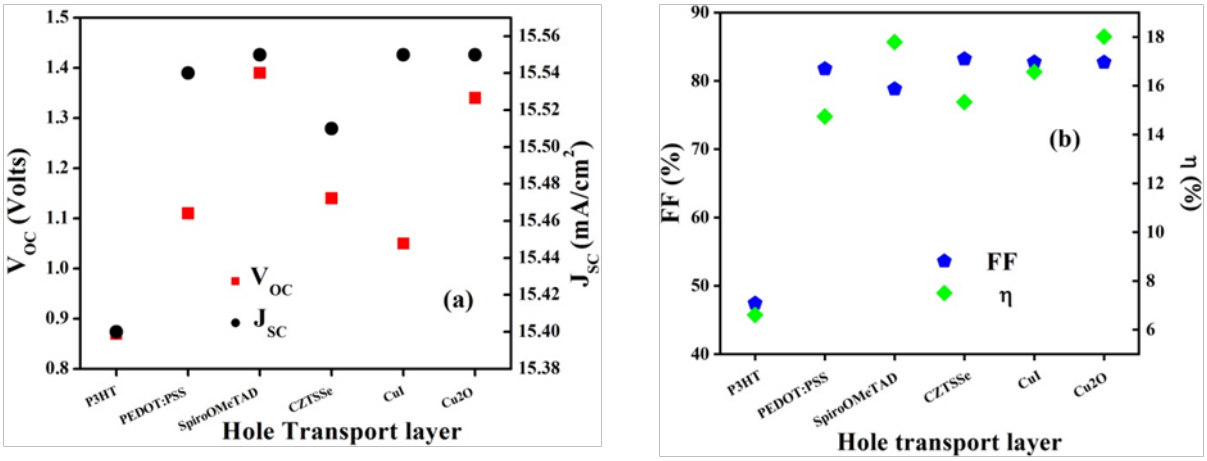

Fig. 3.6 Simulated result for $CH_3NH_3GeI_3$ based perovskite solar cell (a) V_{OC} and J_{SC} (b) FF and η

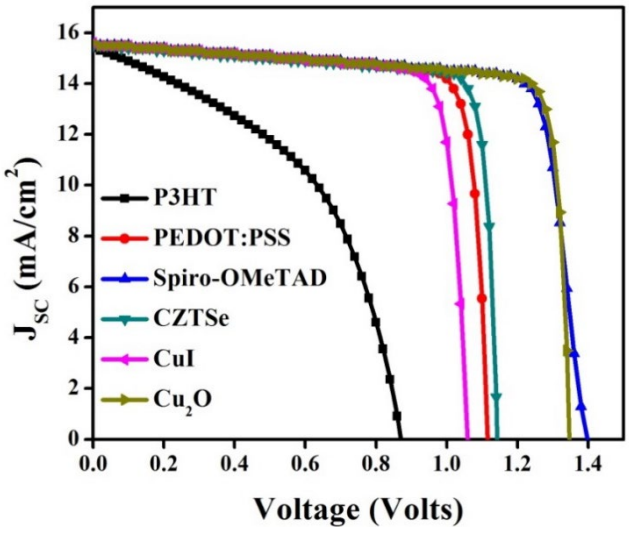

Fig. 3.7. Simulated J-V curve for different HTL on $CH_3NH_3GeI_3$ based perovskite layer

The hole transport layers are optimized by correlating the built-in potential (V_{bi}) to the open-circuit voltage (V_{OC}), where V_{bi} is defined as the energy level difference between conduction band energy level between perovskite and ETL interface to the perovskite and HTL interfaces ($E_{C\_PVK/ETL} - E_{C\_PVK/HTL}$) divided by elementary charge q. It has been obtained from Table 3.3 that for $CH_3NH_3GeI_3$ based perovskite layer, P3HT shows the lowest photovoltaic performance whereas Cu_2O depicts the highest photovoltaic performance which elevates the efficiency from 6.61% to 18.01% for $CH_3NH_3GeI_3$ based perovskite layer as given in Table 3.3. The lowest PV performance of P3HT is due to the E_{C_ETL}-E_{V_HTL} = 1.05 eV which shows V_{bi} up to 0.8 eV and thus reduces the V_{OC} to 0.87 eV. However, the obtained result for P3HT is the worst among all hole transport layers. The poor device performance of P3HT is due to the non–linear behaviour of its conductivity versus doping concentration[125]. One cannot enhance the doping concentration of P3HT from a certain value as it decreases the conductivity of the film which will reduce the PV performance of the solar cell[126]. Apart from the doping concentration, low charge carrier mobility (electron mobility: $1\times10^{-4}cm^2/Vs$ and hole mobility: $1\times10^{-3}cm^2/Vs$) is another reason which limits its V_{OC} up to 0.81 Volts. In the case of Cu_2O, the highest V_{bi} is attained *i.e.,* 1.38 eV which increases the V_{OC} to 1.34 Volts. In addition, spiro-OMeTAD shows the highest V_{OC} of 1.39 eV but less power conversion efficiency (η) 17.79 % is attained as compare to Cu_2O based hole transport layer (η = 18.01%). This is mainly because of the low charge carrier mobility of spiro-

OMeTAD (2×10^{-4} cm^2/Vs) as compare to Cu_2O as the carrier gets lost before reaching the destination electrodes. However, the highest V_{OC} of spiro-OMeTAD is mainly because it created a very good barrier for electron as it restricts the electron travel towards HTL. The limited photovoltaic performance of PEDOT:PSS is due to the barrier between HTL/ϕ_{BC} interface. As compared to Cu_2O, CuI and CZTSe shows poor photovoltaic performance due to their lower V_{bi} and thus reducing its V_{OC} and efficiency. It is obtained from Fig. 3.5 and Table 3.3 that Cu_2O shows the better V_{bi}, as well as good charge carrier mobility for $CH_3NH_3GeI_3$ based perovskite solar cell and hence, shows comparatively better PV performance as compare to other HTLs.

Furthermore, the effect of different hole transport layers on the photovoltaic performance of $CsSnGeI_3$ based PSC is also explored. The energy band alignment diagram for $CsSnGeI_3$ based PSC is shown in Fig. 3.8(a-f). However, the obtained energy band diagram from simulation for $CsSnGeI_3$ based PSC is shown in Fig. 3.9(a-f). However, Table 3.4 shows the obtained photovoltaic parameters of different HTLs for $CsSnGeI_3$ based perovskite solar cells. Fig. 3.10(a-b) shows the obtained photovoltaic parameters for $CsSnGeI_3$ based perovskite solar cell whereas Fig. 3.11 shows the J-V curve of the different HTL for $CsSnGeI_3$ based PSC. It has been obtained from the simulation when $CsSnGeI_3$ based perovskite layer is used for perovskite solar cell the final device photovoltaic performance is enhanced. This is mainly attributed to the suitable bandgap of $CsSnGeI_3$ based perovskite solar cell which is 1.4eV, which is considered almost an ideal bandgap for absorber layers. A detailed study using different hole transport layers is presented in this section. Similar to $CH_3NH_3GeI_3$, in the case of $CsSnGeI_3$ as well, the P3HT shows the worst device performance, which is mainly due to its non–linear behaviour of its conductivity versus doping concentration as mentioned in the case of $CH_3NH_3GeI_3$ based perovskite solar cell[126]. Also, it has been explored from the literature, that one cannot enhance the doping concentration of P3HT from a certain value as it decreases the conductivity of the film which will reduce the PV performance of the solar cell[126]. Apart from the doping concentration, low charge carrier mobility (electron mobility: 1×10^{-4} cm^2/Vs and hole mobility: 1×10^{-3} cm^2/Vs) of P3HT is another reason which limits its V_{OC} to 0.81 Volts. In addition, the limited device performance of PEDOT:PSS on $CsSnGeI_3$ based PSC is due to its low charge carrier mobility, which impedes the carrier to get collected at the electrodes. As given in Table 3.4, spiroOMeTAD and CZTSe show almost analogous V_{bi} and hence similar V_{OC} are

obtained. However, the photovoltaic performance of spiro-OMeTAD is inferior to that of CZTSe mainly due to its smaller hole and electron mobility (2×10^{-4} cm^2/Vs). From the correlation between the V_{bi} and V_{OC}, it is expected that CuI shows similar photovoltaic performance (*i.e.*, power conversion efficiency) to that of CZTSe, but the photovoltaic performance of CuI based HTL layer is quite less as compare to the CZTSe hole transport layer. The low photovoltaic performance of CuI is due to the lower charge carrier mobility of CuI ($\sim10^{-4}$ cm^2/Vs) which limits the overall device performance. The hole transport layer that shows better device photovoltaic performance of $CsSnGeI_3$ based layer is also Cu_2O as shown in Fig. 3.10 and Fig. 3.11, which is due to its higher V_{bi} as given in Table 3.4 and thus resulted in V_{OC} of 1.00 Volts. The Cu_2O depicts better photovoltaic performance among all other HTLs because of its better band alignment with the perovskite layer and back contact, and high charge carrier mobility. Hence, Cu_2O is considered as a hole transport layer for both $CH_3NH_3GeI_3$ as well as $CsSnGeI_3$ based perovskite solar cells. However, it is already shown in the literature that the Cu_2O layer can be compatible with low–temperature solution-processed method [127] and thus Cu_2O as an HTM is taken further to study perovskite layers.

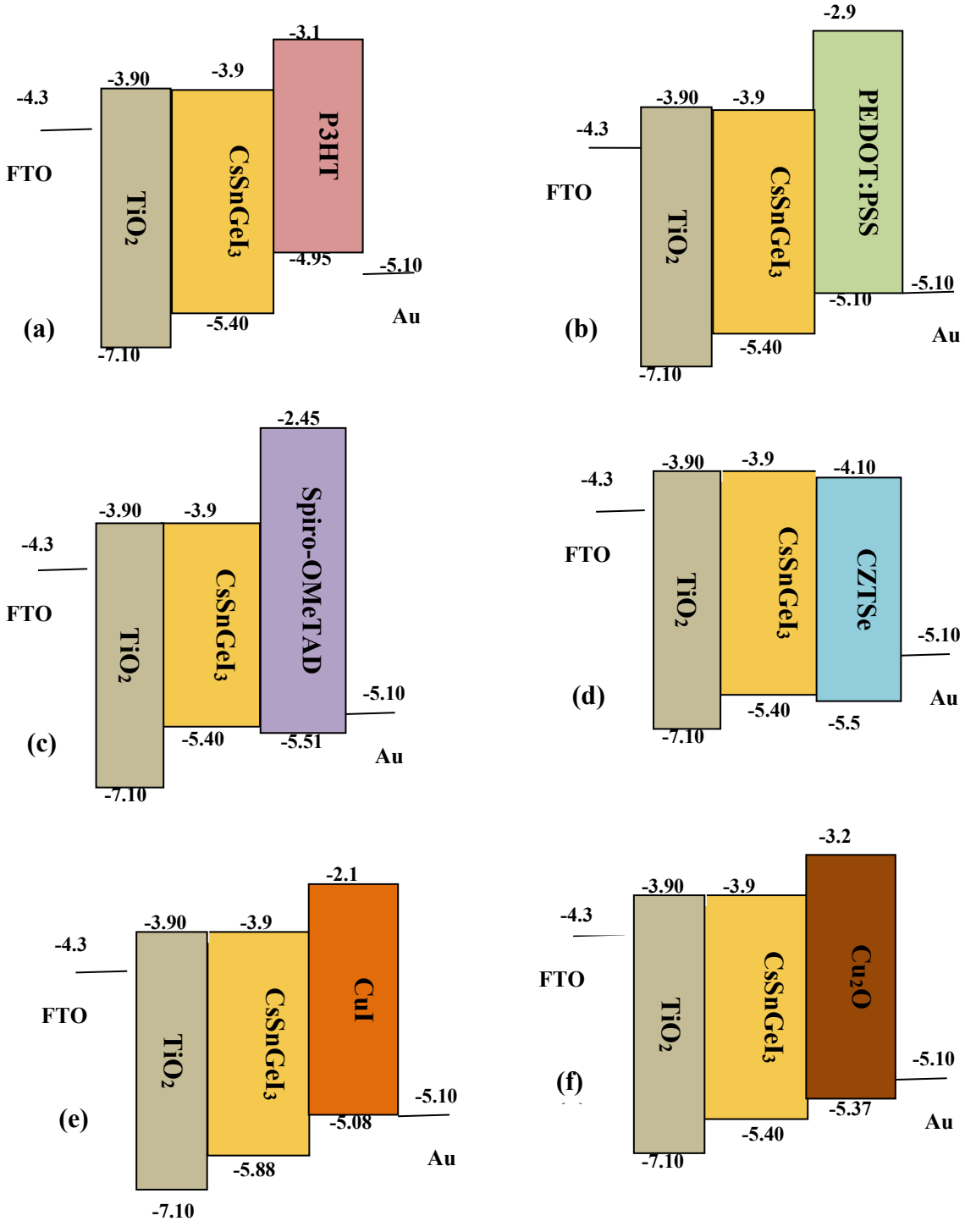

Fig. 3.8. Energy band alignment diagram of different HTL for $CsSnGeI_3$ based perovskite solar cell (a) P3HT (b) PEDOT:PSS (c) Spiro-OMeTAD (d) CZTSe (e) CuI (f) Cu_2O

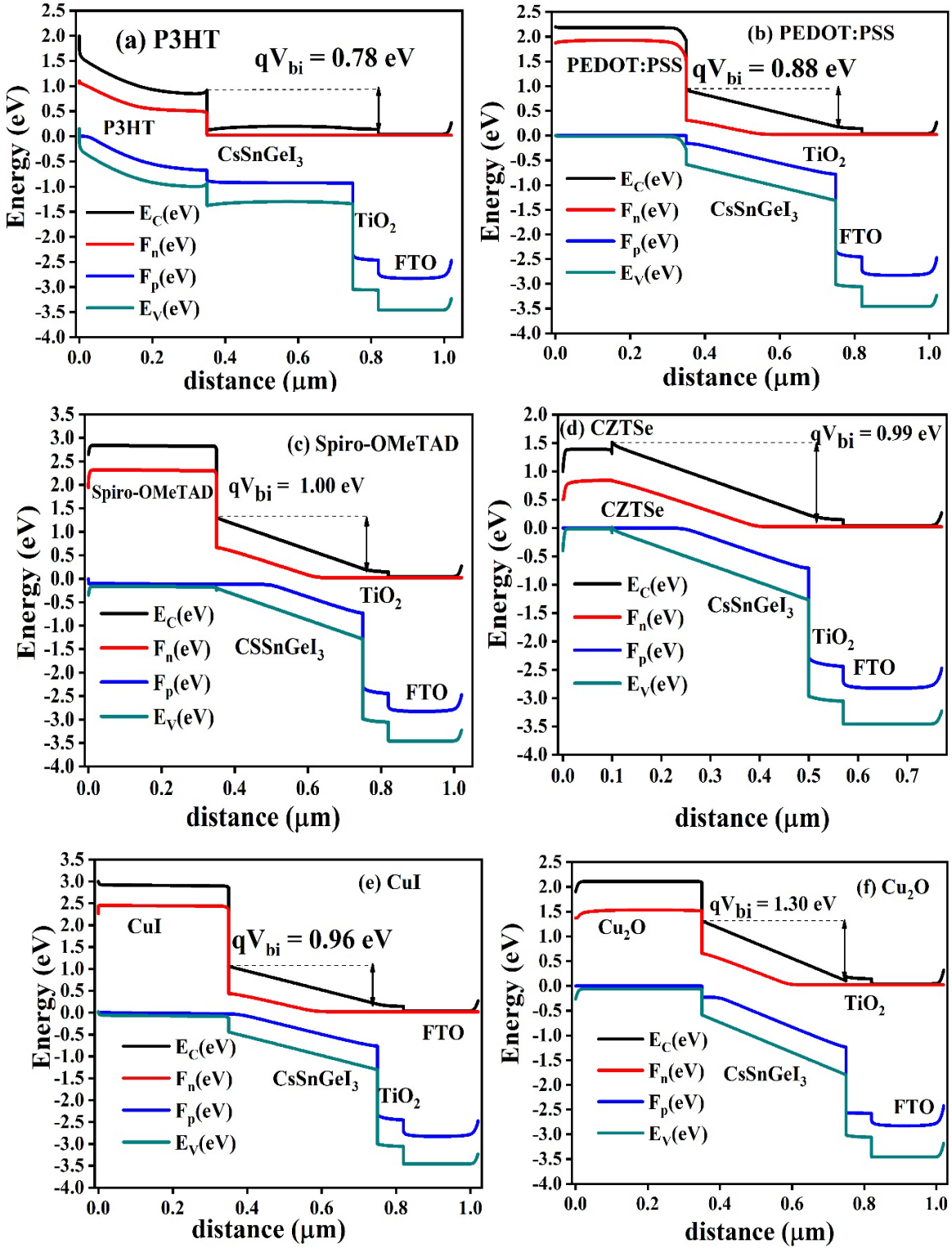

Fig. 3.9. Energy band diagram of different HTL for $CsSnGeI_3$ based PSC (a) P3HT (b) PEDOT:PSS (c) spiro-OMeTAD (d) CZTSe (e) CuI (f) Cu_2O

Table 3.4 Effect of E_{C_ETL}- E_{V_HTL}, ϕ_{BC}-E_{C_ETL}, V_{bi}, V_{OC}, J_{SC}, FF, η on the device photovoltaic performance on $CsSnGeI_3$ based perovskite solar cell

Different HTL layers	E_{C_ETL}- E_{V_HTL} (eV)	Φ_{BC}- E_{C_ETL} (eV)	V_{bi} (V)	V_{OC} (Volts)	J_{SC} (mA/cm^2)	FF (%)	η (%)
P3HT	1.05	1.20	0.78	0.83	19.68	48.02	7.90
PEDOT:PSS	1.20	1.20	0.88	0.96	25.66	78.48	19.37
Spiro-OMeTAD	1.61	1.20	1.00	0.98	25.77	70.84	17.98
CZTSe	1.60	1.20	0.99	1.00	25.69	79.92	20.61
CuI	1.18	1.20	0.96	0.96	25.74	75.21	18.70
Cu_2O	1.47	1.20	1.30	1.00	25.75	79.22	20.58

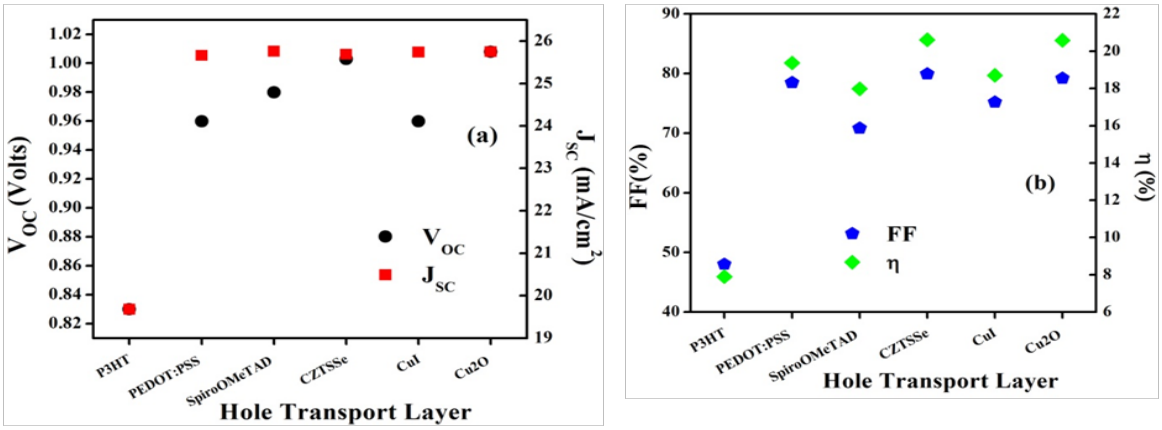

Fig. 3.10. Simulated result for $CsSnGeI_3$ based perovskite solar cell (a) V_{OC} and J_{SC} (b) FF and η

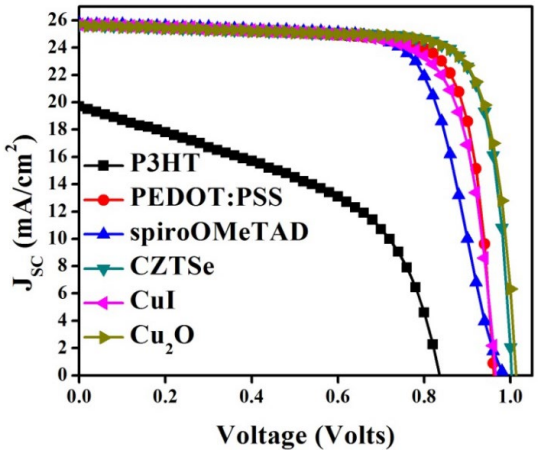

Fig. 3.11. Simulated J-V curve for different HTL on $CsSnGeI_3$ based perovskite layer

3.4 Effect of Absorber Defect Density on Lead-Free ($CH_3NH_3GeI_3$ and $CsSnGeI_3$) Perovskite Solar Cells

The defect density of the individual layers play a significant role in the performance of the solar cells as it increases the recombination centre in the layer. The Schockley–Read–Hall (SRH) recombination model has been employed to study the effect of defect density of the absorber layer on the performance of solar cells as given in Eq. 3.6 and Eq. 3.7.

$$R_{SRH} = \frac{np - n_i^2}{\tau_p(n + n_i) + \tau_n(p + p_i)} \qquad \textbf{Eq. 3.6}$$

and $$\tau_{n,p} = \frac{1}{\sigma v_{th,n,p} N_t} \qquad \textbf{Eq. 3.7}$$

where,

R_{SRH} is the Schockley–Read–Hall recombination rate,

n and p are the concentration of electron and hole,

τ_p,τ_n are the lifetime of hole and electron.

The influence of defect density on the device photovoltaic performance on two different configurations, *i.e.,* ($CH_3NH_3GeI_3$ and $CsSnGeI_3$) is studied. The initial defect density of both the perovskite layer is considered as 1×10^{16} cm^{-3} as shown in Table 3.1. Initially, the defect density of $CH_3NH_3GeI_3$ based perovskite solar cell is altered from 1×10^{14} cm^{-3} to 1×10^{19} cm^{-3} as shown in Fig. 3.12a and Fig. 3.12b. It has been observed that as the defect

density of $CH_3NH_3GeI_3$ based perovskite absorber layer has been increased from 1×10^{14} cm^{-3} to 1×10^{19} cm^{-3}, the V_{OC} has been decreased from 1.35 V to 1.30 V, and J_{SC} is more or less constant at 15.55 mA/cm^2. However, the FF and η (efficiency) of $CH_3NH_3GeI_3$ based perovskite solar cell has been reduced from 83.19 % to 67.97 % and 18.16 % to 14.30 % respectively as illustrated in Fig. 3.12a and Fig. 3.12b.

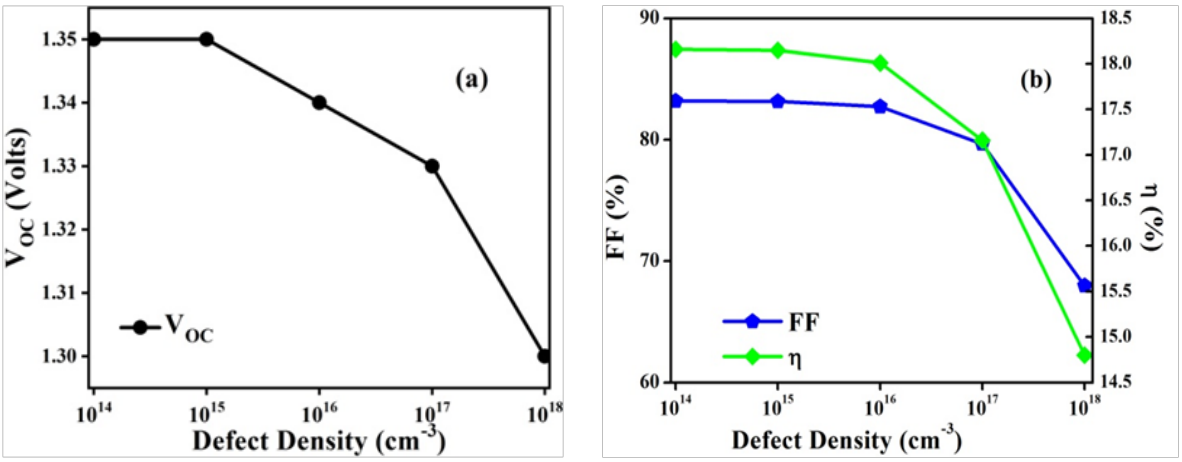

Fig. 3.12. Simulated result for varying $CH_3NH_3GeI_3$ defect density (a) V_{OC} and J_{SC} (b) FF and η

Likewise, the defect density of $CsSnGeI_3$ based perovskite layer is varied from 1×10^{14} cm^{-3} to 1×10^{19} cm^{-3}. The device photovoltaic performance of $CsSnGeI_3$ based perovskite layer is shown in Fig. 3.13a and Fig. 3.13b. As the defect density increases from 1×10^{14} cm^{-3} to 1×10^{19} cm^{-3} the V_{OC} reduces from 1.10 V to 0.79 V, J_{SC} decreases slightly from 25.76 mA/cm^2 to 25.15 mA/cm^2. Though FF reduces from 84.64 % to 67.12 % and a corresponding decrease of η is observed from 24.13 % to 13.42 % as illustrated in Fig. 3.13a and Fig. 3.13b.

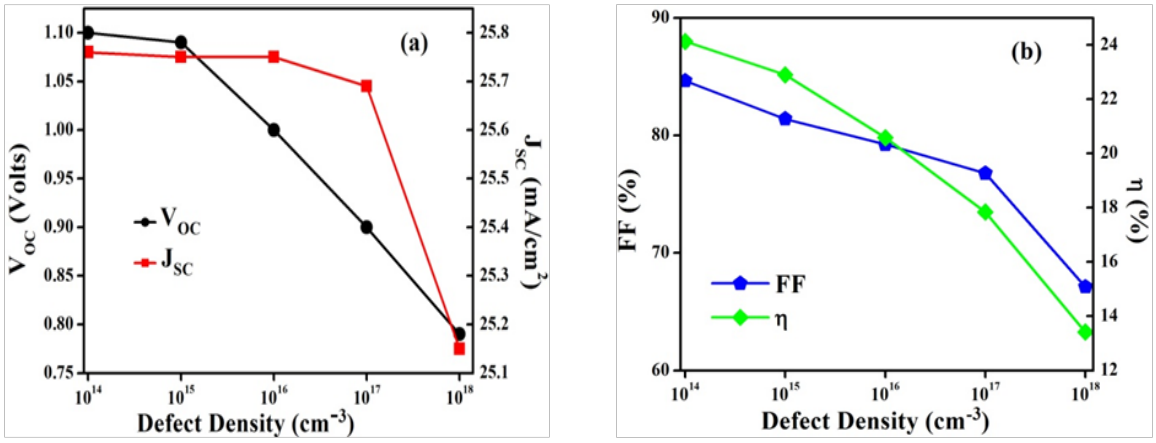

Fig. 3.13. Simulated result for varying $CsSnGeI_3$ defect density (a) V_{OC} and J_{SC} (b) FF and η

As the defect density of the absorber layer increases, it creates more recombination centres due to which more carriers are getting recombined within the absorber layer. Also, as the defect density of the absorber layer increases it will reduce the lifetime of carriers which degrades the overall device performance of solar cells as per the Eq. 3.6 and Eq. 3.7. Moreover, with the increase in defect density, recombination centres also increase which decreases the shunt resistance of the device which in turn reduce the open-circuit voltage (V_{OC}). Hence, it can be concluded from the above analysis that for better device performance of the solar cell, the defect density of the perovskite layers should be controlled to the order of ~1×10^{14} cm^{-3} as with the increase of defect density of the absorber layer, the photovoltaic performance has been reduced.

3.5 Effect of Metal Work Function on Lead-Free ($CH_3NH_3GeI_3$ and $CsSnGeI_3$) Based PSC

The metal electrode is deposited over the HTM to collect holes from the external circuit. To facilitate the proper collection of majority charge carriers *i.e.,* a hole through the back contact, the formation of an ohmic contact is an essential condition. To understand the effect of metal work function on the photovoltaic performance of all-perovskite multijunction solar cell different metal electrodes configuration has been studied. The metal work function has been increased from 4.65 eV to 5.65 eV (4.65 eV (Cu), 4.70 eV (Ag), 5.00 eV (Ni,C), 5.1 eV(Au), 5.30 eV(Pd), 5.65 eV(Pt)).

Fig. 3.14(a-b) and Fig. 3.16 (a-b) demonstrates the effect of metal work function on the performance of $CH_3NH_3GeI_3$ and $CsSnGeI_3$ based perovskite solar cells. As observed, when the work function increases till 5.0 eV, the V_{OC}, FF and η increase and get saturated when the metal work function is increased further. In the case of $CH_3NH_3GeI_3$ based PSC, when the metal work function increased from 4.65 eV to 5.65 eV the V_{OC} increased from 1.22 V to 1.34 V, FF increased from 78.28% to 82.74% and η enhances from 15.53 % to 18.02% as shown in Fig. 3.14(a-b). However, no significant change in J_{SC} is obtained. A similar trend is obtained in the $CsSnGeI_3$ based perovskite solar cell. With the increase of metal work function in case of $CsSnGeI_3$ based perovskite solar cell from 4.65eV to 5.65 eV, the V_{OC} increases from 0.89 V to 1 V, whereas FF and η elevates from 69.65% to 79.22% and 16.07% to 20.60 % respectively as shown in Fig. 3.16a and Fig. 3.16b. From the obtained results, it can be easily depicted that, as the work function of metal increases the efficiency enhances correspondingly which in turn improve the device performance.

It is observed from Fig. 3.15a and Fig. 3.17a, that a barrier exists between the back contact and HTM layer when the metal work function is 4.65 eV however as the metal work function increases till 5.0 eV the majority carrier barrier height reduces. When the work function of back contact is equal to the valence band maximum (VBM) of HTM or smaller than that of HTM, it will create a barrier for holes as shown in Fig. 3.15a and Fig. 3.17a.

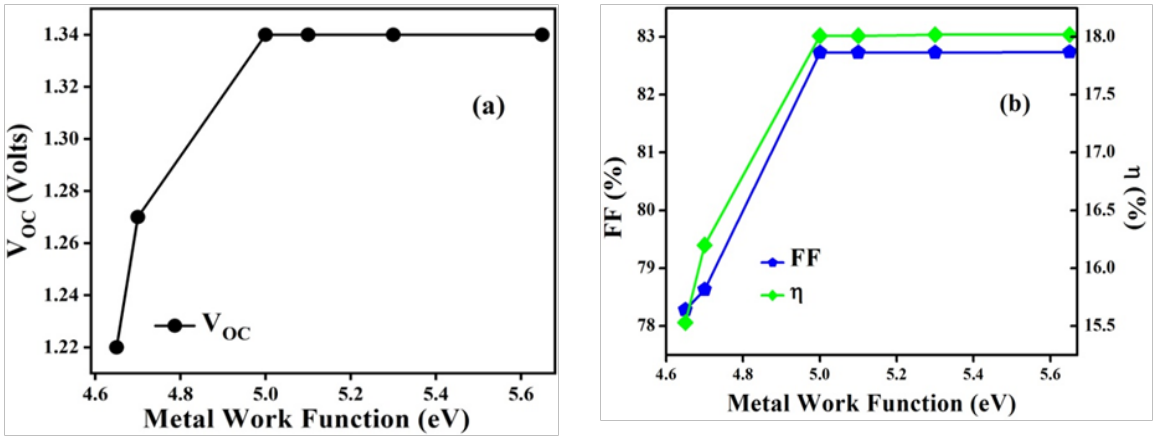

Fig. 3.14. Simulated results for metal work function for $CH_3NH_3GeI_3$ solar cell (a) V_{OC} and J_{SC} (b) FF and η

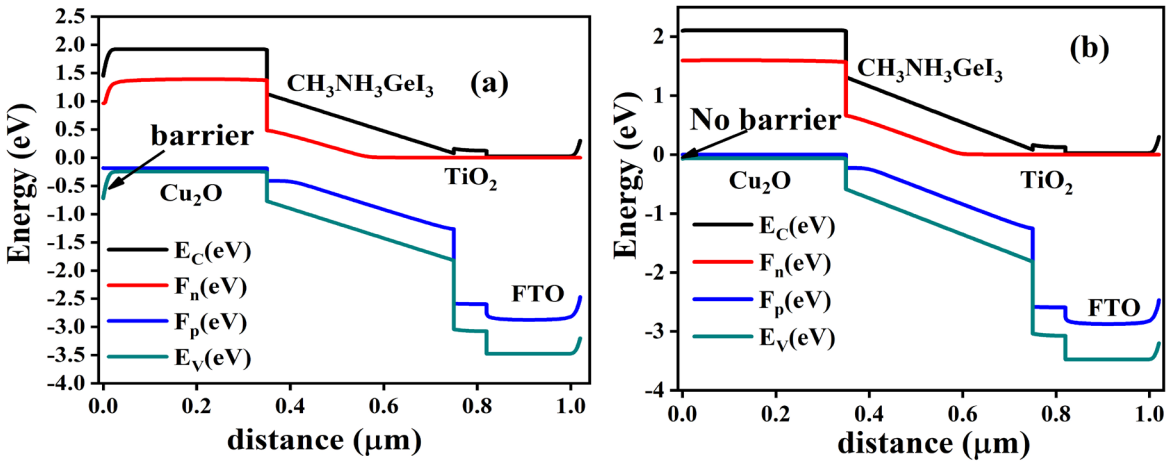

Fig. 3.15. Simulated energy band diagram for metal work function for $CH_3NH_3GeI_3$ solar cell (a) 4.65 eV (b) 5.00 eV

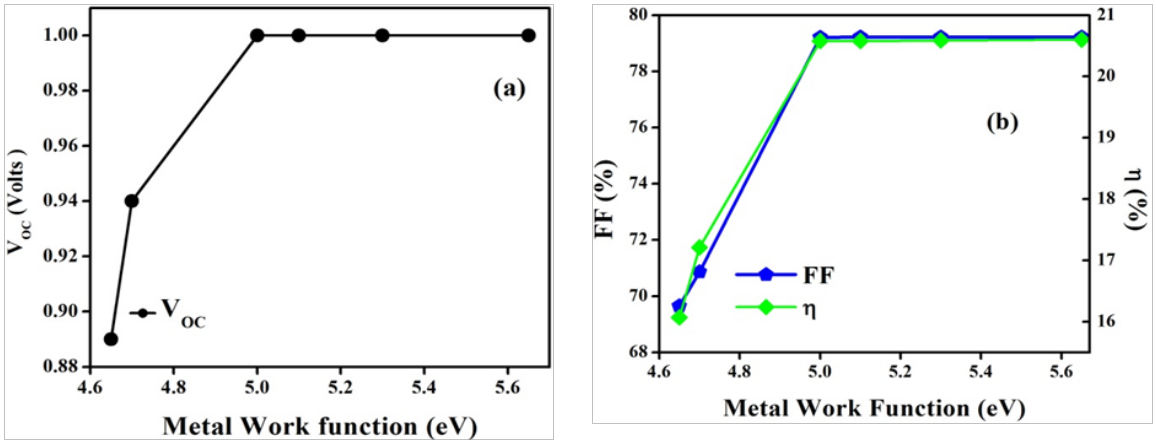

Fig. 3.16. Simulated results for metal work function for $CsSnGeI_3$ solar cell (a) V_{OC} and J_{SC} (b) FF and η

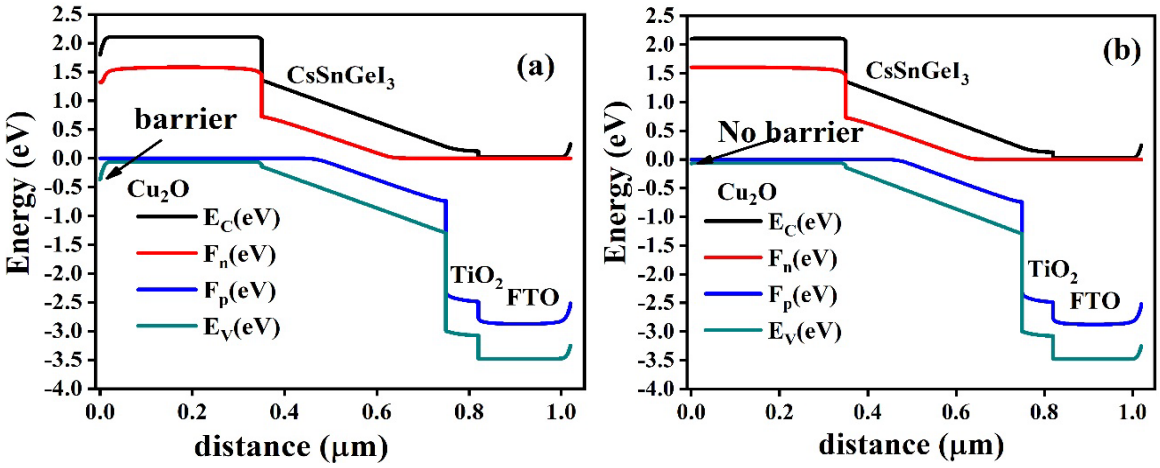

Fig. 3.17. Simulated energy band diagram for metal work function for $CsSnGeI_3$ solar cell (a) 4.65 eV (b) 5.00 eV

However, when the 5.0 eV, metal work function is used, it matches with the Fermi level of the HTM layer and the barrier will get depleted and hence the power conversion efficiency is saturated as shown in Fig. 3.15b and Fig. 3.17b. On further increasing the metal work function, the device performance gets saturated as it gets restricted by the number of charge carriers available for the collection. Therefore, V_{OC} and PCE increase to 5.0 eV and on further increasing the metal work function the device performance gets saturated.

From the obtained results, it can be concluded that, to achieve higher photovoltaic performance, the metal work function should not be less than 5.0 eV [128] as far as Cu_2O is considered as an HTM. Due to the 5.0 eV work function of graphene, it is also considered as a prominent choice for the application of back contact electrode for the application of $CH_3NH_3GeI_3$ solar cell and $CsSnGeI_3$ based perovskite solar cell [128].

3.6 Effect of Temperature on Lead-Free ($CH_3NH_3GeI_3$ and $CsSnGeI_3$) Based PSC

Due to the continuous touch with the sunlight, it will increase the cell temperature (>400 K) even higher than the room temperature (300 K). Hence, there is a need to understand the device performance parameters with varying the temperature. The device operating

temperature is varied from 250 K to 550 K under constant illumination. The photovoltaic performance with respect to the temperature for $CH_3NH_3GeI_3$ and $CsSnGeI_3$ based perovskite solar cells has been shown in Fig. 3.18(a-b) and Fig. 3.19(a-b).

It can be observed that as the temperature increases from 250 K to 550 K on $CH_3NH_3GeI_3$ based perovskite layer the V_{OC} has been reduced from 1.36 V to 1.22 V, FF reduces from 83.34% to 75.69% and efficiency has been decreased from 18.33% to 15.00 %. However, J_{SC} has been observed as more or less constant at 15.55 mA/cm^2. Moreover, as the temperature changes for $CsSnGeI_3$ based perovskite from 250 K to 550 K the V_{OC} reduces from 1.06 V to 0.49 V, FF drops from 80.71% to 59.24% and η decreases from 22.15% to 7.53% and a very slight increase in J_{SC} is obtained *i.e.,* 25.74 mA/cm^2 to 25.77mA/cm^2 as shown in Fig. 3.19a and Fig. 3.19b. The band gap was reduced at a higher temperature, due to which more recombination of electrons and holes will occur, resulting in the reduction of V_{OC}. Also, the increase in temperature is directly related to the increase in defects and thus reduces V_{OC}. Furthermore, the lowering of FF and η with the increase of temperature can be explained due to the decrement of shunt resistance.

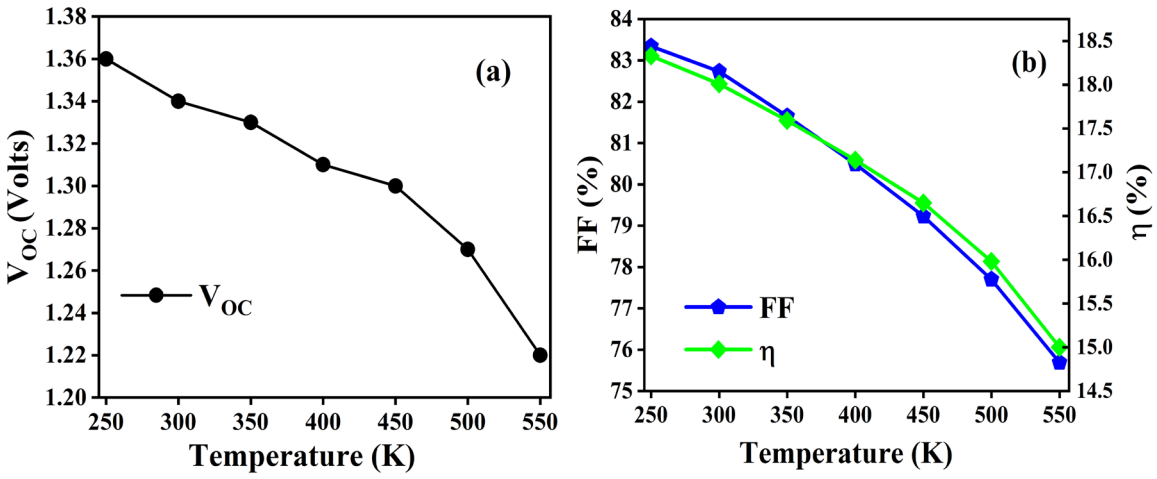

Fig. 3.18. Simulated results for the effect of temperature for $CH_3NH_3GeI_3$ solar cells (a) V_{OC} and J_{SC} (b) FF and η

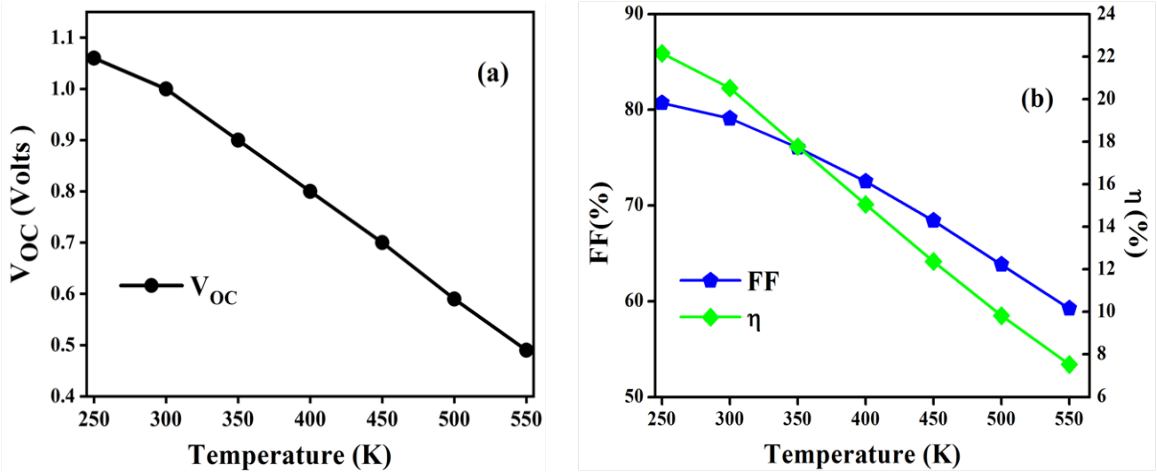

Fig. 3.19. Simulated results for the effect of temperature for $CsSnGeI_3$ solar cells (a) V_{OC} and J_{SC} (b) FF and η

It can be obtained from the simulation analysis that the proposed lead-free perovskite materials show a promising efficiency for PSC development. It can be illustrated from the above analysis that the proposed optimized wide band gap and low band gap perovskite solar cell possess ($CH_3NH_3GeI_3$) V_{OC}= 1.34 V, J_{SC}=15.55 mA/cm^2, FF=83.34% and η= 18.33% whereas the $CsSnGeI_3$ based perovskite shows the device photovoltaic performance V_{OC}= 1.00 V, J_{SC}=24.79 mA/cm^2, FF=80.71 % and η= 22.15% at 300 K temperature.

3.7 Conclusion

This chapter comprises of the simulations of Pb-free PSC ($CH_3NH_3GeI_3$, $CsSnGeI_3$) using SCAPS 1D simulation software. It is observed that, as compared to the $CH_3NH_3GeI_3$ based structure, $CsSnGeI_3$ based structure shows better photovoltaic performance parameters. Further, to achieve better photovoltaic performance, the device V_{OC} is correlated by V_{bi}. It is obtained that Cu_2O as an HTL shows higher V_{OC} in both $CH_3NH_3GeI_3$ and $CsSnGeI_3$ based perovskite structures. In addition, it has been revealed that the photovoltaic performance of the device mainly depends on the defect density, metal work function as well as temperature. It can be illustrated from the above analysis that the proposed optimized wide band gap and low band gap perovskite solar cell possess

($CH_3NH_3GeI_3$) V_{OC}= 1.34 V, J_{SC}=15.55 mA/cm^2, FF=83.34% and η= 18.33% whereas the $CsSnGeI_3$ based perovskite shows the device photovoltaic performance V_{OC}= 1.00 V, J_{SC}=24.79 mA/cm^2, FF=80.71 % and η= 22.15%. It has been obtained that $CsSnGeI_3$ based perovskite solar cell depicts much better performance as compare to the $CH_3NH_3GeI_3$ perovskite solar cell, also $CsSnGeI_3$ based perovskite solar cell shows more significant changes by varying defect density as compare to the $CH_3NH_3GeI_3$ perovskite solar cell. It has been found that at 1×10^{14} cm^{-3} defect density the device efficiency increases up to 4% in the case of $CsSnGeI_3$ based perovskite solar cell, however, no significant changes are obtained for $CH_3NH_3GeI_3$ based perovskite solar cell. Furthermore, it has been elucidated that for better device performance the back contact work function for both $CH_3NH_3GeI_3$ and $CsSnGeI_3$ based perovskite layers should be greater than 5.0 eV. As the device temperature increases the overall PV performance of the PSC starts degrading. The proposed optimized wide band gap and low band gap perovskite solar cell possess ($CH_3NH_3GeI_3$) V_{OC}= 1.34 V, J_{SC}=15.55 mA/cm^2, FF=83.34% and η= 18.33% whereas the $CsSnGeI_3$ based perovskite shows the device photovoltaic performance V_{OC}= 1.00 Volt, J_{SC}=24.79 mA/cm^2, FF=80.71 % and η= 22.15%.

CHAPTER 4

EFFECT OF CHARGE TRANSPORT LAYERS ON THE PERFORMANCE OF LEAD–FREE DOUBLE-PEROVSKITE SOLAR CELL

4.1 Introduction

Double halide perovskite such as $Cs_2AgBiBr_6$ proves to be a viable alternative for the non-toxic perovskite solar cells due to its excellent physical and optoelectronic properties but its PCE is still limited up to ~5% due to its low visible light absorption [71][72]. Moreover, $Cs_2AgBiBr_6$ shows a bandgap up to 2.2 eV, which is unsuitable for absorber layers of PSC. Several strategies are explored to reduce its bandgap such as the addition of metal cation *e.g.* (Tl^{3+}, Sb^{3+}). It is obtained from literature that by substituting 25% of Sb^{3+} (antimony) along with the Bi^{3+} (Bismuth) on $Cs_2AgBiBr_6$ to form $Cs_2AgBi_{0.75}Sb_{0.25}Br_6$ there is an increase in a red shift at the absorption spectra due to which the E_g reduces up to ~1.6 eV. In addition, Hutter *et al.* prepared the mixed Sb-Bi ($Cs_2AgBi_{1-x}Sb_xBr_6$) based perovskite film using wet chemical processing [135]. Despite the limited efficiency, it raises the potential to develop a more efficient mixed halide double-perovskite solar cell. Madan *et al.* reported a lead–free all-perovskite tandem structure in which $Cs_2AgBi_{1-x}Sb_xBr_6$ as a wide bandgap perovskite layer has been introduced[40]. Despite having a tandem configuration based on the $Cs_2AgBi_{1-x}Sb_xBr_6$ structure, it has been elucidated from the literature that comparatively limited analogous study has been reported based on lead-free double–perovskite (Pb-free DPSC) ($Cs_2AgBi_{1-x}Sb_xBr_6$) solar cells. The only study based on $Cs_2AgBi_{0.75}Sb_{0.25}Br_6$ is done by Pantaler *et al.* and the study depicts the device efficiency limited up to ~ 1%[73]. However, the effect of ETLs and HTLs have not been studied which could impact the device efficiency significantly. For high device performance, ETL should have high electron mobility, a wide bandgap and should be transparent so that it can permit a maximum portion of the light to get transmitted through it and absorbed in the perovskite absorber layer. Though, various hole and electron transport layers have been explored within a decade. Nevertheless, due to these stringent requirements high-performance charge transport layers are still limited. However, due to the complexity and limitation of the deposition

methods the simulation routes are considered as a promising approach for understanding the effects of the different hole and electron transport layer on the lead-free double-perovskite solar cell performance. This chapter reports the studies on the numerical simulation of the standalone lead-free bismuth-antimony based mixed double-perovskite solar cell and the effect of different charge transport layers and their thickness. Additionally, the present investigation correlates the V_{OC} with the V_{bi} which clarifies the selection of the best ETLs and HTLs to enhance the efficiency of the device. This chapter includes studies to suggest the possible way of enhancing the device efficiency of Pb-free DPSC ($Cs_2AgBi_{0.75}Sb_{0.25}Br_6$) solar cell structure.

4.2 Device Structure and Simulation Parameters

The device structure of the Pb-free DPSC has been shown in Fig. 4.1. It consists of the $Cs_2AgBi_{0.75}Sb_{0.25}Br_6$ layer as a perovskite absorber layer whereas spiro-OMeTAD as an HTL and ZnO as an ETL.

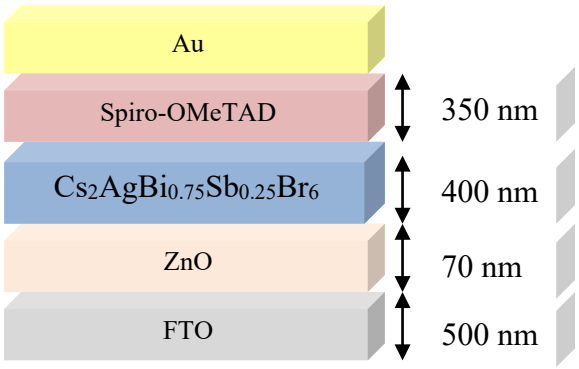

Fig. 4.1. Device structure for Pb-free DPSC

The parameters taken for the double-perovskite absorber layer, different HTLs and ETLs are shown in Table 4.1, Table 4.2 and Table 4.3.

Table 4.1 Numerical parameters considered for double–perovskite absorber layer, electron and hole transport layer and transparent conductive oxide layer

Parameters	SpiroOMeTAD	$Cs_2AgBi_{0.75}Sb_{0.25}Br_6$	ZnO	FTO
Thickness (μm)	0.350	0.400	0.070	0.500

Eg (eV)	3.00	1.8	3.3	3.5
Electron affinity (eV)	2.45	3.58	4.00	4.00
Dielectric permittivity	3.00	6.5	9.00	9.00
N_c (cm^{-3})	2.2×10^{18}	2.2×10^{18}	3.7×10^{18}	2.2×10^{18}
N_v (cm^{-3})	1.8×10^{19}	1.8×10^{19}	1.8×10^{19}	1.8×10^{19}
Electron thermal velocity (cm/s)	1×10^{7}	1×10^{7}	1×10^{7}	1×10^{7}
Hole thermal velocity (cm/s)	1×10^{7}	1×10^{7}	1×10^{7}	1×10^{7}
Electron mobility (cm^2/Vs)	2×10^{-4}	2	100	20
Hole mobility (cm^2/Vs)	2×10^{-4}	2	25	10
N_D (cm^{-3})	0	10^{13}	5×10^{17}	10^{18}
N_A (cm^{-3})	2×10^{18}	10^{17}	0	0
N_t (cm^{-3})	10^{15}	10^{14}	10^{15}	10^{15}
References	[53]	[40]	[127]	[122]

Table 4.2 Numerical parameters considered for hole transport layers (HTLs)

Parameters	Cu_2O	CuI	$CuSbS_2$	NiO	PEDOT:PSS
Thickness (μm)	0.350	0.350	0.350	0.350	0.350
Bandgap (eV)	2.17	2.98	1.58	3.80	2.2
Electron affinity (eV)	3.2	2.1	4.20	1.46	2.9
Dielectric permittivity	7.1	6.5	14.60	10.70	3
N_c (cm^{-3})	2.02×10^{17}	2.8×10^{19}	2×10^{18}	2.8×10^{19}	2.2×10^{15}
N_v (cm^{-3})	1.10×10^{19}	1×10^{19}	1×10^{19}	1×10^{19}	2.2×10^{17}
Electron thermal velocity (cm/s)	1×10^{7}	1×10^{7}	1×10^{7}	1×10^{7}	1×10^{7}

Hole thermal velocity (cm/s)	1×10^{7}	1×10^{7}	1×10^{7}	1×10^{7}	1×10^{7}
Electron mobility (cm^2/Vs)	200	1.7×10^{-4}	49	12	2×10^{-3}
Hole mobility (cm^2/Vs)	80	2×10^{-4}	49	2.8	2×10^{-3}
N_A (cm^{-3})	9×10^{21}	1×10^{18}	1.38×10^{18}	1×10^{18}	1×10^{17}
References	[121]	[122]	[129]	[125]	[122]

Table 4.3 Numerical parameters considered for electron transport layers (ETLs)

Parameters	STO	WS_2	IGZO	ZnSe	ZnOS
Thickness (μm)	0.070	0.070	0.070	0.070	0.070
E_g (eV)	3.2	1.8	3.05	2.81	2.83
Electron affinity (eV)	4.00	3.95	4.16	4.09	3.6
Dielectric permittivity	8.70	13.60	10.00	8.6	9
Conduction Band Density of States (N_c)(cm^{-3})	1.7×10^{19}	1×10^{18}	5×10^{18}	2.2×10^{18}	2.2×10^{18}
Valence band density of states (N_v) (cm^{-3})	2×10^{20}	1×10^{18}	5×10^{18}	1.8×10^{18}	1.8×10^{18}
Electron thermal velocity (cm/s)	1×10^{7}	1×10^{7}	1×10^{7}	1×10^{7}	1×10^{7}
Hole thermal velocity (cm/s)	1×10^{7}	1×10^{7}	1×10^{7}	1×10^{7}	1×10^{7}
Electron mobility (cm^2/Vs)	5.3×10^{3}	50	15	4×10^{2}	100
Hole mobility (cm^2/Vs)	6.6×10^{2}	50	0.1	1.1×10^{2}	25
N_D (cm^{-3})	2×10^{16}	1×10^{18}	1×10^{18}	1×10^{18}	2×10^{18}

References	[130]	[131]	[124]	[132]	[133]

The Pb-free DPSC ($Cs_2AgBi_{0.75}Sb_{0.25}Br_6$) solar cell is designed as shown in Fig. 4.1. The device structure for Pb-free DPSC and the proposed solar cell is simulated using SCAPS 1D. Fig. 4.2(a) and Fig. 4.2(b) present the current-voltage (J-V) characteristic and quantum efficiency (QE) characteristics. The Pb-free DPSC based on $Cs_2AgBi_{0.75}Sb_{0.25}Br_6$ as a perovskite absorber layer exhibits power conversion efficiency η= 11.35%, V_{OC}= 0.94 Volts, J_{SC}=15.95 mA/cm^2, and FF= 72.65%.

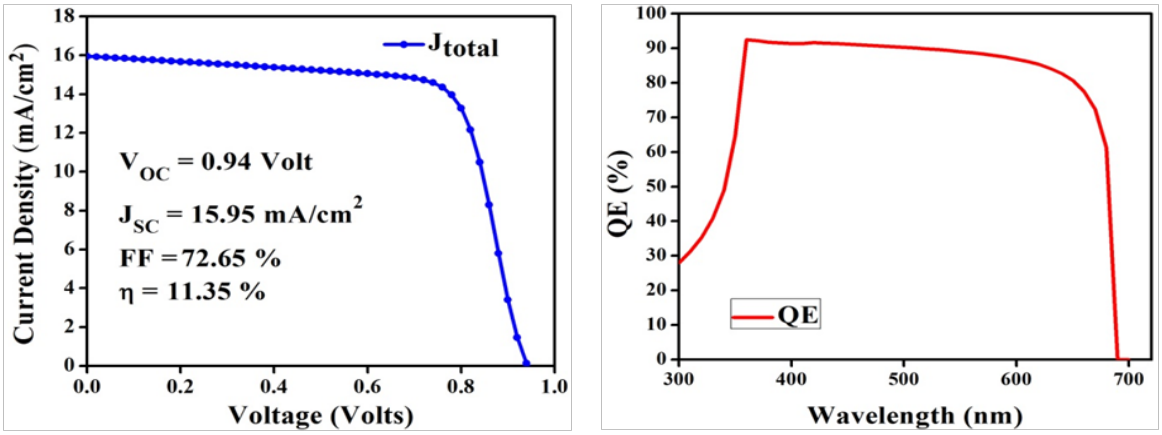

Fig. 4.2. Characteristics of Pb-free DPSC structure (a) J-V curve (b) QE curve

4.3 Hole Transport Layer Effects on the PV Performance of Pb-Free DPSC

To examine the impact of various HTLs on the performance of DPSC various HTLs are analyzed. Depending upon the conduction band and valence band energy levels different HTLs are arranged as shown in Fig. 4.3(a-f).

To efficiently optimize the hole transport layers, the V_{bi} which is generated across the perovskite layer is correlated with the open-circuit voltage (V_{OC}). The band diagram obtained from simulation for different HTLs is shown in Fig. 4.4(a-f). The J-V curve and QE curve as obtained is shown in Fig. 4.5a and Fig. 4.5b. The resulted parameters for different hole transport layers are listed in Table 4.5. It is observed that there is a relationship between V_{bi} and V_{OC} as the higher V_{bi} is attributed to higher V_{OC} as given in Table 4.5. It is obtained from Table 4.5 that the lowest open-circuit voltage (V_{OC}) is

obtained by $CuSbS_2$ and the highest open-circuit voltage (V_{OC}) is obtained by Cu_2O which significantly increase its η from 8.74 % to 12.67%. In the case of $CuSbS_2$ as an HTL, even the E_{C_ETL}-E_{V_HTL} = 1.78 eV which is quite high, but still shows lower V_{bi} of 0.78 eV as compare to the other HTLs and thus the photovoltaic performance degrades significantly. The lower photovoltaic performance with $CuSbS_2$ is mainly because of the band misalignment between the perovskite/HTL interface as shown in Fig. 4.3d. In addition, in the case of $CuSbS_2$, a barrier cliff is created between the perovskite and HTL interface, which hinders carrier transport between perovskite and HTL as shown in Fig. 4.4d and thus reduce overall photovoltaic performance. However, the E_{V_HTL} level of Cu_2O is 5.37 eV which is almost similar to the E_{V_PVK} level of the perovskite layer and shows the best efficiency. However, it is obtained from Table 4.5 that NiO, CuI and PEDOT:PSS shows similar V_{OC}, but the highest value of PCE is obtained by Cu_2O. This is mainly attributed because of higher V_{bi} value obtained by the Cu_2O which resulted in its higher V_{OC} and PCE.

From Table 4.6, it is seen that when E_{C_ETL}-E_{V_HTL} < Φ_{BC}-E_{C_ETL}, V_{bi} is mainly influenced by E_{C_ETL}-$E_{V\_HTL.}$ In addition, when Φ_{BC}-E_{C_ETL} < E_{C_ETL}-E_{V_HTL}, the V_{bi} is mainly influenced by Φ_{BC}-$E_{C\_ETL.}$ In the HTL simulation analysis, as V_{bi} is closed to Φ_{BC}-E_{C_ETL}, hence V_{bi} is mainly affected by Φ_{BC}-E_{C_ETL} therefore the obtained V_{OC} is corresponding to Φ_{BC}-E_{C_ETL}. Furthermore, it is also obtained from Table 4.5 that even E_{C_ETL}-E_{V_HTL} is varied from 1.10 V to 1.78 V still V_{bi} is limited to 0.99 eV as V_{bi} is mainly influenced by Φ_{BC}-E_{C_ETL}.Moreover, it is also recommended that to obtain higher V_{OC} and PCE, the E_{V_HTL} and Φ_{BC} should not be deeper than the E_{V_PVK} to prevent V_{bi} loss.

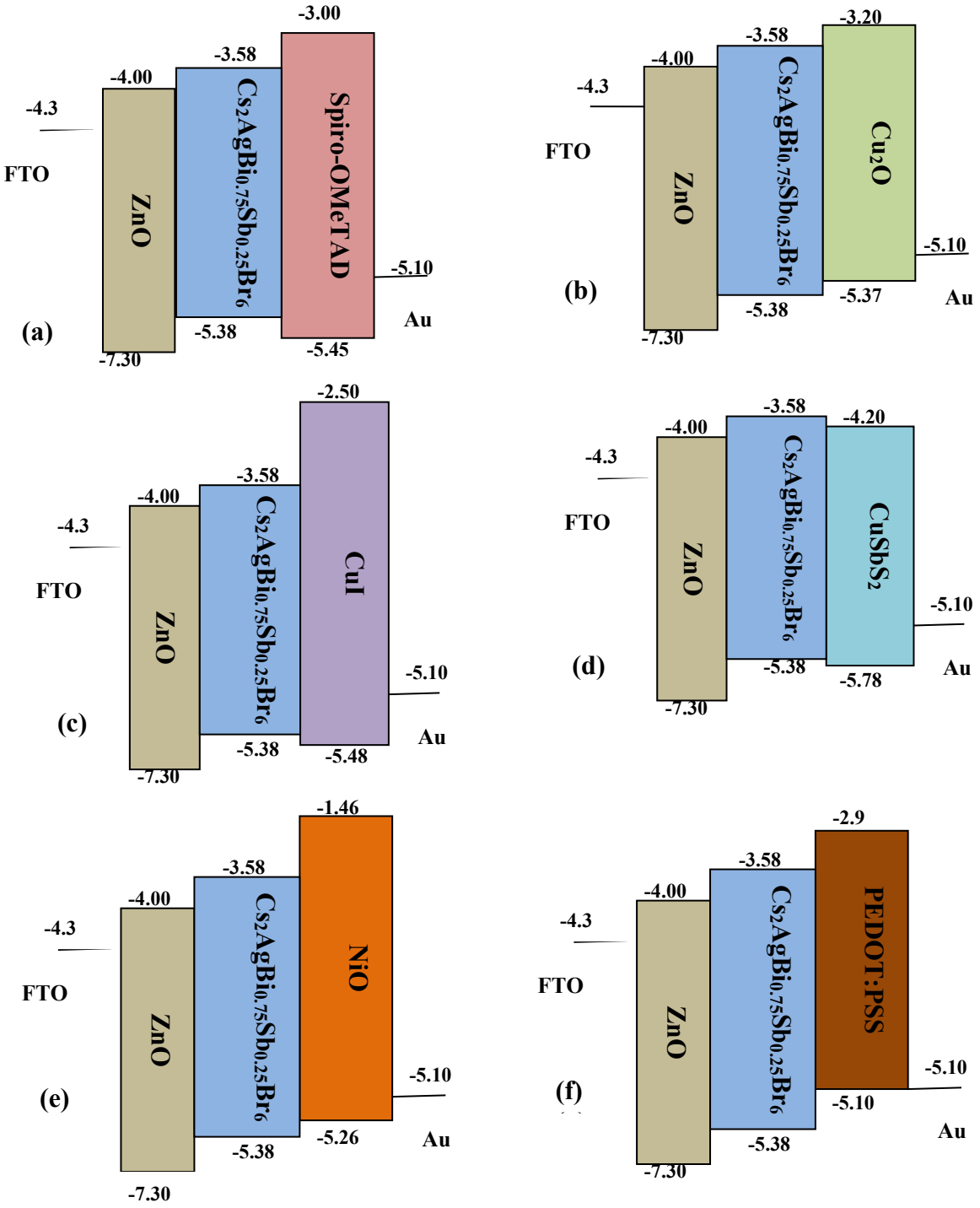

Fig. 4.3. Energy band diagrams for different HTL for Pb-free DPSC (a) spiro-OMeTAD (b) Cu_2O (c) CuI (d) $CuSbS_2$ (e) NiO (f) PEDOT:PSS

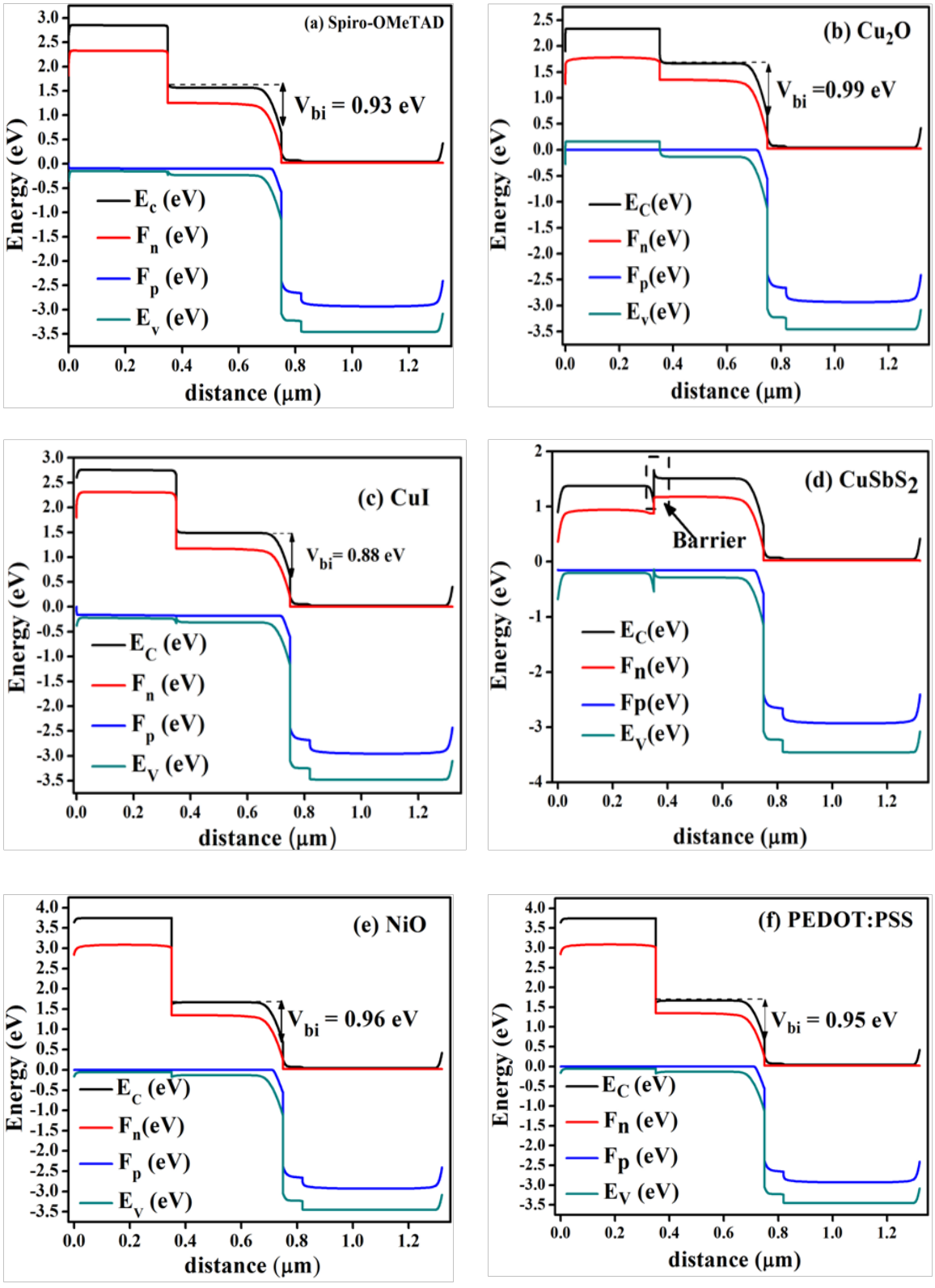

Fig. 4.4. Energy band diagram of various HTL on the photovoltaic performance of Pb-free DPSC (a) spiro-OMeTAD (b) Cu_2O (c) CuI (d) $CuSbS_2$ (e) NiO (f) PEDOT:PSS

Table 4.4 Effect of different HTL on the photovoltaic performance of the lead-free double-perovskite solar cell

Hole Transport Layers (HTL)	E_{C_ETL}-E_{V_HTL} (eV)	Φ_{BC}-E_{C_ETL} (eV)	qV_{bi} (eV)	V_{OC} (Volts)	J_{SC} (mA/cm^2)	FF (%)	η (%)
Spiro-OMeTAD	1.45	1.10	0.93	0.94	15.95	72.65	11.35
Cu_2O	**1.37**	**1.10**	**0.99**	**0.96**	**15.91**	**79.18**	**12.67**
CuI	1.48	1.10	0.88	0.88	15.92	69.83	10.26
$CuSbS_2$	1.78	1.10	0.78	0.84	13.67	72.86	8.74
NiO	1.26	1.10	0.96	0.96	15.85	78.90	12.58
PEDOT:PSS	1.10	1.10	0.96	0.96	14.84	77.16	11.48

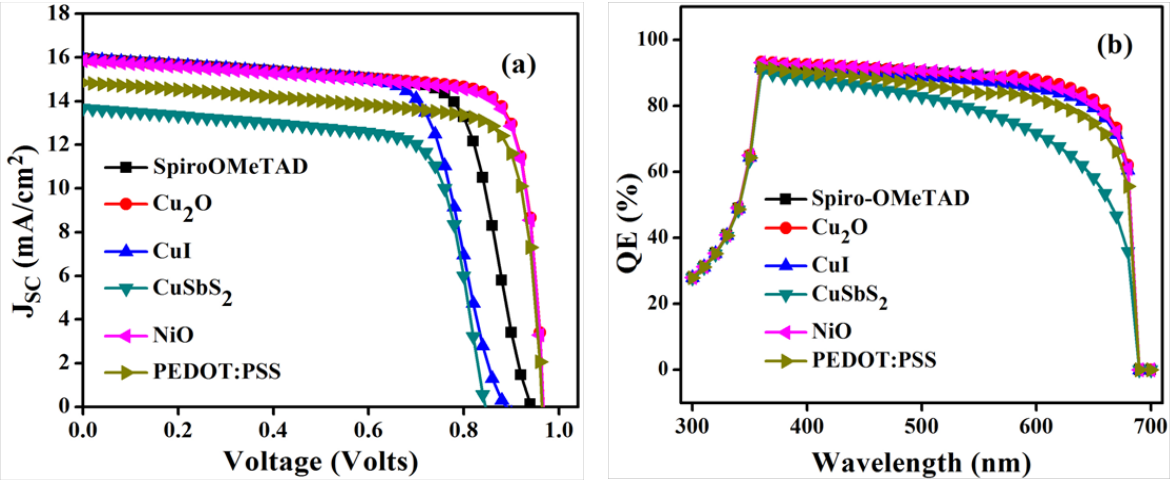

Fig. 4.5. (a) J-V curve and (b) QE curves for different HTLs on lead-free double-perovskite solar cells

Fig. 4.5a shows the resulted J-V curve of the hole transport layers of Pb-free DPSC. It is evident from the J-V curve that Cu_2O shows the higher V_{OC} as well as J_{SC}. On the contrary, $CuSbS_2$ shows the lowest J_{SC} and V_{OC}. The highest V_{OC} and J_{SC} of Cu_2O is attributed to the better band alignment with the corresponding layers as well as it shows higher V_{bi} *i.e.,* up to 0.99 eV. It can be observed from Fig. 4.5b that a quite low QE is observed for $CuSbS_2$ and PEDOT:PSS HTL layers. The prime reason for $CuSbS_2$ to show

low QE is because of the band misalignment between perovskite/HTL interface which limits carrier collection from the absorber layer to the electrode. In addition, the lower QE of $CuSbS_2$ is due to its lower bandgap (E_g) as most of the carriers are absorbed in the hole transport layer instead of the absorber layer. Due to this the absorption of photons, as well as carrier generation, decreases in the absorber layer resulted in the lower QE in the case of $CuSbS_2$. However, PEDOT:PSS shows low photovoltaic performance due to the low charge carrier mobility which in turn reduce the carrier collection to the electrodes. On the other hand, no significant changes are obtained by changing HTL on the quantum efficiency curve. As it is obtained from Fig. 4.5a and Fig. 4.5b that Cu_2O shows higher photovoltaic performance hence Cu_2O is preferred as a hole transport layer.

4.4 Electron Transport Layer Effects on the PV Performance of Pb-Free DPSC

In this section, Cu_2O is taken as the HTL and ETL has been varied. The ETLs are organized based on their conduction and valence band energy level as shown in Fig. 4.6(a-f). The band diagrams for different ETLs layers are shown in Fig. 4.7(a-f).

The resulted photovoltaic performance is given in Table 4.5. In case of STO, the value of E_{C_ETL}-E_{V_HTL} =1.37 eV which exhibits lesser built-in potential V_{bi} =0.43 eV. The lower V_{bi} corresponds to the lower V_{OC} *i.e.,* 0.85 V. On the other hand, the highest V_{OC} is obtained for ZnOS which helps to increase its PCE from 10.50 % to 18.18%. The highest V_{OC} is achieved in the case of ZnOS is attributed to its higher V_{bi} *i.e.,* 1.62 eV**.** In the case of IGZO, the limited PCE is obtained due to the low charge carrier mobility of electrons and holes (μ_e = 15 cm^2/Vs and μ_h=0.1 cm^2/Vs) the photovoltaic performance gets limited as carriers are lost before reaching to the contacts. It can be suggested that E_{C_ETL}, Φ_{FC}, should not be much higher than E_{C_PVK} to avoid V_{bi} loss.

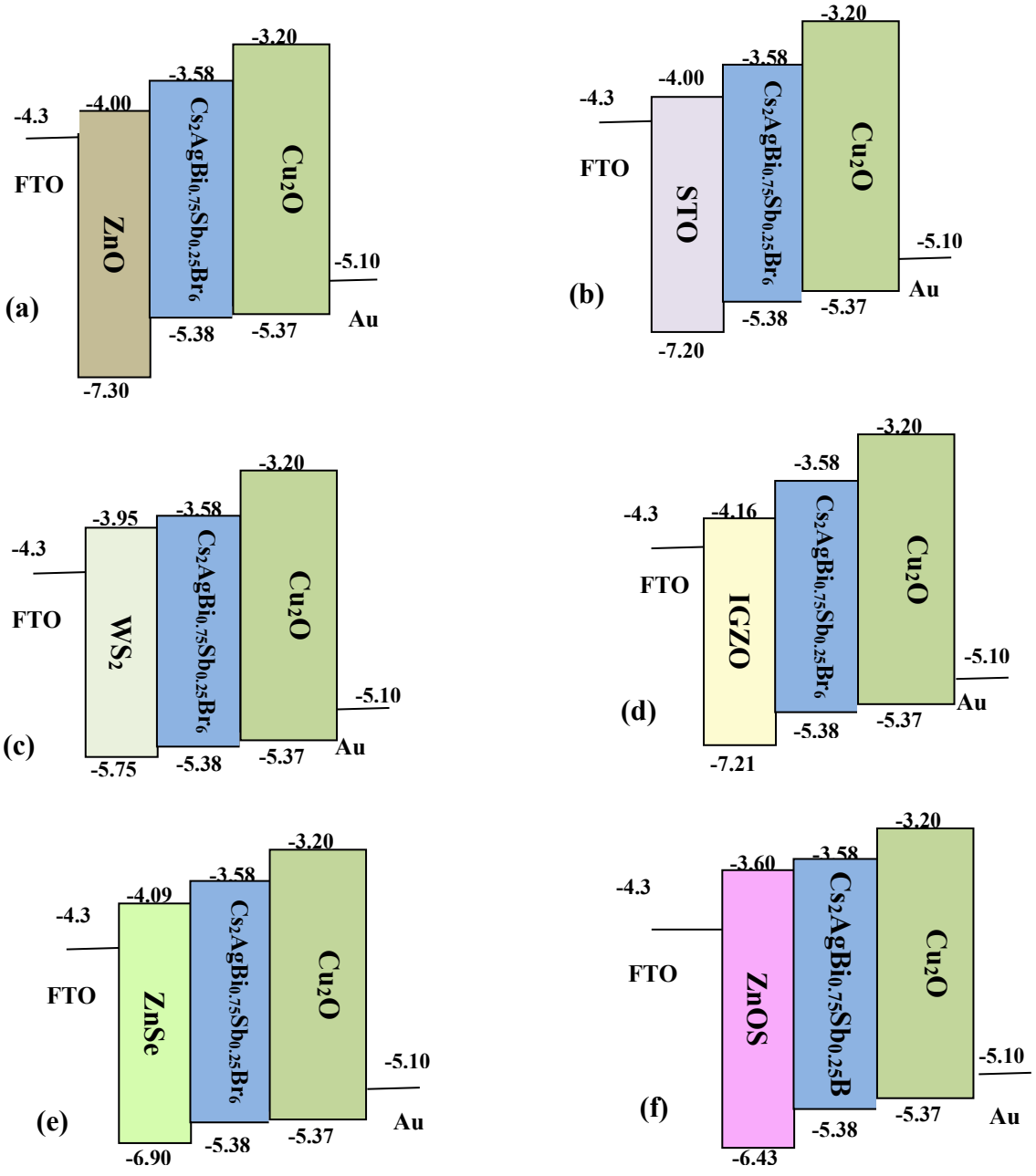

Fig. 4.6. Energy band level diagram for different ETL for Pb-free DPSC (a) ZnO (b) STO (c) WS_2 (d) IGZO (e) ZnSe (f) ZnOS

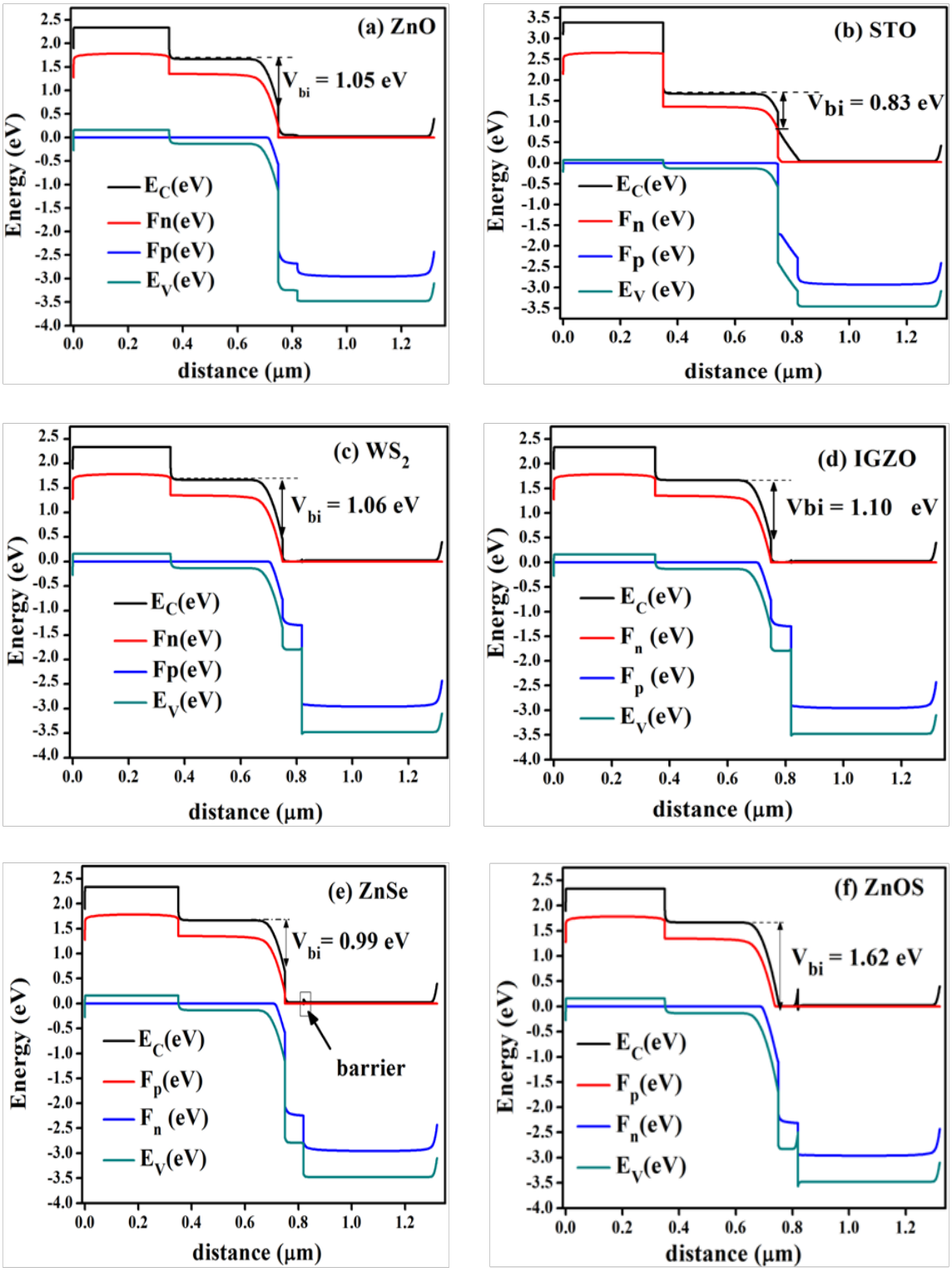

Fig. 4.7. Energy band diagram of ETL on the photovoltaic performance of Pb-free DPSC (a) ZnO (b) STO (c) WS_2 (d) IGZO (e) ZnSe (f) ZnOS

Fig. 4.8a and Fig. 4.8b shows the J-V curve and QE curve by varying different ETL on Pb-free DPSC. It is obtained from the current-voltage (J-V) and QE graph that STO shows comparatively less device power conversion efficiency as compared to other ETLs. In addition, ZnOS proves to be the best ETL among various ETL. However, different ETLs show variation in photovoltaic parameters as well as QE but comparatively less variations on QE curve is obtained for different ETLs. This is mainly attributed to the suitable electron and hole mobility as well as suitable band alignment which allows proper facilitation of electrons from perovskite to contacts via electron transport layer as depicted in Fig. 4.7(a-f).

Thus, from the resulted EBD as shown in Fig. 4.7f, and from Table 4.5 it is suggested that for better device photovoltaic performance ZnOS is proving to be the best alternative among all other ETLs and hence for making Pb-free double-perovskite solar cells, ZnOS as an ETL and Cu_2O as an HTL are chosen.

Table 4.5 Impact of various ETL on the device performance of Pb free DPSC

Electron Transport Layers (ETL)	E_{C_ETL}-E_{V_HTL} (eV)	Φ_{FC}-E_{V_HTL} (eV)	qV_{bi} (eV)	V_{OC} (Volts)	J_{SC} (mA/cm^2)	FF (%)	η (%)
ZnO	1.37	1.07	1.05	0.96	15.91	79.19	12.68
STO	1.37	1.07	0.83	0.85	15.62	75.68	10.50
WS_2	1.42	1.07	1.06	1.09	15.98	80.00	14.49
IGZO	1.21	1.07	1.10	0.83	15.88	79.15	10.91
ZnSe	1.28	1.07	0.99	0.92	15.92	79.46	12.14
ZnOS	**1.77**	**1.07**	**1.62**	**1.39**	**16.04**	**78.34**	**18.18**

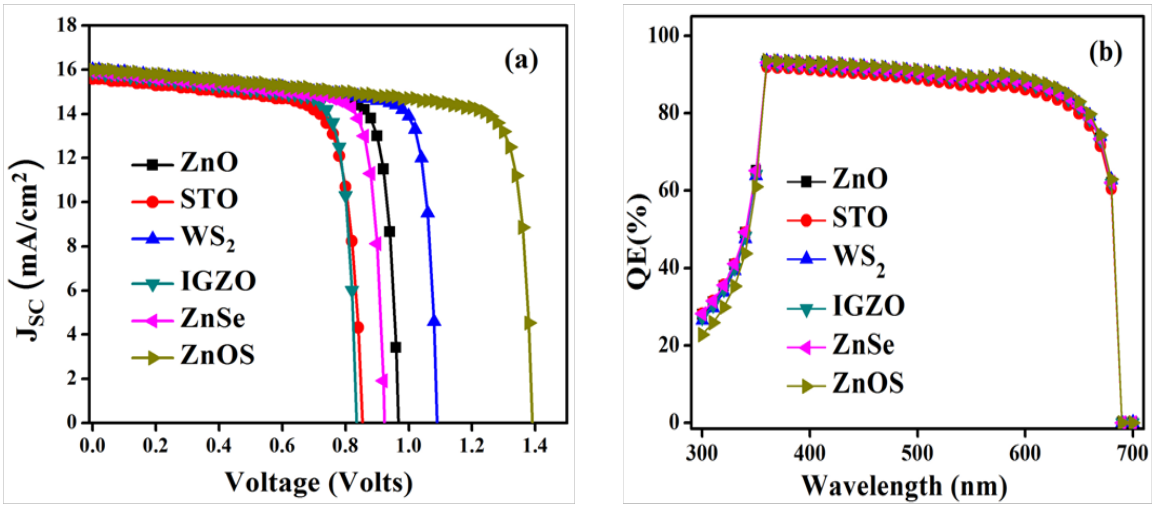

Fig. 4.8. (a) J-V and (b) Quantum Efficiency (QE) curve for different electron transport layers for Pb-free DPSC

4.5 Impact of Thickness of the Double–Perovskite Layer on the Device Performance

To understand the effect of varying thickness on the double-perovskite solar cell, the perovskite layer thickness is altered from 200 nm to 600 nm and the obtained PV performance is illustrated in Fig. 4.9 a and Fig. 4.9 b.

It is depicted from Fig. 4.9a and Fig. 4.9b that as the device thickness is varied from 200 nm to 600 nm a slight decrement of V_{OC} is observed, whereas J_{SC} increases from 14.88 mA/cm^2 to 16.04 mA/cm^2 up to 400 nm thickness after that it reduces and drops to 15.77 mA/cm^2. However, the FF drops slightly from 79.33% to 77.24%. As the thickness is increased to 400 nm the efficiency increases from 17.15% to 18.18% and after that, it reduces slightly to 17.55 % as shown in Fig. 4.9b.

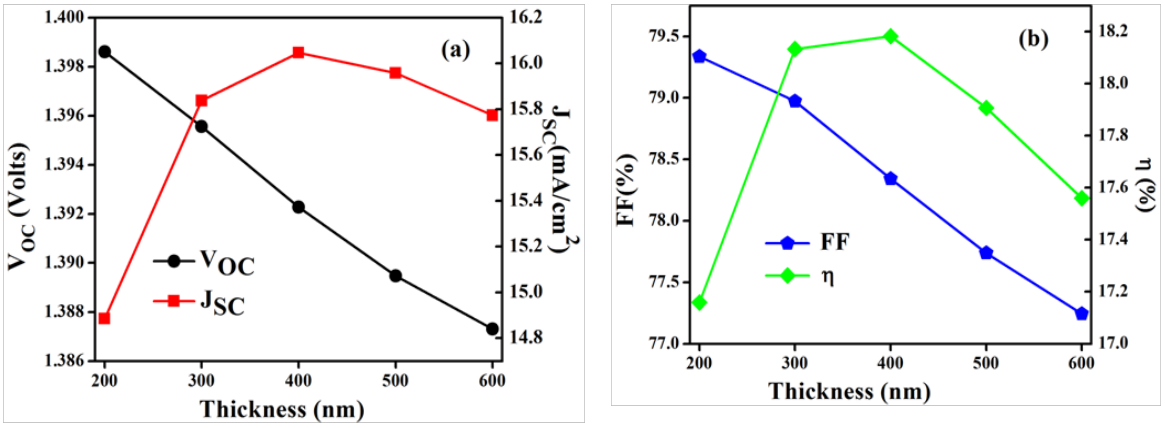

Fig. 4.9. Simulated results for the effect of thickness on Pb-free DPSC(a) V_{OC} and J_{SC} (b) FF and η

A slight decrement of V_{OC} with the increasing thickness is ascribed to the increment of J_0 which allows higher carrier recombination. The increment of J_0 will reduce the V_{OC} of the device with the increment of thickness as given in Eq. 4.1

$$V_{OC} = \frac{\eta' KT}{q} ln\left(\frac{J_{SC}}{J_0} + 1\right) \quad \textbf{Eq. 4.1}$$

In addition, an increase in J_{SC} with the increase in thickness is mainly because of thicker absorber layer which allows more generation of electron and hole pairs helping increase the J_{SC} of the double-perovskite solar cell. Further, increasing in thickness beyond 500 nm slightly reduces the J_{SC}. This slight decrement of J_{SC} may be due to the mismatch between the diffusion length of carriers and absorber layer thickness. Moreover, as the thickness increases up to 400 nm a slight increase in FF is observed afterwards it starts decreasing significantly. The decrease in FF is mainly due to an increase of series resistance with the thickness. It can be seen from the Fig. 4.9b that PCE first increase and then decrease with respect to the thickness. When the thickness of the perovskite layer increases, it will enhance the photon absorption and more carriers are generated which helps to increase the PCE. Also, with the increase in thickness, it will make a long transfer route for photo-generated carriers and hence carrier transportation is limited due to the enhanced recombination which in turn reduce the PCE of the device.

Fig. 4.11 shows the QE curve of double-perovskite solar cell with respect to varying thickness and Fig. 4.10 shows the optimized device structure of the solar cell. The QE of the double-perovskite solar cell enhanced remarkably till 400 nm to 500 nm after that it reduces. The increase in QE with respect to thickness corresponds to the increased absorption and carrier generation. However, the QE curve reduces considerably after 500 nm thickness, due to the increase of thickness beyond diffusion length of charge carriers *i.e.,* 0.510 µm, so the carriers are lost before reaching the back and front electrodes. As it is well evident that, the absorber layer thickness can be increased only up to the diffusion length of carriers. Thus, the optimized thickness for lead-free double–perovskite is considered 400 nm as slightly higher photovoltaic performance is attained as compared to 500 nm. At 400 nm the device photovoltaic parameters are given as open-circuit voltage (V_{OC}) = 1.39 V, short circuit current density (J_{SC}) = 16.03 mA/cm^2 Fill factor (FF) =78.37% and efficiency (η) = 18.18%. The optimized double-perovskite solar cell structure is given in Fig. 4.11. In addition, Fig. 4.12 represents the optimized J-V curve of the lead–free double-perovskite structure. The optimized parameter at each case is given in Table 4.6.

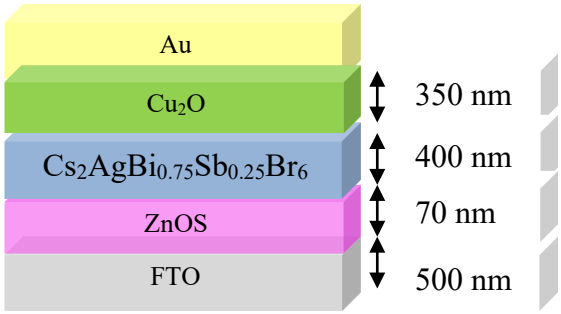

Fig. 4.10. Optimized lead–free double perovskite solar cell structure

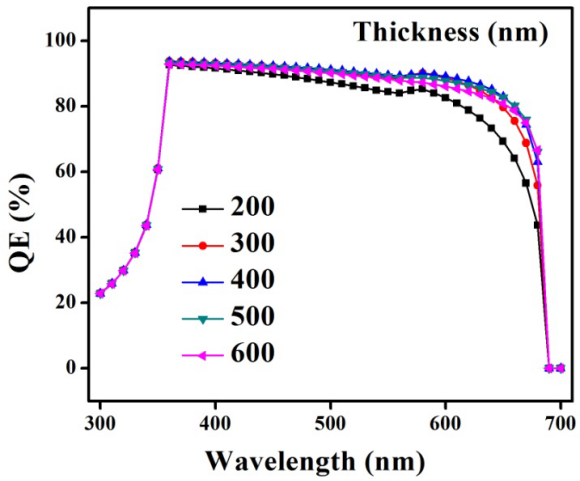

Fig. 4.11. The QE curve with varied thickness from 100 nm to 600 nm

Table 4.6 The final device photovoltaic performance obtained after each parameter optimization

Device Parameters	V_{OC} (Volts)	J_{SC} (mA/cm^2)	FF (%)	η (%)
Initial Solar cell Structure	0.94	15.95	72.65	11.35
After HTL optimization	0.96	16.00	79.19	12.74
After ETL and thickness optimization	1.39	16.03	78.37	18.18

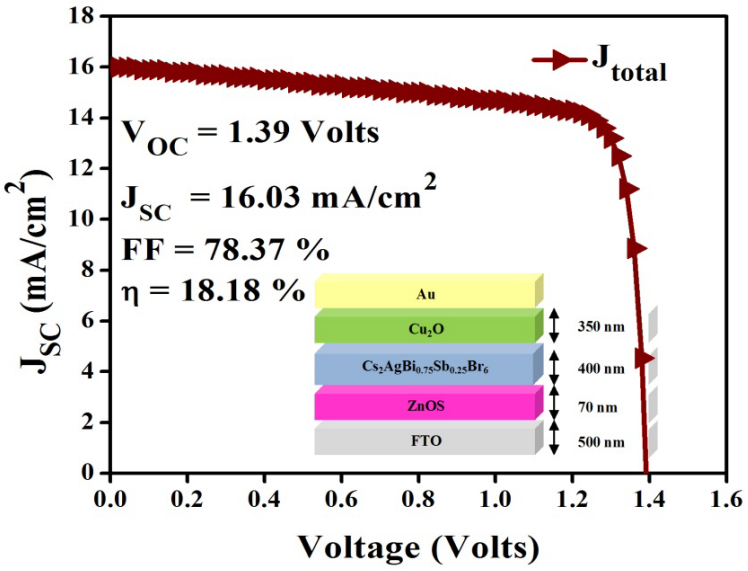

Fig. 4.12. Optimized J-V curve of Pb-free DPSC

4.6 Conclusion

This study brings forth the numerical simulation of Pb–free DPSC. Primarily, various potential HTL and ETL layers are studied. The optimization of ETLs and HTLs are performed by correlating the built-in voltage (V_{bi}) with the open-circuit voltage (V_{OC}). It is figured out from the obtained results, that the layer which shows higher V_{bi} leads to higher V_{OC}. It is revealed from the results that, Cu_2O shows promising results as a HTLs. On the other hand, ZnOS shows better device photovoltaic performance as an ETLs. It is found that to attain higher V_{OC} and PCE the proper selection of HTLs and ETLs is a crucial factor. For the proper selection of HTL, the E_{V_HTL} and ϕ_{BC} should not be much deeper than the E_{V_PVK} to avoid V_{bi} loss. On the other hand, for proper selection of ETL, E_{C_ETL}, Φ_{FC}, should not be much higher than E_{C_PVK} to avoid built-in potential loss. Furthermore, it is concluded that the optimized thickness of the lead-free double–perovskite absorber layer is 400 nm. After comprehensive optimization, the device photovoltaic performance elevates up to V_{OC} = 1.39V, J_{SC} = 16.04 mA/cm^2 , FF=78.34% and η= 18.18%. Due to the wide bandgap of the double-perovskite layer, this simulation study will help to design lead-free perovskite-based multijunction solar cells.

CHAPTER 5

NUMERICAL SIMULATION OF LEAD-FREE ALL-PEROVSKITE MULTIJUNCTION SOLAR CELL

There are numerous studied reported on multijunction solar cells, nevertheless there is a shortage of studies of Pb-free all-perovskite multijunction solar cells (APMJSC). Thus, this chapter aims to propose the Pb-free APMJSC using $CsSnGeI_3$ and $FAMASnGeI_3$ as a smaller band gap layer and $CH_3NH_3GeI_3$ as a wider band gap perovskite absorber layer. This chapter includes the study of the two Pb-free APMJSC configurations ($CH_3NH_3GeI_3$-$CsSnGeI_3$) and ($CH_3NH_3GeI_3$-$FAMASnGeI_3$) based perovskite solar cells.

5.1 Device Structure

This study includes two different all-perovskite multijunction solar cells which are as follows:

A) $CH_3NH_3GeI_3$ and $CsSnGeI_3$based all-perovskite multijunction solar cell
B) $CH_3NH_3GeI_3$ and $FAMASnGeI_3$based multi-junction solar cells

The standalone structure of ($CH_3NH_3GeI_3$-$CsSnGeI_3$) based all-perovskite multi-junction perovskite solar cell is already explored in chapter 3. However, the configuration of ($CH_3NH_3GeI_3$- $CsSnGeI_3$) based multijunction solar cell is shown in Fig. 5.1. Table 5.1, depicts the numerical parameters considered for the simulation.

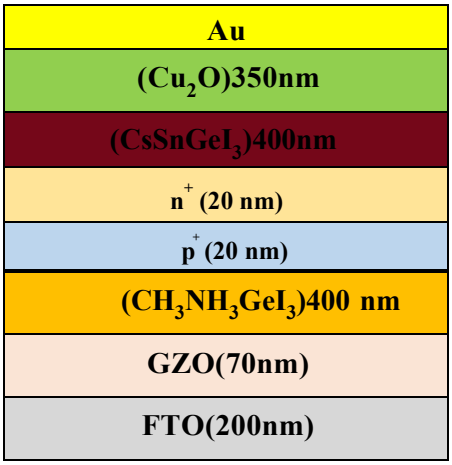

Fig. 5.1. Schematic of Pb-free all-perovskite multijunction solar cell

Table 5.1 Input simulation parameters of HTL, Pb-free perovskite layers, ETL, transparent conductive oxide

Parameters	Cu_2O	$CH_3NH_3GeI_3$	$CsSnGeI_3$	GZO	TCO (FTO)
Material Thickness (μm)	0.350	0.400	0.400	0.070	0.200
N_A (cm^{-3})	1×10^{18}	1×10^{19}	1×10^{14}	0	0
E_g (eV)	2.17	1.900	1.5	3.9	3.500
χ(eV)	3.2	3.98	3.9	4.6	4.00
N_D (cm^{-3})	0	1×10^{9}	0	5.2×10^{19}	1×10^{18}
Dielectric Permittivity	7.11	10.00	28	9	9.00
μ_e(cm^2/Vs)	200	1.62×10^{5}	974	1.8×10^{1}	20
$v_{th,h}$ & $v_{th,e}$ (cm/s)	1×10^{7}	1×10^{7}	1×10^{7}	1×10^{7}	1×10^{7}
N_c (cm^{-3})	2.02×10^{17}	1×10^{16}	3.1×10^{18}	2.2×10^{18}	2.2×10^{18}
N_t(cm^{-3})	1×10^{14}	1×10^{16}	1×10^{16}	-	-
μ_h(cm^2/Vs)	80	1.010×10^{5}	213	1.8×10^{1}	10

N_v (cm^{-3})	1.1×10^{19}	1×10^{16}	3.1×10^{18}	1.8×10^{19}	1.8×10^{19}
References	[121]	[53]	[66]	[134]	[122]

In addition, the simulation of lead-free all-perovskite multijunction solar cells (APMJSC) based upon methyl ammonium germanium halide ($CH_3NH_3GeI_3$) and mixed halide layers ($FAMASnGeI_3$) is also included which has not been explored yet in the literature. Moreover, it is obtained from the literature that, individual $CH_3NH_3GeI_3$ and $FAMASnGeI_3$ based layers are compatible with low-temperature and solution processing methodology [37][40]. Hence, this chapter includes the standalone and all-perovskite multijunction solar cell study of the ($CH_3NH_3GeI_3$-$FAMASnGeI_3$) based perovskite solarcell as depicted in Fig. 5.2a, Fig. 5.2b, and Fig. 5.2c. The numerical parameters taken for the simulation of $CH_3NH_3GeI_3$-$FAMASnGeI_3$ based perovskite solar cell are given in Table 5.2.

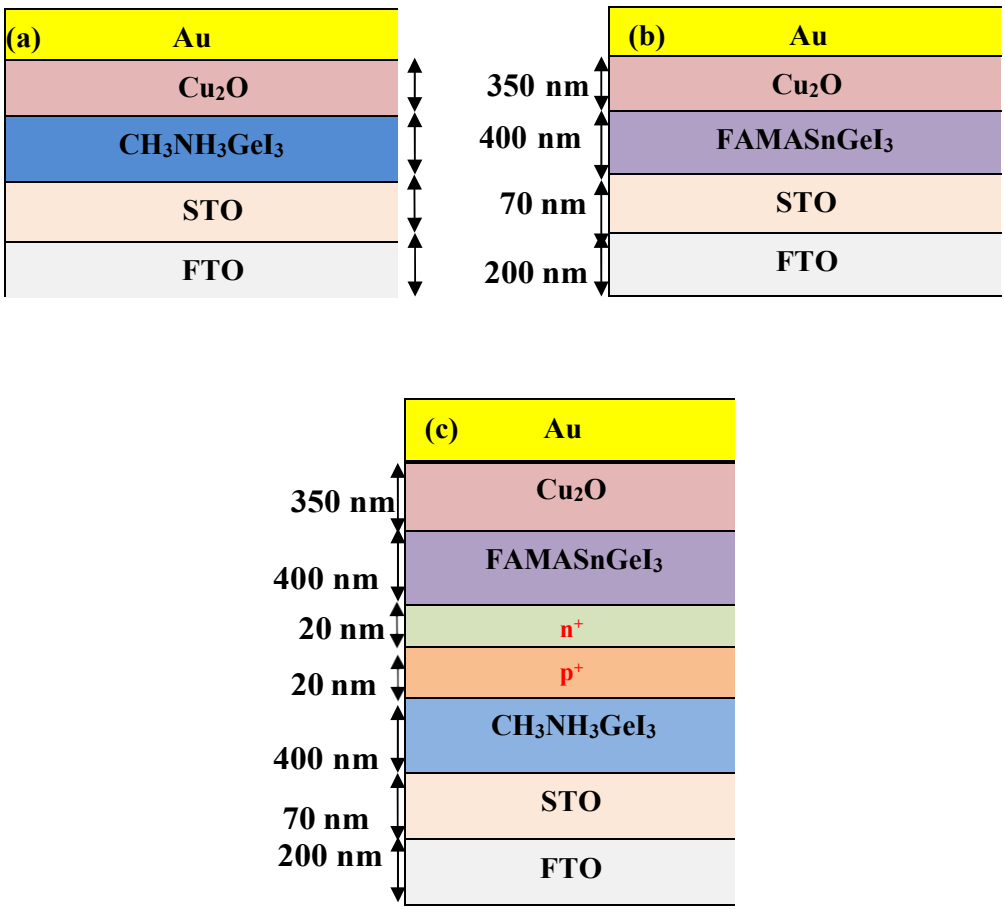

Fig. 5.2 Simulated structure of (a) $CH_3NH_3GeI_3$ based PSC (b) $FAMASnGeI_3$ based PSC (c) Multijunction structure of PSC

Table 5.2 Device layer properties consider for the HTL, absorber layers, ETL and TCO

Parameters	Cu_2O	$CH_3NH_3GeI_3$	$FAMASnGeI_3$	STO	FTO
Thickness (μm)	0.350	0.400	0.400	0.070	0.200
E_g(eV)	2.17	1.90	1.40	3.20	3.50
qχ (eV)	3.2	3.98	3.67	4.00	4.00
Dielectric Permittivity	7.11	10.00	8.20	8.70	9.00
Conduction Band Density of States (N_c)(cm^{-3})	2.02×10^{17}	1×10^{16}	2.2×10^{18}	1.7×10^{19}	2.2×10^{18}
Valence Band Density of States (N_v) (cm^{-3})	1.1×10^{19}	1×10^{16}	1.8×10^{19}	2×10^{20}	1.8×10^{19}
Electron thermal velocity (cm/s)	1×10^{7}	1×10^{7}	1×10^{7}	1×10^{7}	1×10^{7}
Hole Thermal Velocity (cm/s)	1×10^{7}	1×10^{7}	1×10^{7}	1×10^{7}	1×10^{7}
Electron mobility (cm^2/Vs)	200	1.62×10^{5}	2	5.3×10^{3}	20
Hole mobility (cm^2/Vs)	80	1.010×10^{5}	2	6.6×10^{2}	10

N_D (cm^{-3})	0	1×10^{9}	1×10^{13}	2×10^{16}	1×10^{18}
N_A (cm^{-3})	1×10^{18}	1×10^{9}	0	0	0
References	[121]	[53]	[52]	[130]	[122]

Furthermore, this chapter also discusses the effect of ETL and HTLs, as these layers play a substantial role in charge extraction from the perovskite absorber layer to the contacts. Due to restraints of the fabrication methods and the expensive transport layers, numerical simulation methodology is highly promising to comprehend the impact of various charge transport layers on the PV performance of Pb-free APMJSC. Further, to enhance the device efficiency the defect density of the perovskite layer is also explored. In addition, the effect of Φ_{BC} on APMJSC is also discussed.

5.2 Simulation Results

The simulated results obtained for the Pb-free APMJSC ($CH_3NH_3GeI_3$-$CsSnGeI_3$) and ($CH_3NH_3GeI_3$-FAMA$SnGeI_3$) is documented here.

5.2.1 $CH_3NH_3GeI_3$ and $CsSnGeI_3$ Based All-Perovskite Multijunction Solar Cell

The numerical parameters considered for HTM and ETM in the numerical simulation are given in Table 5.3, Table 5.4. The schematic diagram of APMJSC is given in Fig. 5.1. To provide an optoelectronic interconnection between the top and bottom sub cells a tunnel junction (n+/ p+ also called recombination layer) is introduced in such a way that it possesses negligible optical absorption and should have low series resistance as shown in Fig. 5.1. The simulated J-V curve for Pb-free ($CH_3NH_3GeI_3$-$CsSnGeI_3$) APMJSC configuration is plotted in Fig. 5.3.

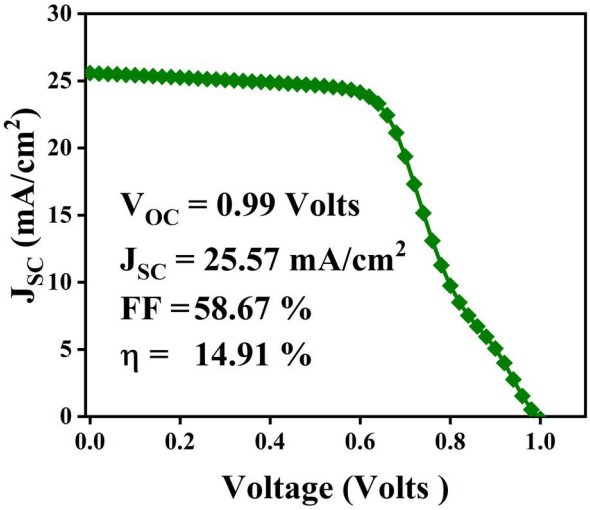

Fig. 5.3 Simulated J-V for Pb-free ($CH_3NH_3GeI_3$- $CsSnGeI_3$) APMJSC configuration

Table 5.3 Input parameters considered for different HTM

Parameters	$CuGaO_2$	CZTSe	SpiroOMeTAD	CuI
Thickness (μm)	0.350	0.350	0.350	0.350
Bandgap (eV)	3.58	1.4	3.06	2.98
Electron affinity (eV)	1.71	4.1	2.05	2.1
μ_h(cm^2/Vs)	1×10^{-2}	1.25×10^{1}	2×10^{-4}	1.69×10^{-4}
Electron thermal velocity (cm/s)	1×10^{7}	1×10^{7}	1×10^{7}	1×10^{7}
Dielectric Permittivity	3.3	9.00	3.00	6.5
N_A (cm^{-3})	1×10^{18}	1×10^{19}	1×10^{18}	1×10^{18}
N_V (cm^{-3})	4.38×10^{19}	1.8×10^{19}	1×10^{19}	1×10^{19}
μ_e(cm^2/Vs)	1×10^{-2}	1×10^{2}	1×10^{-4}	1.69×10^{-4}
N_C (cm^{-3})	4.38×10^{19}	2.2×10^{18}	2.8×10^{19}	2.8×10^{19}
Hole thermal velocity (cm/s)	1×10^{7}	1×10^{7}	1×10^{7}	1×10^{7}
References	[135]	[123]	[53]	[136]

Table 5.4 Input parameters considered for different ETM

Parameters	TiO_2	STO	C60	SnO_2
Thickness (μm)	0.070	0.070	0.070	0.070
Bandgap (eV)	3.200	3.2	1.7	3.6
Electron mobility (cm^2/Vs)	20	5.3×10^{3}	1×10^{-1}	1×10^{2}
Hole thermal velocity (cm/s)	1×10^{7}	1×10^{7}	1×10^{7}	1×10^{7}
Dielectric Permittivity	32.00	8.7	10	9
N_C (cm^{-3})	1×10^{19}	1.7×10^{19}	2.2×10^{18}	2.2×10^{18}
$v_{th,e}$ (cm/s)	1×10^{7}	1×10^{7}	1×10^{7}	1×10^{7}
Valence band density of states N_V (cm^{-3})	1×10^{19}	2×10^{20}	1.8×10^{19}	1.8×10^{19}
χ (eV)	3.9	4.0	4.5	4.5
Hole mobility (cm^2/Vs)	10	6.6×10^{2}	1×10^{-1}	2.5×10^{-1}
N_A (cm^{-3})	1×10^{17}	2×10^{16}	1×10^{16}	1×10^{20}
References	[53]	[128]	[40]	[40]

The all-perovskite multijunction solar cell allows maximum photons absorption. Hence, a significant improvement in the photovoltaic performance of APMJSC is obtained. With GZO as an ETL layer, the proposed all-perovskite multijunction solar cell shows 14.91% of PCE as shown in Fig. 5.3, is considered as a significant improvement in all-perovskite multijunction solar cell technology with GZO as an ETL.

5.2.1.1 Impact of HTL on the PV performance of Pb-free APMJSC

This section includes the impact of different HTL on PV performance of Pb-free APMJSC. Depend on the bandgap and electron affinity different HTL layers are arranged as given in Fig. 5.4(a-e). The energy band diagram for each HTL layer is shown in Fig. 5.5(a-e). Fig. 5.6a, Fig. 5.6b and Table 5.5 presents the obtained PV parameters of the simulated HTL for Pb-free APMJSC. The obtained J-V curve of various HTL for Pb-free APMJSC is given in Fig. 5.7. For effective transport of positive charge carriers (*i.e.,* holes) from perovskite to HTL, the E_{V_HTL} (*i.e.,* valence band maximum (VBM) of HTL) should be above the E_{V_PVK} (*i.e.,* VBM of perovskitelayer). To analyse the effect of HTL on PV performance the open-circuit voltage (V_{OC}) and built-in potential (V_{bi}) is correlated with E_{C_ETL}-E_{V_HTL} and Φ_{BC}-E_{C_ETL}. It is obtained from Table 5.5 that V_{bi} is primarily affected by E_{C_ETL}-E_{V_HTL} and Φ_{BC}- E_{C_ETL}. Table 5.5 revealed that when E_{C_ETL}-E_{V_HTL} is more than Φ_{BC}- E_{C_ETL} then V_{bi} is mainly influencedby Φ_{BC}- E_{C_ETL}. In contrast, when E_{C_ETL}-E_{V_HTL} is lesser than Φ_{BC}- E_{C_ETL} then V_{bi} is nearer to E_{C_ETL}-E_{V_HTL}. In the case of CuI and CZTSe, the V_{bi} (built-in potential) is nearer to E_{C_ETL}-E_{V_HTL} as in both the cases, E_{C_ETL}-E_{V_HTL} is lesser than Φ_{BC}- E_{C_ETL}. The obtained V_{bi} is around 0.52 eV and hence low V_{OC} is obtained as compared to other HTLs. Also, despite having better V_{bi} of spiroOMeTAD *i.e.,* 0.60 eV, which is similar to $CuGaO_2$, spiroOMeTAD exhibits poor photovoltaic performance. The comparatively less efficiency of spiroOMeTAD is attained, because of its limited mobility of charge of the order of ~ 10^{-4} cm^2/Vs. However, spiroOMeTAD shows good V_{OC} as a high barrier is created for electrons as shown in Fig. 5.4d, which limits the propagation of electrons via HTL. Moreover, it has been obtained from Fig. 5.4(a-b) and Fig. 5.5(a-b) that Cu_2O and $CuGaO_2$ show comparatively higher photovoltaic performance among other HTL alternatives. This is mainly due to its better energy band alignment with the perovskite layer. However, comparatively less efficiency is achieved for $CuGaO_2$ due to its lower charge carrier mobility (*i.e.,* 1×10^{-2} cm^2/Vs). It is obtained from Fig. 5.6(a-b) and Fig. 5.7 that, Cu_2O shows the highest V_{OC} (0.99 V) and efficiency (14.91%). This is due to its proper band alignment as well as high electron and hole mobility, hence Cu_2O is considered as the most suitable material among all other HTLs for the

application of Pb-free APMJSC. It is also concluded that the highest V_{bi} corresponds to the highest V_{OC}.

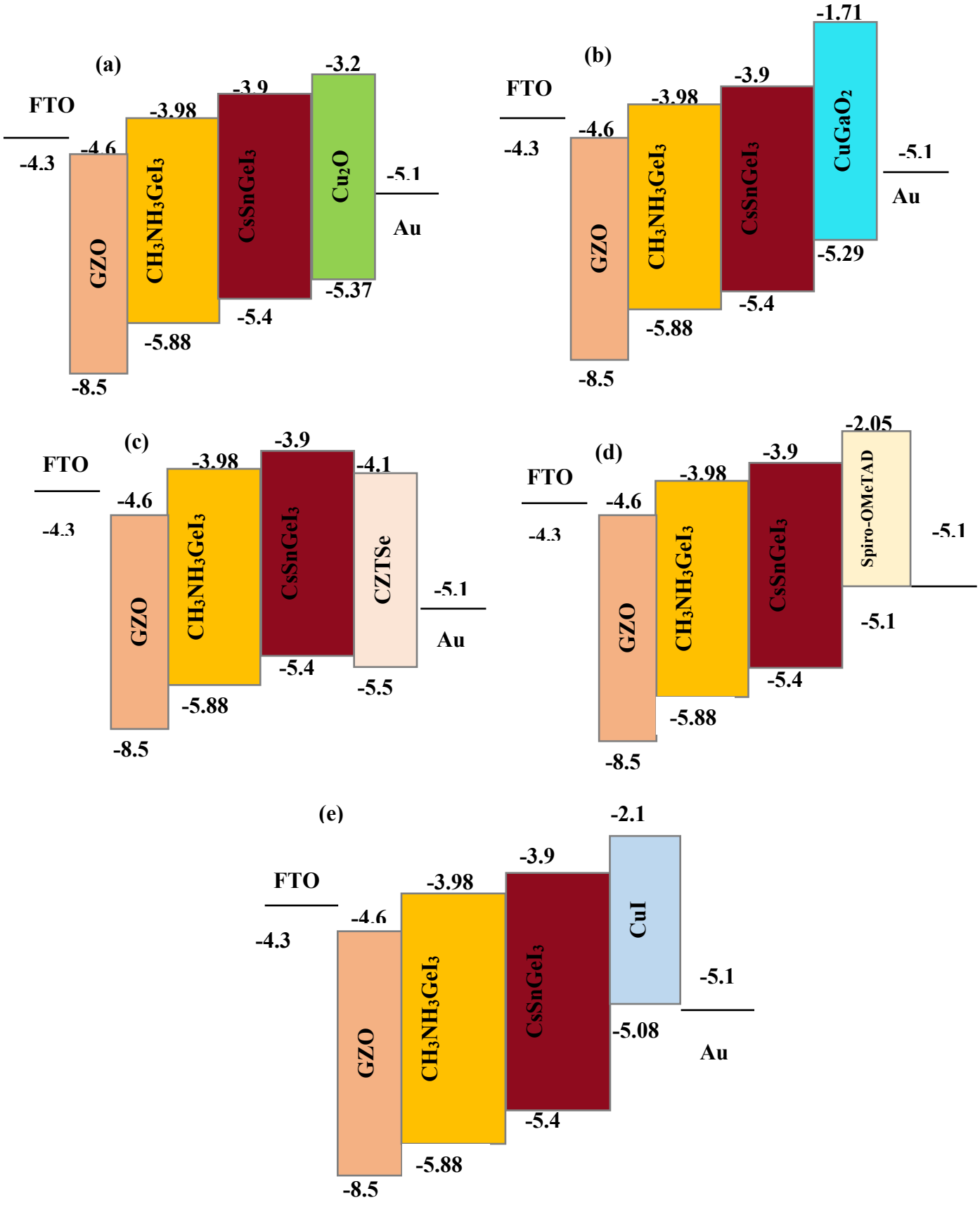

Fig. 5.4. Energy band alignment diagram for various HTL considered for the simulation of Pb-free APMJSC (a) Cu_2O (b) $CuGaO_2$ (c) CZTSe (d) SpiroOMeTAD (e) CuI

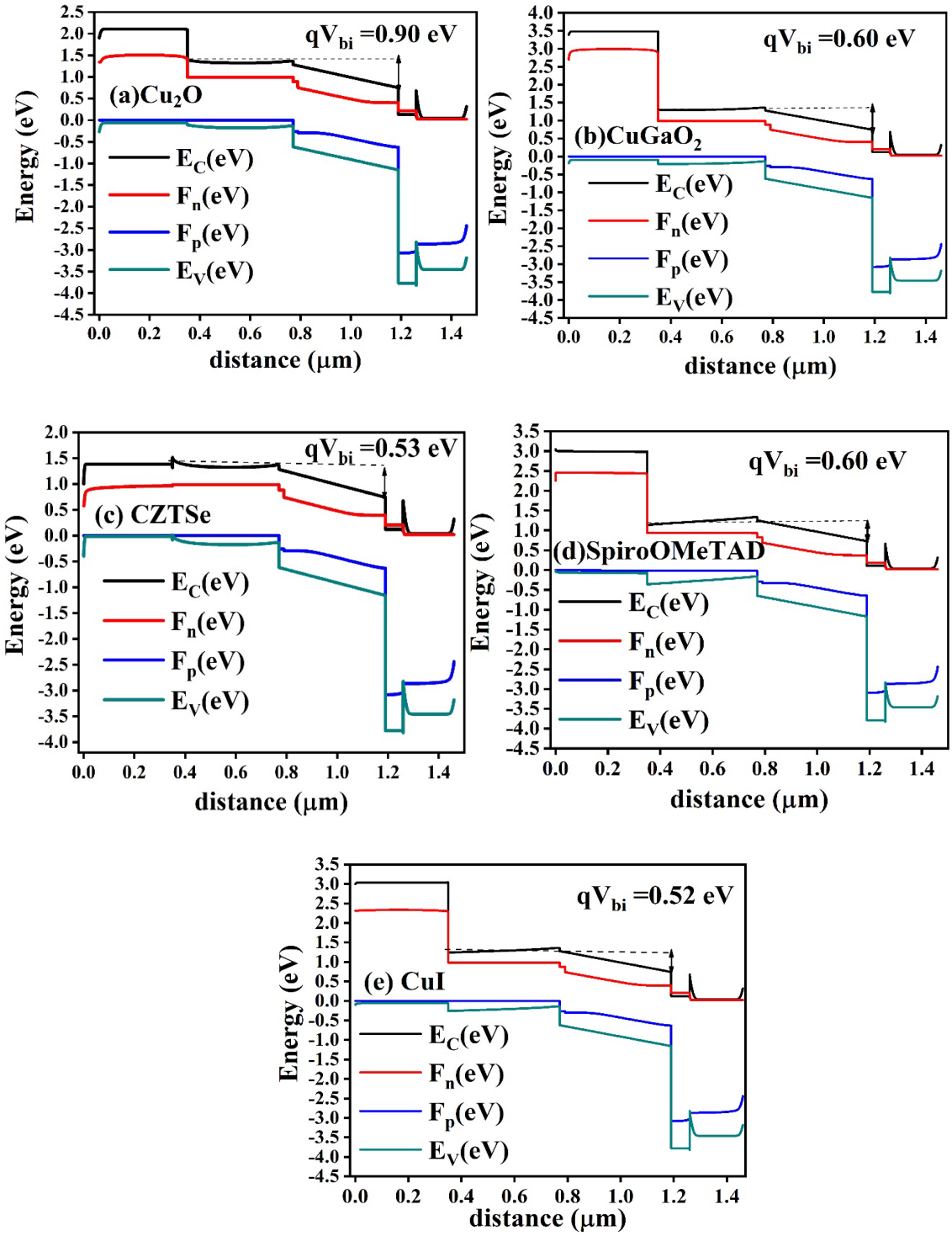

Fig. 5.5. Energy band diagram of HTL obtained from the simulation of Pb-free APMJSC (a) Cu_2O (b) $CuGaO_2$ (c) CZTSe (d)SpiroOMeTAD (e) CuI

Table 5.5 The different parameters of APMJSC with different HTLs

Different HTL Layers	E_{C_ETL}-E_{V_HTL}	Φ_{BC}-E_{C_ETL}	V_{bi} (Volts)	V_{OC} (Volts)	J_{SC} (mA/cm^2)	FF (%)	η (%)
Cu_2O	0.77	0.5	0.90	0.99	25.57	58.67	14.91
$CuGaO_2$	0.69	0.5	0.60	0.97	24,94	56.62	13.70
CZTSe	0.5	0.5	0.53	0.94	23.26	54.21	11.95
Spiro-OMeTAD	0.9	0.5	0.60	0.92	18.69	53.28	9.22
CuI	0.48	0.5	0.52	0.94	23.47	54.12	12.05

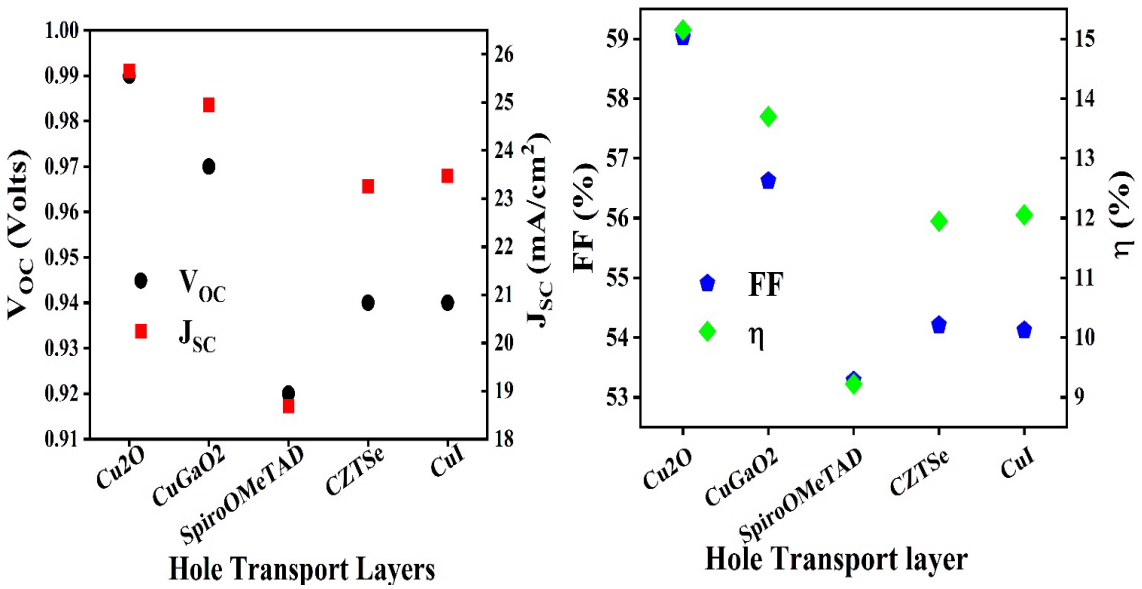

Fig. 5.6. Simulated results obtained from different HTL for APMJSC (a) V_{OC} and J_{SC} (b) FF and η

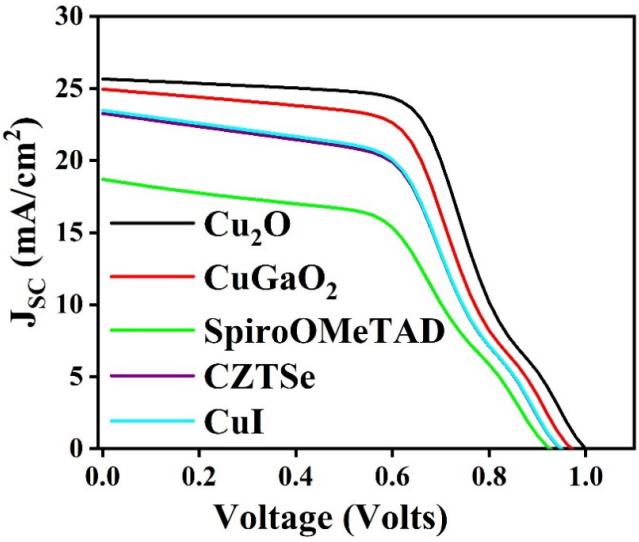

Fig. 5.7. J-V curve of simulated hole transport layer for APMJSC

5.2.1.2 Impact of ETL on the PV performance of Pb-free APMJSC

This section discusses the impact of various ETLs on the PV performance of APMJSC. To inspect the impact of various ETLs, the layers are aligned depending on their E_C and E_V levels, as well as their electron affinity and bandgap. The energy band alignment diagrams and simulated energy band diagram for various ETL are given in Fig. 5.8(a-e) and Fig. 5.9(a-e). The photovoltaic performance obtained for a different electron transport layer is summarized in Fig. 5.10(a-b). Table 5.6 consists of the simulated photovoltaic parameters. Fig. 5.11 depicts the J-V characteristics of different ETL for Pb-free APMJSC. For the proper transport of electrons from the perovskite absorber layer to the ETL, E_{C_ETL} should be lower than the E_{C_PVK}. It is obtained from Table 5.6, Fig. 5.10 and Fig. 5.11 that GZO shows the worst device performance, whereas STO depicts the best device power conversion efficiency of 23.96 %. It is obtained from Table 5.6 that in the case of GZO, C60 and SnO_2 when E_{C_ETL}-E_{V_HTL} is less than Φ_{FC}- E_{V_HTL} and thus V_{bi} is mainly influenced by E_{C_ETL}-E_{V_HTL}. On the contrary, when E_{C_ETL}-E_{V_HTL} is greater than Φ_{FC}- E_{V_HTL} (*i.e.,* STO, TiO_2) V_{bi} is nearer to Φ_{FC}- E_{V_HTL}. Table 5.6 shows that the trend of having the V_{OC} is almost similar to V_{bi} except for the case of C60. When C60 is used as an ETL layer it shows low V_{bi} and low E_{C_ETL}-E_{V_HTL}, still comparatively highest V_{OC} is attained with device efficiency limited to 16.69%. This is mainly due to the reason that the C60 has a

smaller band gap and since the light is entering from the ETL layer, C60 isthe light facing layer, and thus absorbs most of the light spectrum. Because of the increased absorption of photons at the C60 layer, the generated charge carriers reaches very fast to the electrode as the electron need to travel a very small distance to reach the electrode. However, the generated holes within the ETL layer are recombined before getting collected at the electrodes and are unable to participate in the conduction. This can beconfirmed by the S-shaped J-V curve obtained for the C60 layer as depicted in Fig. 5.10. Moreover, for SnO_2, the performance is limited due to its higher electron affinity than the Φ_{FC} which leads to the barrier for the majority charge carrier and thus mainly affects theFF of the device. Moreover, the lower electron mobility and the less V_{bi} are also restricting the device performance. Fig. 5.10, Fig. 5.11 and Table 5.6 illustrates that TiO_2 and STO show the best device performance among all the ETL layer used. This is mainly due to the fact, that these layers show the highest V_{bi} along with its better energy band alignment with perovskite as well as front contact. This led to the high V_{OC} and better FF and thus the overall device performance. Hence, both STO and TiO_2 are considered eminent layers for ETL in Pb-free APMJSC applications. Despite having a slightly better photovoltaic performance of STO, still, it is very challenging to obtain low-temperature solution processing STO that exhibits good hole blocking capability [141][142]. Hence, Cu_2O and TiO_2 are considered as charge transport layers for the present study.

Table 5.6 Impact of various ETL on the PV performance of APMJSC

Different ETL	E_{C_ETL}-E_{V_HTL}	Φ_{FC}-E_{V_HTL}	V_{bi} (Volts)	V_{OC} (Volts)	J_{SC} (mA/cm^2)	FF (%)	η (%)
GZO	0.77	1.07	0.90	0.99	25.65	59.03	15.15
STO	1.37	1.07	1.11	1.11	25.84	83.51	23.96
C60	0.87	1.07	0.69	1.57	25.66	41.14	16.69
SnO_2	0.87	1.07	0.98	1.09	25.63	77.08	21.54
TiO_2	1.47	1.07	1.10	1.10	25.84	83.02	23.69

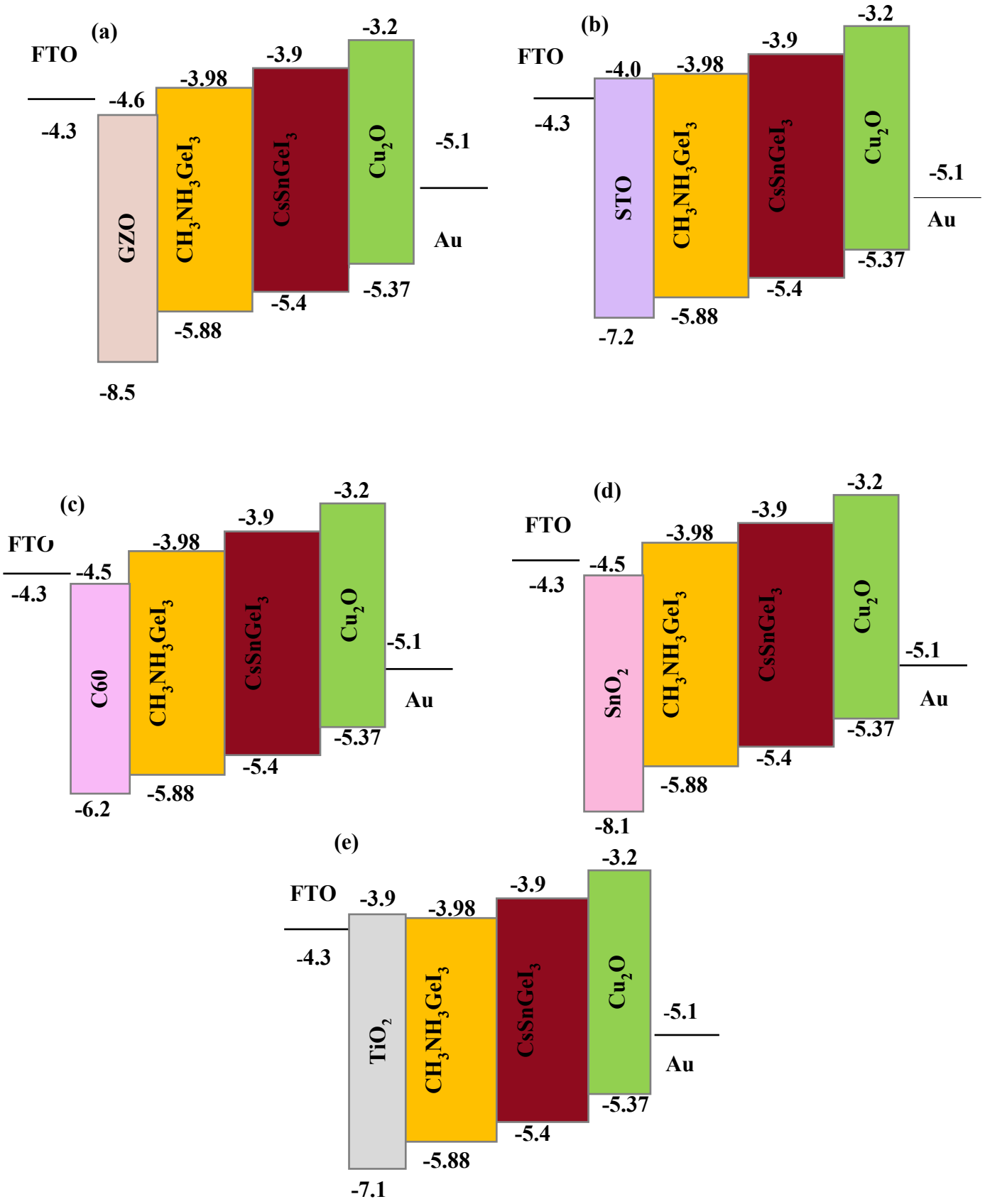

Fig. 5.8. Energy band alignment diagram for various ETL considered for the simulation of Pb-free APMJSC(a) GZO (b) STO (c) C60 (d)SnO_2 (e) TiO_2

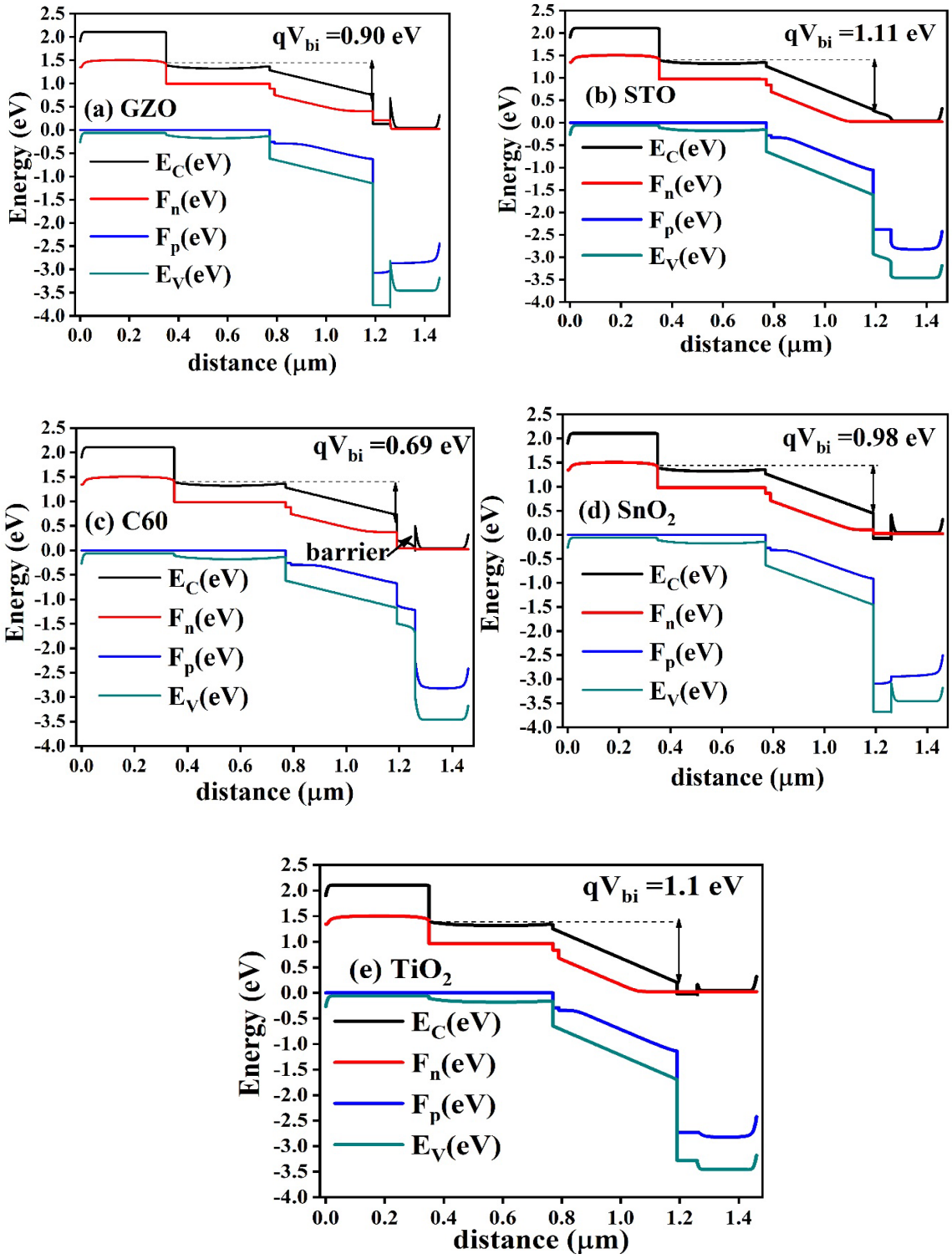

Fig. 5.9. Energy band diagram of ETL obtained from the simulation of Pb-free APMJSC (a) GZO (b) STO (c) C60 (d) SnO_2 (e) TiO_2

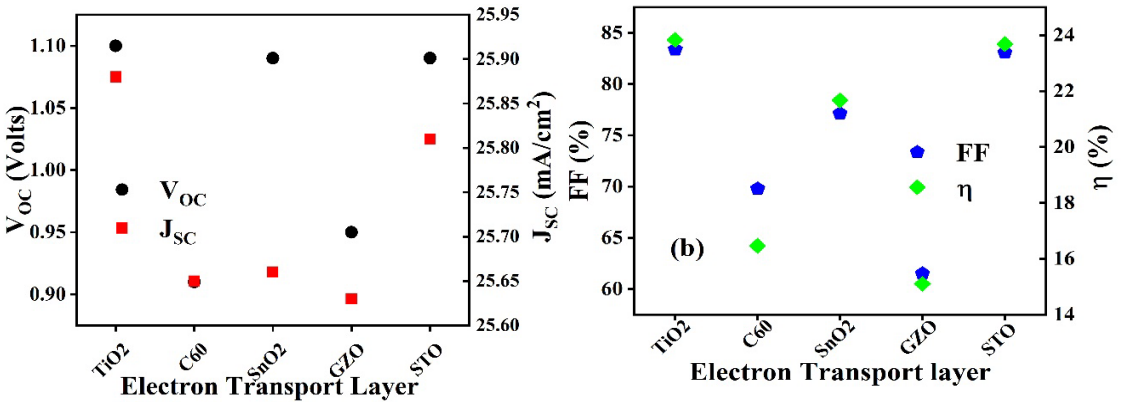

Fig. 5.10. Simulated results obtained from different ETL for APMJSC (a) V_{OC} and J_{SC} (b) FF and η

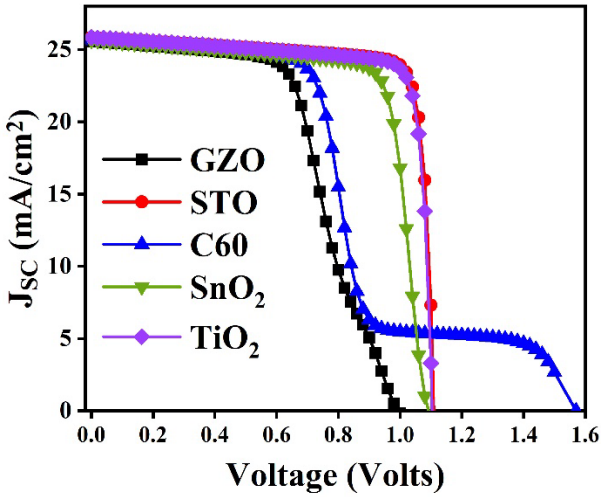

Fig. 5.11. J-V curve of simulated ETL for Pb-free APMJSC

5.2.1.3 Impact of perovskite defect density on the PV performance of Pb-free APMJSC

The PV performance of the APMJSC expects a great deal on the defects associated with the absorber layers. The study of recombination mechanisms due to defects also make a crucial contribution to the device performance. In this study, to investigate the impact of defect density on the absorber layer, the Shockley–Read–Hall (R_{SRH}) recombination model has been used as given in Eq. 5.1 and Eq. 5.2.

$$R_{SRH} = \frac{np - n_i^2}{\tau_p(n + n_i) + \tau_n(p + p_i)} \quad \textbf{Eq. 5.1}$$

$$\tau_{n,p} = \frac{1}{\sigma v_{th,n,p} N_t} \quad \textbf{Eq. 5.2}$$

where,

R_{SRH}= Schockley–Read–Hall recombination rate,

τ_p, τ_n = lifetime of hole and electron

This section includes the study of variation of defect density of narrow bandgap perovskite layer (*i.e.,* $CsSnGeI_3$) from 1×10^{14} cm^{-3} to 1×10^{18} cm^{-3}. The defect density of the wide bandgap perovskite layer (*i.e.,* $CH_3NH_3GeI_3$) remains unchanged at 1×10^{16} cm^{-3}. It is illustrated in Fig. 5.12(a-b) that the increment of defect density of $CsSnGeI_3$ from 1×10^{14} cm^{-3} to 1×10^{18} cm^{-3} led to the reduction in V_{OC} and J_{SC} from 1.20 V to 1.02 V & 25.99 mA/cm^2 to 19.71 mA/cm^2, respectively as shown in Fig. 5.12a. However, the FF and η drop from 84.85 % to 71.14 % and 26.47 % to 14.41%, respectively as depicted in Fig. 5.12b.

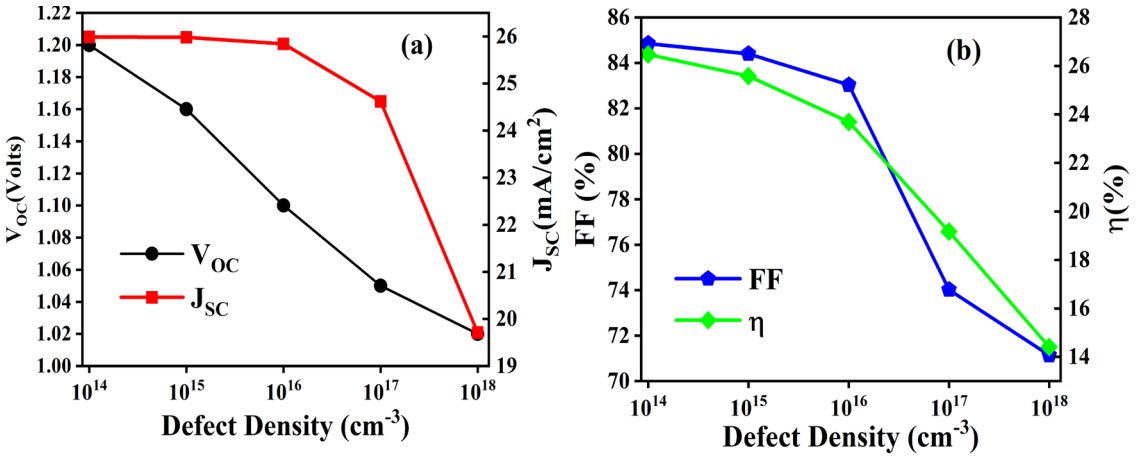

Fig. 5.12. Effect of the variation of defect density of $CsSnGeI_3$ perovskite with constant defect density at 1×10^{16} cm^{-3} for $CH_3NH_3GeI_3$ (a) V_{OC} & J_{SC} (b) FF & η

Fig. 5.13 (a-b) corresponds to the study of variations in defect density of wide bandgap perovskite layer ($CH_3NH_3GeI_3$) from 1×10^{14} cm^{-3} to 1×10^{18} cm^{-3}, by keeping the narrow bandgap perovskite layer ($CsSnGeI_3$) defect density, constant at 1×10^{14} cm^{-3}. It

is illustrated from Fig. 5.13a, that with the variation of the defect density from 1×10^{14} cm^{-3} to 1×10^{18} cm^{-3}, V_{OC} is reduced from 1.20 V to 1.18 V but almost constant J_{SC} is obtained. Correspondingly, the FF and η drop from 85.31% to 69.42% and 26.64% to 21.29%, respectively as depicted in Fig. 5.13b. Hence, it is concluded that there is a significant impact of defect density on the overall device performance as high defect density leads to inadequate device performance.

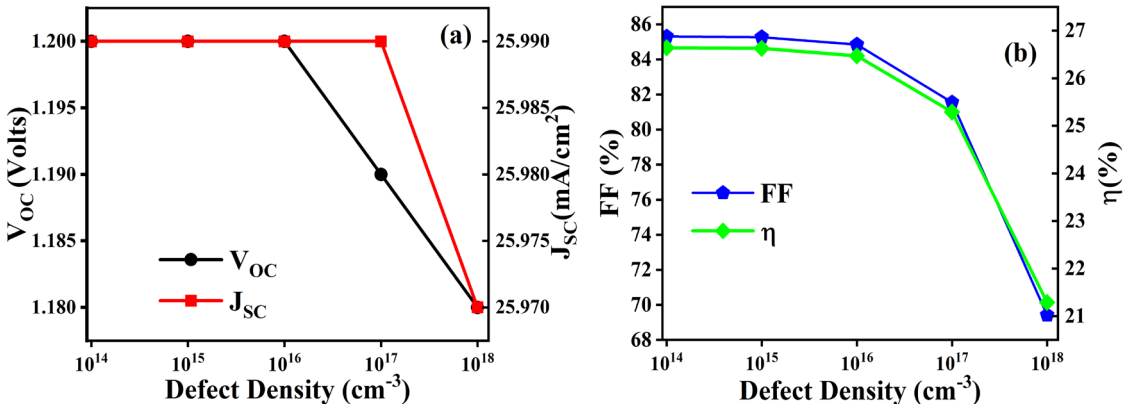

Fig. 5.13. Effect of the variation of defect density of $CH_3NH_3GeI_3$ perovskite with constant defect density at 1×10^{14} cm^{-3} for $CsSnGeI_3$ constant at (a) V_{OC} & J_{SC} (b) FF & η

The reduction of photovoltaic performance by increasing defect density is due to the creation of more recombination centres within the absorber layer. The increased recombination centres led to the reduction of diffusion length of generated carriers as well as the reduced lifetimes of the photogenerated carriers, and hence the overall device performance degrades as given in Eq. 5.1 and Eq. 5.2. Furthermore, the extreme defects of the perovskite layer limit the shunt resistance of the device which degrades the V_{OC} of the device.

It is obtained from Fig. 5.12 and Fig. 5.13 that 1×10^{14} cm^{-3} defect density is considered as an optimum value for perovskite layers in Pb-free APMJSC, which will effectively improve the overall device efficiency. The V_{OC}, J_{SC}, FF and efficiency of the APMJSC are found to be 1.20V, 25.99 mA/cm^2, 85.31 % and 26.64 % respectively. The results show that the defect density of individual layers. To obtain a better result of multijunction solar cells it is advisable to have defect density ~1×10^{14} cm^{-3}.

5.2.1.4 Impact of bottom contact work function (Φ_{BC}) on the PV performance of APMJSC

The back electrode metal work function shows a profound effect on the device performance. The ohmic contact between the HTL and back contact is an essential condition to effectively transport the charge carrier from HTL to back contact. The proposed study includes the effect of different metal electrodes is explored for APMJSC. The metal work function considered for the simulation is varied from 4.65 eV to 5.65 eV.

Fig. 5.14a and Fig. 5.14b shows the impact of Φ_{BC} on the photovoltaic performance of APMJSC. It is seen that with the increase of Φ_{BC} till 5.0 eV, the V_{OC}, FF and η increases and reach maximum values and saturates thereafter. The optimized PCE of APMJSC is surmounted to 26.64% i.e., (V_{OC}=1.20 V, J_{SC}= 25.99 mA/cm^2, FF =85.31 % and η=26.64 %) at 5.0 eV. Fig. 5.14a and Fig. 5.14b shows the significant improvement in the overall device photovoltaic performance, with the enhancement of Φ_{BC}.

At 4.65 eV of Φ_{BC}, the device efficiency reaches up to 22.00%. However, the device efficiency increases up to 26.64 % as the Φ_{BC} increases from 4.65 eV to 5.00 eV. This is mainly due to the presence of a barrier between the bottom electrode and hole transport layer at 4.65 eV work function, however with the further increment of Φ_{BC} till 5.0 eV the barrier height of the majority carriers gets diminished. A barrier for the hole is created between the HTM and back contact interface when the $\Phi_{BC} \leq E_{V\_HTL}$ is shown in Fig. 5.15a.

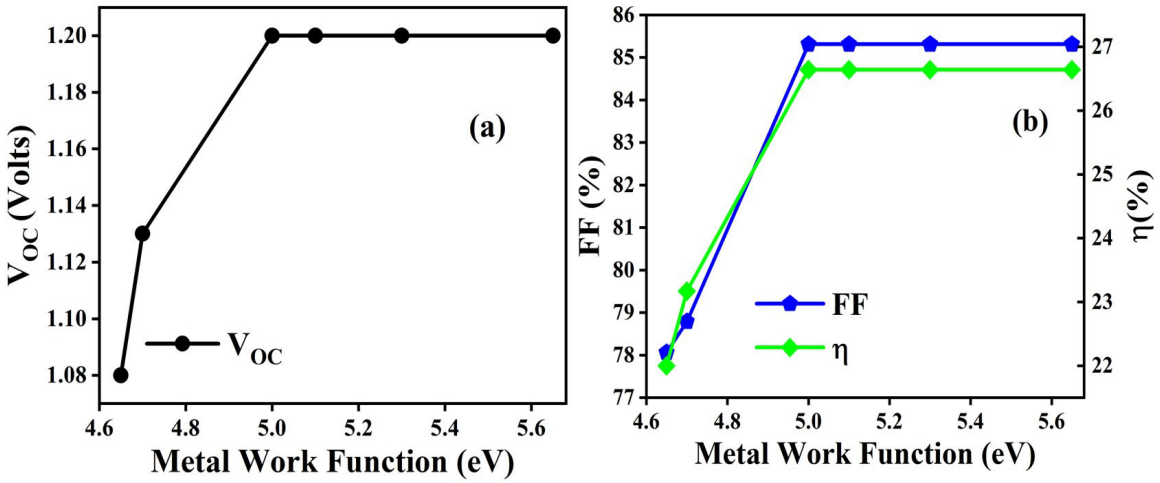

Fig. 5.14. Impact of variation of metal work function for APMJSC (a) V_{OC} & J_{SC} (b) FF& η

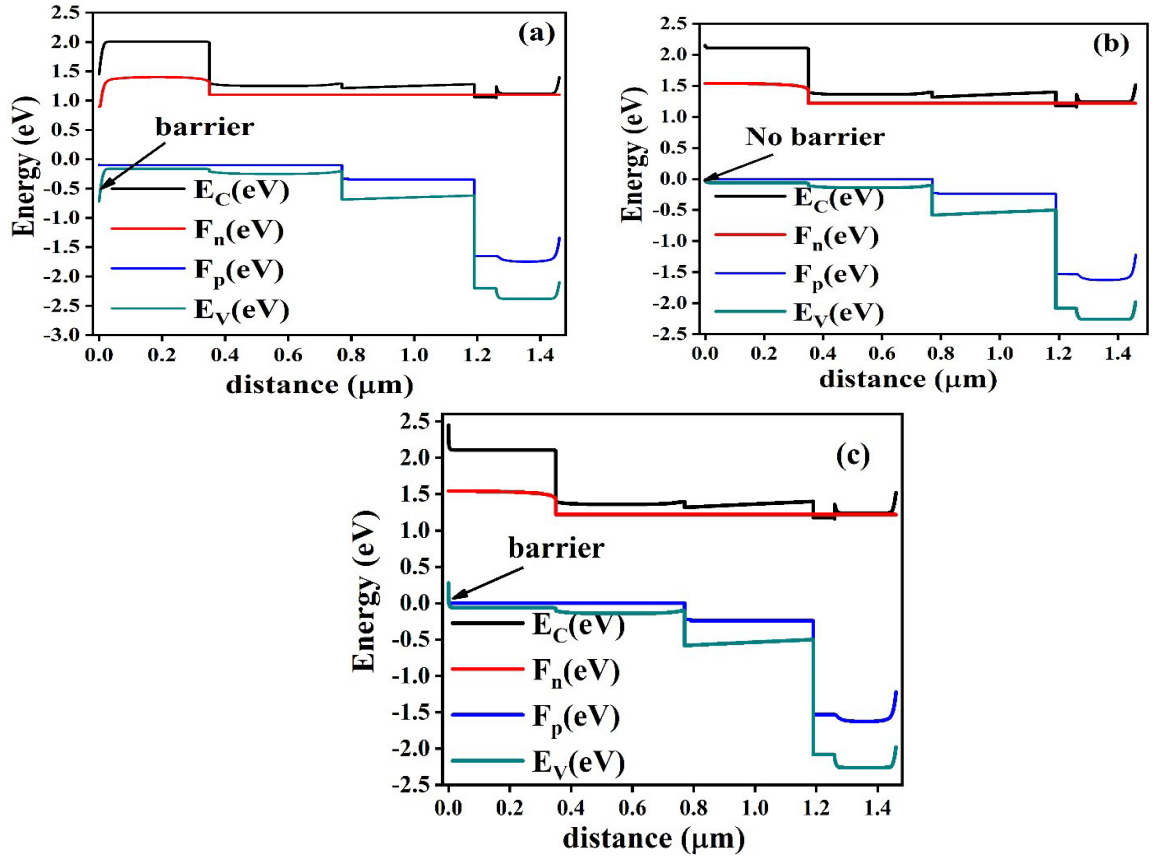

Fig. 5.15. Energy band diagram at different metal work function of APMJSC (a) at ϕ =4.65 eV (b) at ϕ =5.0 eV (c) at ϕ =5.65 eV

Moreover, with the further increase in Φ_{BC} from 4.65 eV to 5.00 eV, it coincides with the fermi level of HTM and hence, a barrier-less contact is formed between the HTM/Φ_{BC} interface as shown in Fig. 5.15b.

Further increase of the Φ_{BC} above 5.0 eV, the photovoltaic performance gets saturated due to the restriction of charge carrier collection. This is due to the creation of a barrier for electrons between HTM layer/back contact as the hole collection is dominated at the HTM/back contact interface, resulting in no significant improvement of the photovoltaic performance.

Hence, it is suggested that when Cu_2O and TiO_2 are taken as a charge transport layers, the Φ_{BC} should not be less than 5.0 eV to attain the high PV performance of APMJSC. Also, Pb-free APMJSC exhibits far more efficient PV performance as compare to standalone $CH_3NH_3GeI_3$ and $CsSnGeI_3$ based Pb-free PSC.

From the above study using the optimized parameters of the HTL, ETL, defect density, and metal work function, the final J-V curve of $CH_3NH_3GeI_3$ and $CsSnGeI_3$ APMJSC is indicated in Fig. 5.16. It is illustrated from Fig. 5.16 that the proposed APMJSC possesses V_{OC}= 1.20 V, J_{SC}=25.99 mA/cm^2, η= 26.64% and FF=85.31% which is far better than that of standalone $CsSnGeI_3$ and $CH_3NH_3GeI_3$ based perovskite solar cells. Table 5.7 depicts the optimized parameters obtained after each step. Table 5.8 compares the PSC performance of the proposed multijunction solar cell with the reported ones so far in the literature.

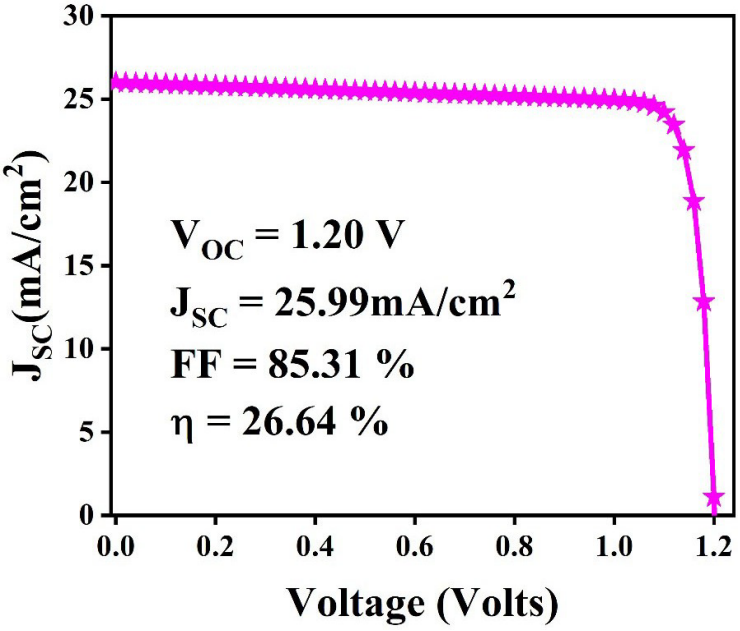

Fig. 5.16. Simulated optimized J-V curve of $CH_3NH_3GeI_3$ and $CsSnGeI_3$ APMJSC

Table 5.7 Device photovoltaic performance attained by optimizing each parameter

Device photovoltaic parameters	Primary multijunction structure	After charge transport layer optimization	Final optimized parameters
V_{OC} (Volts)	0.99	1.10	**1.20**
J_{SC} (mA/cm^2)	25.57	25.84	**25.99**
FF (%)	58.67	83.02	**85.31**
η (%)	14.91	23.69	**26.64**

Table 5.8 Comparison of proposed work with other layer configurations of tandem perovskite solar cell

Layer arrangement	V_{OC} (V)	J_{SC} (mA/cm^2)	FF (%)	η (%)	References
F.Jiang *et.al.,*	1.89	6.61	56.00	7.00	[33]
J.H.Heo *et.al.,*	1.95	8.40	66	10.80	[34]

G.E.Eperon *et.al.,*	1.60	14.50	70	16.90	[36]
A.Rajagopal *et.al.,*	1.98	12.70	73	18.40	[35]
D.Zhao *et.al.,*	1.92	14.00	78.10	21.00	[37]
A.F. Palmstrom *et.al.,*	1.88	16.00	77.00	21.30	[115]
J.Tong *et.al.,*	1.91	14.99	79.76	22.90	[38]
$Au/Cu_2O/CsSnGeI_3/CH_3NH_3GeI_3/TiO_2/FTO$	**1.20**	**25.99**	**85.31**	**26.64**	**[This Work]**

5.2.2 $CH_3NH_3GeI_3$ and $FAMASnGeI_3$ Based All-Perovskite Multi-Junction Solar Cells

To understand the PV performance of the lead-free all-perovskite multijunction solar cell, initially, the device performance of single-layer PSC based on $CH_3NH_3GeI_3$ and $FAMASnGeI_3$ layers have been investigated. The device structures for single layer and multijunction perovskite solar cells have been shown in Fig. 5.2a, Fig. 5.2b and Fig. 5.2c. The numerical parameters considered for different ETLs is given in Table 5.9. The standalone Pb-free ($CH_3NH_3GeI_3$ and $FAMASnGeI_3$ perovskites) configuration J-V curve is given in Fig. 5.17a and Fig. 5.17b. However, the J-V curve of the multijunction solar cell configuration is depicted in Fig. 5.18.

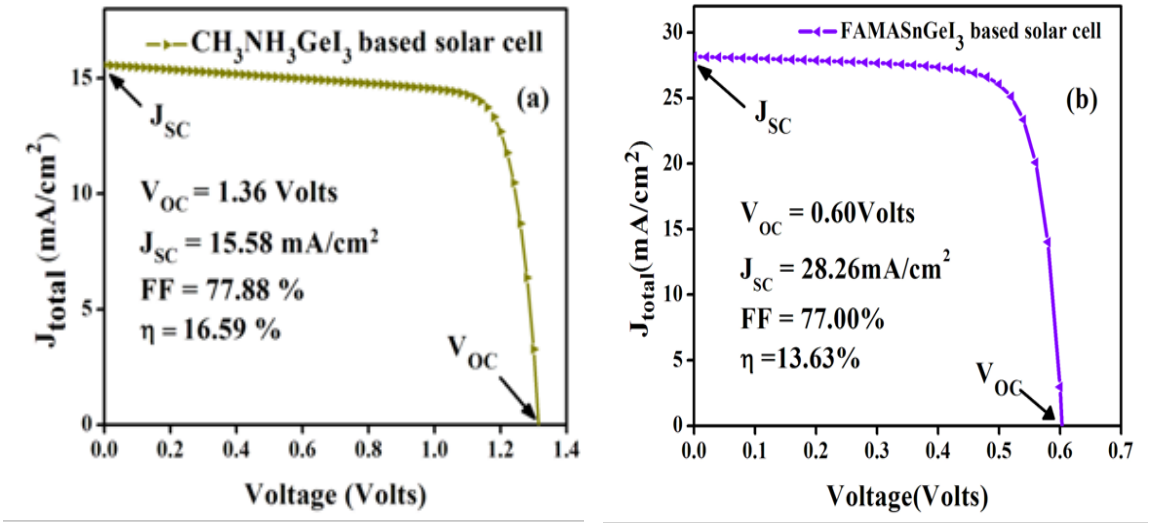

Fig. 5.17. Simulated J-V curve of (a) $CH_3NH_3GeI_3$ based solar cell (b) $FAMASnGeI_3$ based solar cell

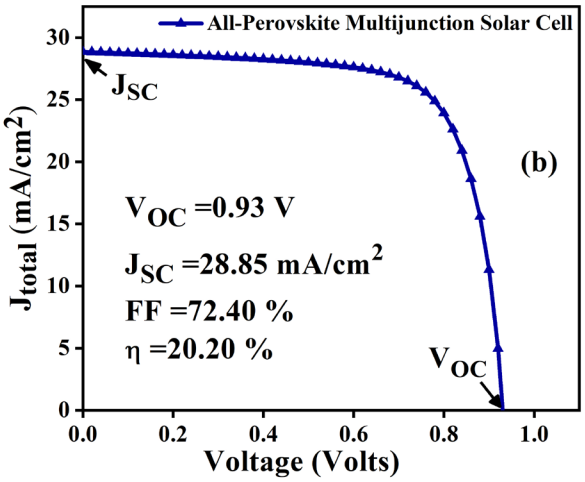

Fig. 5.18. J-V curve of Pb-free ($CH_3NH_3GeI_3$ and $FAMASnGeI_3$) based multijunction solar cell

Table 5.9 Numerical parameters taken for different ETLs

Parameters	SnO_2	IGZO	PCBM	TiO_2	ZnO
Thickness (μm)	0.070	0.070	0.070	0.070	0.070
Band-gap(eV)	3.6	3.05	2.1	3.26	3.3

Electron affinity (eV)	4.5	4.16	3.9	4.2	4.0
Dielectric Permittivity	9	10	3.9	10	9.0
N_c)cm^{-3})	2.2×10^{18}	5×10^{18}	2.2×10^{19}	2.2×10^{18}	3.7×10^{18}
N_v (cm^{-3})	1.8×10^{19}	5×10^{18}	2.2×10^{19}	1.8×10^{19}	1.8×10^{19}
Electron thermal velocity (cm/s)	1×10^{7}	1×10^{7}	1×10^{7}	1×10^{7}	1×10^{7}
Hole Thermal Velocity (cm/s)	1×10^{7}	1×10^{7}	1×10^{7}	1×10^{7}	1×10^{7}
Electron mobility (cm^2/Vs)	100	15	1×10^{-3}	100	100
Hole mobility (cm^2/Vs)	25	0.1	2×10^{-3}	25	25
N_D (cm^{-3})	1×10^{20}	1×10^{18}	1×10^{20}	1×10^{19}	5×10^{17}
References	[137]	[54]	[122]	[121]	[138]

5.2.2.1 Effect of different electron transport layers (ETLs) on lead-free all-perovskite multijunction solar cells

The optimization of the ETLs have been done based on the analysis of built-in potential (V_{bi}) which is generated across the perovskite layers and finally, the V_{bi} is correlated with the obtained V_{OC}. The V_{bi} is determined by the difference between the $E_{C\_ETL/CH3NH3GeI3}$ interface and $E_{C\_FAMASnGeI3/HTL}$ interface. The energy band alignment diagrams of the different ETL on all-perovskite multijunction solar cell are given in Fig. 5.19a, Fig. 5.19b, Fig. 5.19c and Fig. 5.19d. The band diagrams of multijunction solar cells with different ETLs has been shown in Fig. 5.20a, Fig. 5.20b, Fig. 5.20c and Fig. 5.20d. The

resulting V_{bi} of the different ETLs is shown in Table 5.10. Based on band alignment four different cases of ETLs are studied and their J-V curve is obtained as shown in Fig. 5.21.

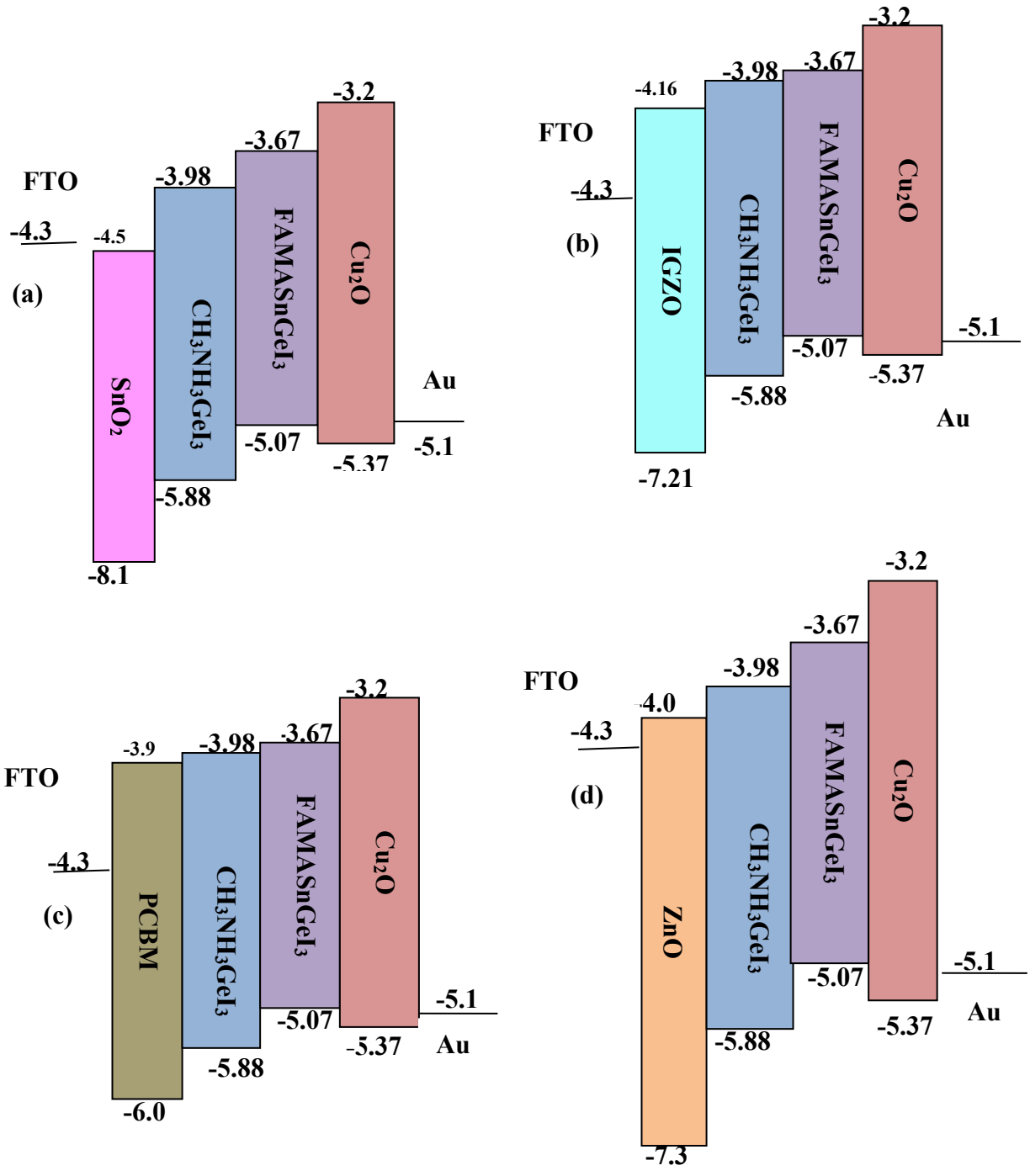

Fig. 5.19. Energy band alignment of different electron transport layers used in all-perovskite multijunction solar cell (a) SnO_2 (b IGZO (c) PCBM (d) ZnO

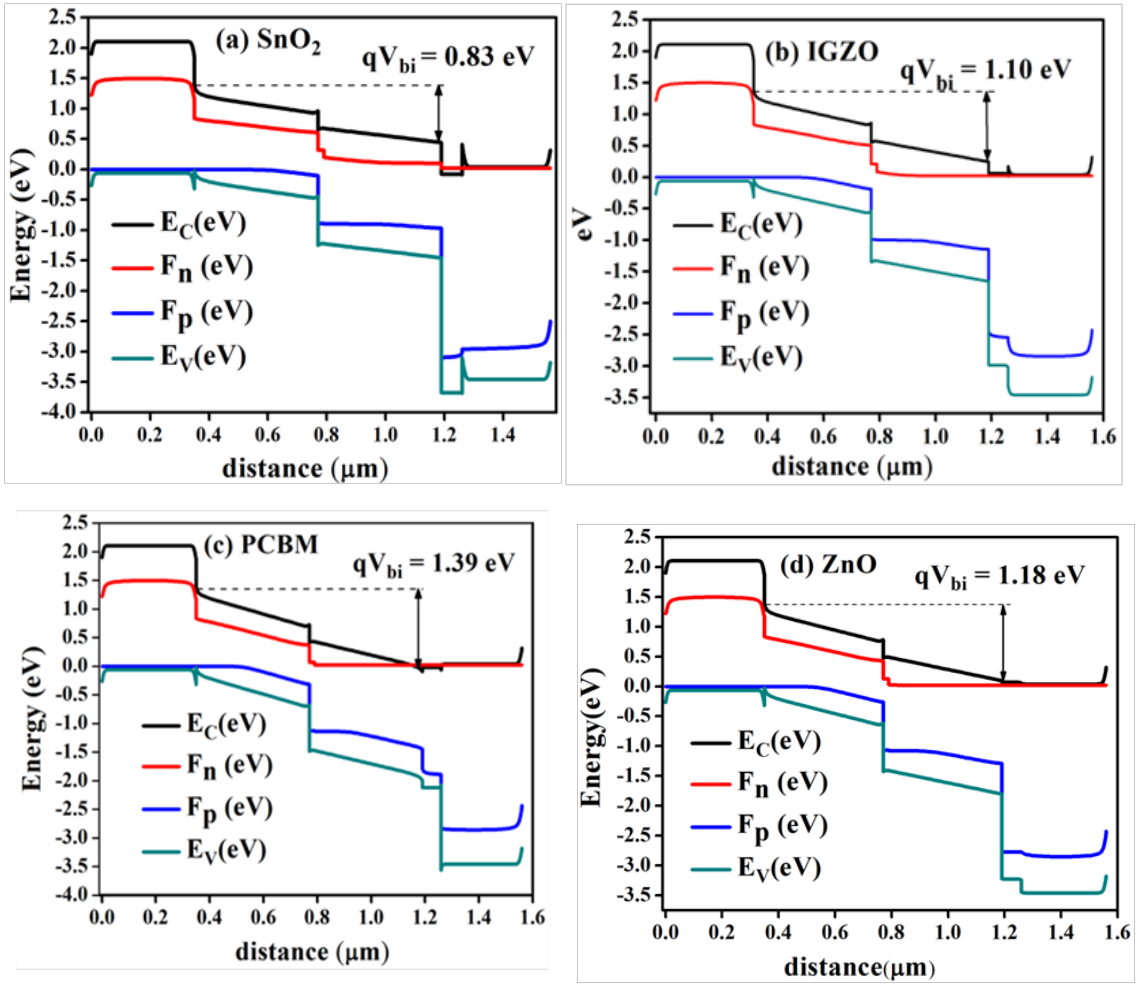

Fig. 5.20 Energy band diagram of electron transport layers used in all-perovskite multijunction solar cell (a) SnO_2 (b) IGZO (c) PCBM (d) ZnO

Table 5.10 Effect of E_{C_ETL} -E_{V_HTL} and Φ_{FC}-E_{V_HTL} , V_{bi} , V_{OC} , J_{SC} , FF and η of different ETLs on photovoltaic performance

Different ETL combination	E_{C_ETL} - E_{V_HTL} (eV)	Φ_{FC}- E_{V_HTL}	V_{bi} (V)	V_{OC} (V)	J_{SC} (mA/cm^2)	FF (%)	η (%)
SnO_2	0.87	1.07	0.83	0.860	28.68	62.85	16.13
IGZO	1.21	1.07	1.10	0.927	28.85	69.70	19.39

PCBM	1.47	1.07	1.39	0.945	27.78	78.68	21.47
ZnO	1.37	1.07	1.18	0.944	28.87	77.83	22.04

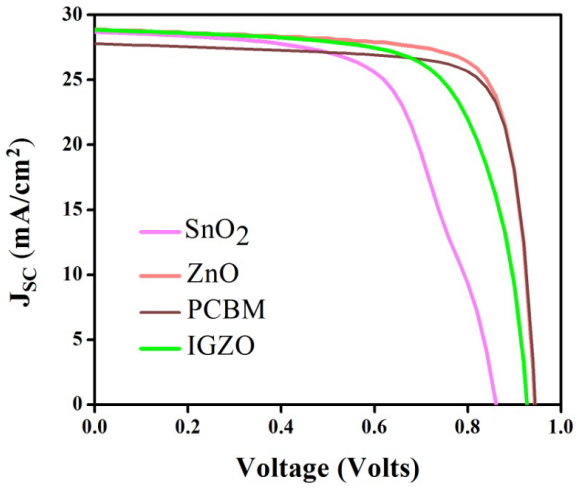

Fig. 5.21. Simulated J-V curve of different ETL on all-perovskite multijunction solar cell

In the case of SnO_2 the $E_{C\_ETL} - E_{V\_HTL}$ = 0.87 eV shows a lower V_{bi} as compared to other ETLs. In the case of IGZO, the V_{bi} value increases to 1.1 V. On the other hand, for PCBM and ZnO the E_{C_ETL} is -3.9 eV and -4.0 eV, respectively which is approximately equal to the E_C level of the wide bandgap perovskite layer. Thus, the V_{bi} increases in the case of PCBM and ZnO and reaches the value of 1.39 V and 1.18 V respectively. The current-voltage curve of all-perovskite multijunction solar cells with different ETL layers have been shown in Fig. 5.21. It can be seen from Table 5.12 that the lowest V_{OC} is found for SnO_2 whereas the highest V_{OC} is obtained for PCBM which significantly increases the PCE from 16.13% to 21.47%. Additionally, it is depicted from Fig. 5.19a, Fig. 5.19b, Fig. 5.19c, Fig. 5.19d and Table 5.10 that there is an important relationship is found between the V_{OC} and V_{bi}. This is attributed to the fact that the highest V_{bi} shows the highest V_{OC}. Moreover, it is found that to achieve high V_{OC} and PCE, E_{C_ETL} should not be deeper than E_{C_PVKs} to avoid V_{bi} loss. Hence, it can be revealed from the band alignment that the poor device performance of SnO_2 and IGZO is due to the lesser V_{bi}. It was expected from the band diagram, that PCBM and ZnO show similar device performance but PCBM has a low charge carrier's mobility which limits its performance. However, due to the higher V_{bi} =1.18 eV and higher

E_{C_ETL}-E_{V_ETL} =1.37 eV, the ZnO shows the best photovoltaic performance with a PCE of 22.04% as shown in Fig. 5.21 and Table 5.10.

5.2.2.2 Effect of absorber layer thickness on the photovoltaic performance of all-perovskite multijunction solar cell

The absorber layer plays a significant role in the photovoltaic performance of solar cells. To understand the effect of thickness of the perovskite absorber layer on the solar cell performance, the thickness of the wide bandgap absorber and low bandgap absorber layer have been changed from 100 nm to 800 nm. Initially, the thickness of $FAMASnGeI_3$ based layer has been changed from 100 nm to 800 nm consequently V_{OC} has been reduced from 1.01 V to 0.93 V and a significant increment of J_{SC} is observed from 25.10 mA /cm^2 to 29.51 mA/cm^2, whereas FF drops from 79.65 % to 73.18 % and efficiency reduces from 21.17 % to 20.37 % as given in Fig. 5.22a and Fig. 5.22b. The decrease in V_{OC} with respect to the thickness is attributed to the increase in J_0 which will enhance therecombination of charge carriers as given in Eq. 5.3

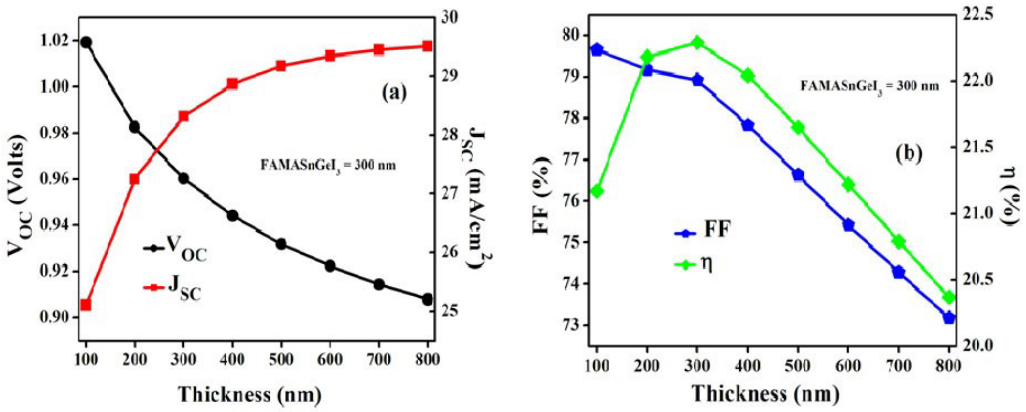

Fig. 5.22. Simulated results for $FAMASnGeI_3$ thickness keeping $CH_3NH_3GeI_3$ thickness constant at 400 nm (a) V_{OC} and J_{SC} (b) FF and η

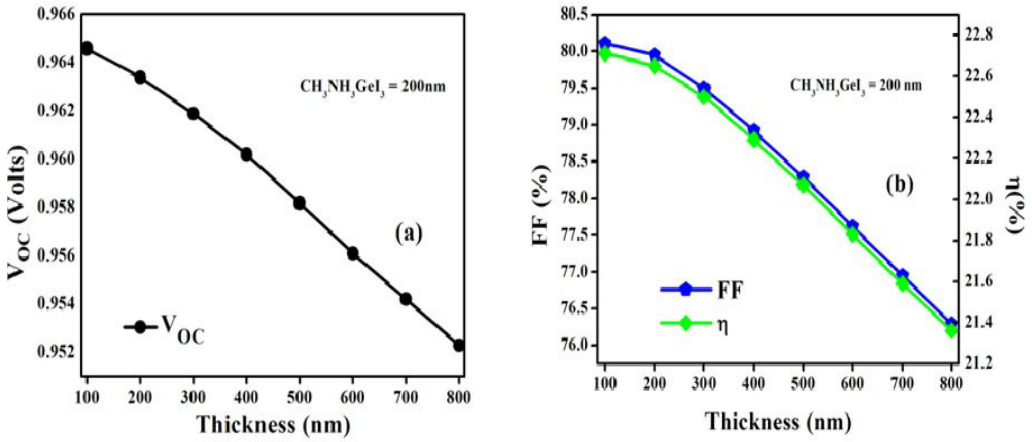

Fig. 5.23. Simulated results for $CH_3NH_3GeI_3$ thickness keeping $FAMASnGeI_3$ thickness constant at 300 nm (a) V_{OC} and J_{SC} (b) FF and η

This increase in J_{SC} is mainly due to the fact that the thick perovskite absorber layer allows more absorption of photons of high wavelength which will enhance carrier generation. The fill factor (FF) drops with the increase in thickness because as thickness increases it will increase the overall series resistance of the device. From Fig. 5.22b it has been obtained that after 300 nm thickness of $FAMASnGeI_3$ based layer, slight decrement of efficiency has been obtained. The maximum efficiency of 22.3% is achieved at the 300 nm thickness of $FAMASnGeI_3$. Hence, the optimum thickness for the $FAMASnGeI_3$ based perovskite layer is taken as 300 nm. Further, the thickness of $CH_3NH_3GeI_3$ based perovskite layer has been varied from 100 nm to 800 nm and the photovoltaic performance is measured. It is obtained from Fig. 5.23a that with the increase in thickness the V_{OC} decreases slightly however, a constant J_{SC} has been observed. Also, the slight decrement of FF and η is obtained as shown in Fig. 5.23b. It can be concluded from the results that as the thickness of the wide bandgap layer increases the performance of the device degrades. This is mainly due to the fact that as the thickness of the wide bandgap layer increases, the absorption in this layer increases and thus degrades the performance of the device. The thickness of the wide bandgap layer is thus kept at 200 nm for the rest of the studies shown in the chapter

$$V_{OC} = \frac{\eta' KT}{q} ln\left(\frac{J_{SC}}{J_o} + 1\right)$$

Eq. 5.3

5.2.2.3 Effect of absorber defect density on the photovoltaic performance of all-perovskite multijunction solar cell

Initially, the defect density of $FAMASnGeI_3$ based layer is varied from 1×10^{14} cm^{-3} to 1×10^{18} cm^{-3} keeping the defect density of $CH_3NH_3GeI_3$ constant at 1×10^{16} cm^{-3} as shown in Fig. 5.24a and Fig. 5.24b. It is obtained from Fig. 5.24a that as the defect density has been varied from 1×10^{14} cm^{-3} to 1×10^{18} cm^{-3} of $FAMASnGeI_3$ based layer the V_{OC} is reduced from 1.07 V to 0.85 V however, J_{SC} reduces from 28.32 mA/cm^2 to 24.74 mA/cm^2. Similarly, the FF and η have been decreased from 83.04 % to 54.80 % and 26.21 % to 12.08 % as shown in Fig. 5.24b. Hence, it can be concluded that as the defect density of the $FAMASnGeI_3$ layer increases, the device performance degrades significantly.

To obtain better device performance one should always keep the absorber layer defect density as low as possible. The defect density of the $FAMASnGeI_3$ layer is kept as 1×10^{14} cm^{-3} for the rest of the studies in the chapter.

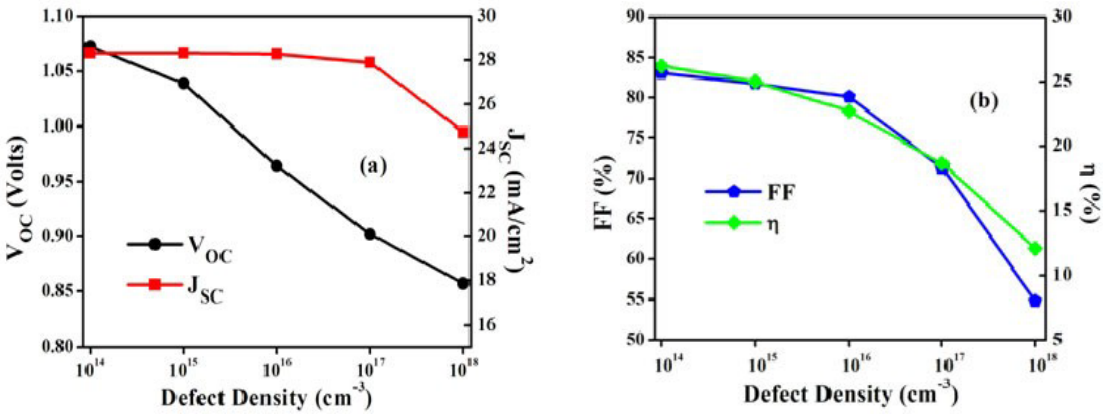

Fig. 5.24. Simulated results of $FAMASnGeI_3$ based defect density keeping the defect density of $CH_3NH_3GeI_3$ constant at 1×10^{16} cm^{-3}

Further, the defect density of the $CH_3NH_3GeI_3$ based layer is varied from 1×10^{14} cm^{-3} to 1×10^{18} cm^{-3} keeping the defect density of $FAMASnGeI_3$ constant at 1×10^{14} cm^{-3} as shown in Fig. 5.25a and Fig. 5.25b. It is observed from Fig. 5.25a that as the defect density of $CH_3NH_3GeI_3$ is varied from 1×10^{14} cm^{-3} to 1×10^{18} cm^{-3} the V_{OC} does not degrade much however the J_{SC} decreases from 28.33 mA/cm^2 to 24.59 mA/cm^2. Consequently, the FF reduces from 84.46% to 58.72% and the PCE decreases from 26.72% to 15.91%. It is figured out that as the defect density is increased it will create more recombination centres which will enhance the recombination of carriers within the absorber layer as well as reduce the lifetime of the carriers which degrades the device performance of the solar cell. The increase in recombination centres leads to a decrease in shunt resistance which reduces the V_{OC} of the device. It is found from the above study that when both the absorber layers have defect density is of the order of 1×10^{14} cm^{-3} the overall photovoltaic parameters improved to V_{OC} = 1.07 V, J_{SC} = 28.33 mA/cm^2 FF= 84.46 % and η = 26.72%.

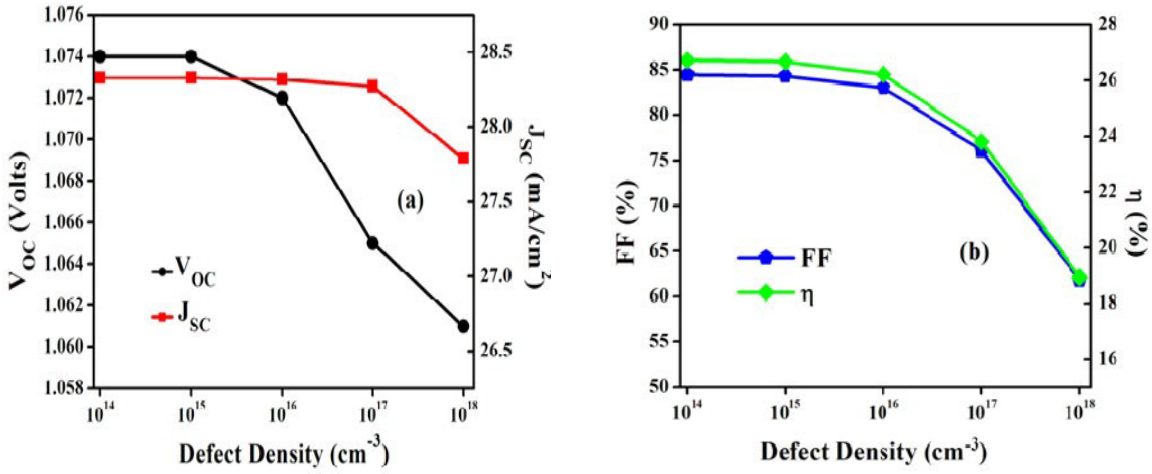

Fig. 5.25. Simulated results of $CH_3NH_3GeI_3$ based defect density keeping the defect density of $FAMASnGeI_3$ constant at 1×10^{14} cm^{-3}

5.2.2.4 Effect of front electrode work function on the device performance of all – perovskite multijunction solar cells

To the efficient collection of electrons from the absorber layer, the front contact plays a very important role. To facilitate the proper collection of electrons from the

front contact,the formation of an ohmic contact is crucial. To investigate the effect of front contact on the photovoltaic performance, the work function of the front electrode is varied from 3.8eV to 4.6 eV.

It is elucidated from Fig. 5.26a and Fig. 5.26b that as the front electrode metal work function increases up to 4.4 eV the photovoltaic parameters show good performance however on further increasing the work function of front contact, the device performance degrades rapidly as shown in Fig. 5.26a and Fig. 5.26b. The decrease in device performance with the work function of the front electrode can be explained using the band diagram as shown in Fig. 5.27a.

It is clear from the Fig. 5.27b that when the work function of front electrode is 4.4 eV, there exists a very small barrier, however, on further increasing the work function, the barrier increases which degrades the performance of the device as shown in Fig. 5.27c.

The V_{OC}, FF and η start degrading and reaches up to 1.02 V, 76.75% and 23.06 %, respectively. This is mainly due to the barrier created for electron transfer at the ETL/front electrode interface and will increase as the work function increases and in turn will degrade the photovoltaic performance. Hence, it is concluded that for the selection of front electrode material the work function of the front electrode should not exceed above 4.4 eV.

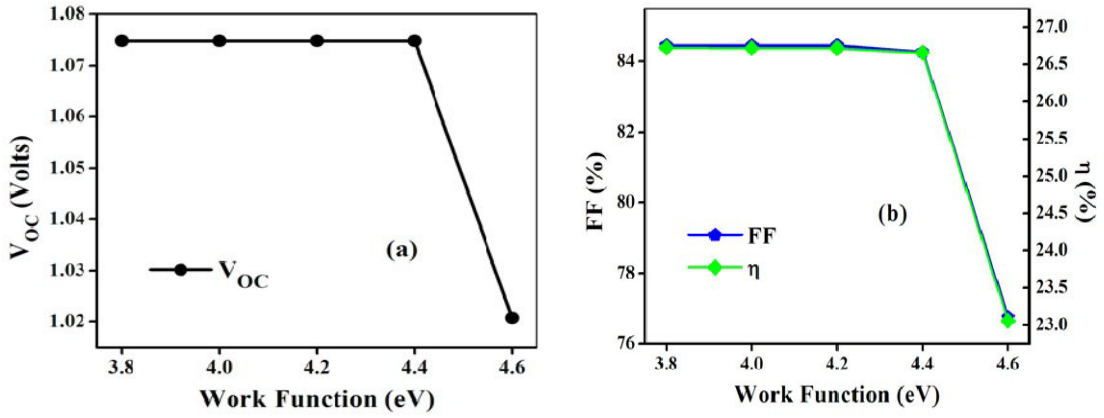

Fig. 5.26. Simulated results of front electrode work function on lead–free all-perovskite multi junction solar cells (a) V_{OC} and J_{SC} (b) FF and η

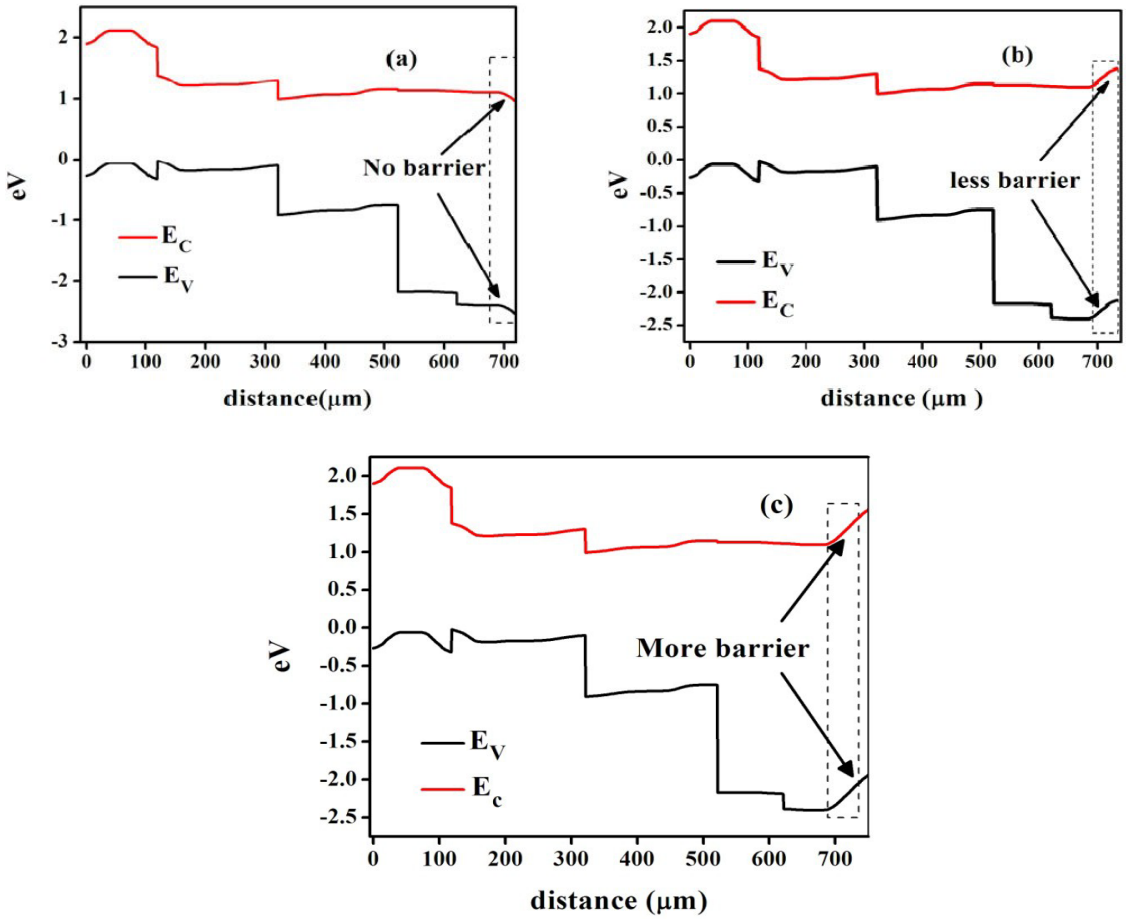

Fig. 5.27. Energy band diagram of lead-free all-perovskite multijunction solar cells (a) at 3.8 eV (b) at 4.4 eV (c) at 4.6 eV

The final J-V curve of Pb-free all-perovskite multijunction solar cell obtained using the optimized parameters is shown in Fig. 5.28. With the introduction of optimized ETL *i.e.,* ZnO, the thickness of the absorber layer *i.e.,* 300 nm for $FAMASnGeI_3$ and 200 nm for $CH_3NH_3GeI_3$, defect density of both absorber layer set to 1×10^{14} cm^{-3} and keeping the front electrode work function as 4.3 eV the final optimized parameters for all-perovskite multijunction solar cell is obtained as, V_{OC} =1.07 V, J_{SC} = 28.36 mA/cm^2, FF = 84.46 % and η = 26.72 % as shown in Table 5.11.

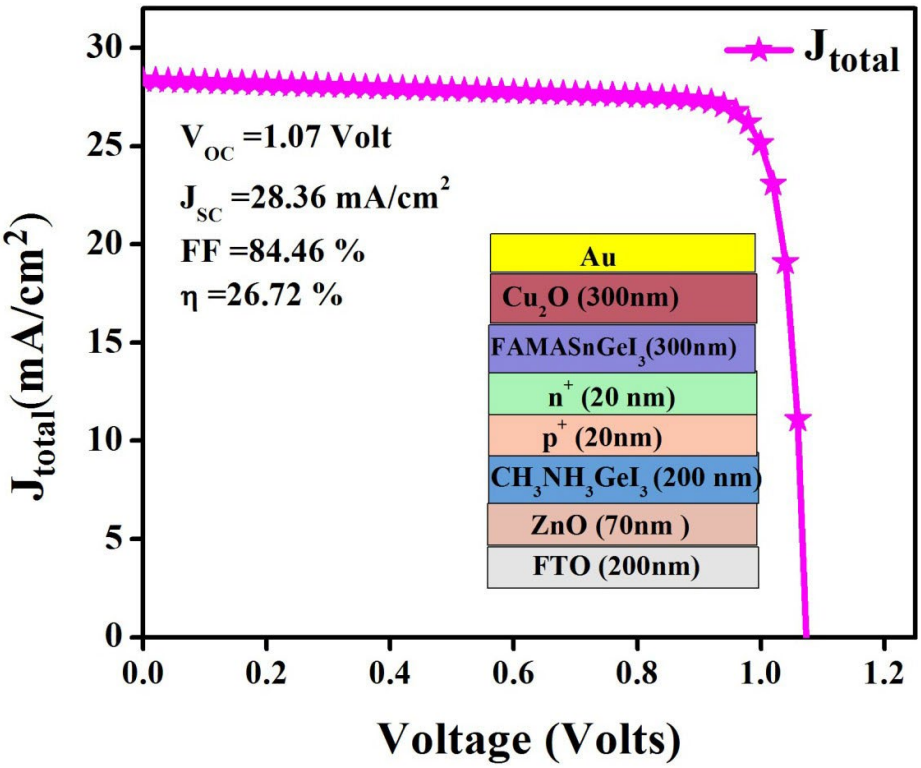

Fig. 5.28. Simulated J-V curve of optimized all–perovskite multijunction solar cell

Table 5.11 Final optimized device parameters obtained from simulation

Device parameters	Initial multijunction structure	After ETL optimization	Final optimized structure
V_{OC} (Volts)	0.93	0.94	1.07
J_{SC} (mA/cm^2)	28.85	28.87	28.36
FF (%)	72.40	77.83	84.46
η (%)	20.20	22.04	26.72

Table 5.12 shows the comparison of the simulated structure to the photovoltaic performance of APMJSC reported so far in the literature.

Table 5.12 Fabricated and simulated results of all –perovskite multijunction solar cell

Device Structure	V_{OC} (V)	J_{SC} (mA/cm^2)	FF (%)	η (%)	References
ITO/SnO_2/C60/LiF/ perovskite/spiro-OMeTAD/nc-Si:H/ncSiC_x/SiO_x C-Si/SiO_x/ITO/Ag	1.741	19.50	74.70	25.41	[144]
Si/nc-SiO_x:H/Perovskite/IZO	1.76	19.40	76.70	26.30	[145]
ITO/PEI/ETL/$CH_3NH_3PbI_3$/ Spiro-OMeTAD/Ag/FTO/c-TiO_2/mp-TiO_2/ $CH_3NH_3PbI_3$/Spiro-OMeTAD/Ag	1.89	6.61	56.00	7.00	[46]
ITO/PEDOT:PSS/$MAPbI_3$/PCBM/P3HT/$MAPbBr_3$/bl-TiO_2/FTO	1.95	8.40	66	10.80	[47]
ITO/NiO_x/$MAPb_{1-x}Sn_xI_3$/C60/ BisC60/ITO/PEDOT:PSS/ $MAPb(I_{0.6}Br_{0.4})_3$	1.98	12.70	73	18.40	[48]
Ag/BCP/C60/ $FA_{0.75}Cs_{0.25}Sn_{0.5}Pb_{0.5}I_3$/PEDOT:PSS/ITO/PCBM/ $FA_{0.83}Cs_{0.17}Pb(I_{0.5}Br_{0.5})_3$ /NiO/ITO	1.60	14.50	70	16.90	[49]
Ag/C60BCP/$(FASnI_3)_{0.6}(MAPbI_3)_{0.4}$:Cl/PEDOT:PSS/Ag/$MoO_x$ /ITO/C60/BCP/ $FA_{0.8}Cs_{0.2}Pb(I_{0.7}Br_{0.3})_3$/PTAA/ITO/glass	1.92	14.00	78.10	21.00	[50]
1.75eV(Wide),1.25eV(Low)	1.91	14.99	79.76	22.90	[51]
ITO/polyPFN/ $FA_{0.75}Cs_{0.25}Sn_{0.5}Pb_{0.5}I_3$ /LiF/C60/AZO/IZO/PEDOT:PS	1.88	16.00	77.00	21.30	[52]

S/ $FA_{0.725(1-x)}Cs_{0.2(1-x)+0.5x}$ $DMA_{0.5x}PbI_3$/C60/BCP/Au					
NiO/Top layer perovskite/PCBM/Recombination layer/PEDOT:PSS/Bottom layer perovskite/C60	-	-	-	29.8	[53]
Au/Cu_2O/FAMASnGeI$_3$/ $CH_3NH_3GeI_3$/ZnO/FTO	1.07	28.36	84.46	26.72	**[This Work]**

Table 5.12 demonstrates the fabricated and simulated results based on the tandem perovskite solar cell reported in the literature. This table reveals that there is a lot of potential for exploring all-perovskite multijunction solar cell to improve its photovoltaic performance. Also, the photovoltaic performance of all – perovskite multijunction solar cells is greatly dependent on the fabrication processing of charge recombination layers, additives used for hole transport layers, the technique through which layers are deposited. It can be viewed from the Table 5.12 that the proposed multijunction solar cell structure shows comparatively better PV performance than the other solar cell structures. Hence, by considering these fabrication constraints one can attain the highly efficient all-perovskite multijunction solar cell.

5.3 Conclusion

This section concludes that, as compared to the wide bandgap lead-free $CH_3NH_3GeI_3$ based perovskite structure, the narrow bandgap lead-free $CsSnGeI_3$ based perovskite structure shows superior PV performance. However, still, there is a limitation with respect to the S-Q limit owing to its lesser mobility of charge carriers of $CsSnGeI_3$ perovskite. It has been observed from the simulation results, that APMJSC exhibits superior PV performance as compare to standalone $CsSnGeI_3$ and $CH_3NH_3GeI_3$ based perovskite solar cells. Moreover, the impact of defect density of absorbers on the PV performance of APMJSC has also been studied. It is elucidated that an increment of ~ 3 % PCE is achieved at the defect density of 1×10^{14} cm^{-3}. Additionally, to acquire better PV performance the Φ_{BC} should be beyond 5 eV. The proposed multijunction perovskite solar cell possesses V_{OC}=1.20 V, J_{SC}=25.99

mA/cm^2, FF=85.31% and η= 26.64% which is far better than that of $CsSnGeI_3$ and $CH_3NH_3GeI_3$ based perovskite solar cell.

Furthermore, another all-perovskite multijunction solar cell with $CH_3NH_3GeI_3$ as wide bandgap layer and $FAMASnGeI_3$ as a narrow bandgap perovskite layer is also explored with STO as an initial ETL. Moreover, the device V_{OC} has been correlated with built-in potential with different electron transport layers. It is observed that ZnO shows better device efficiency as compare to STO as an electron transport layer. This is because ZnO provides better built-in voltage than that of STO which enhances the V_{OC} significantly. To further optimize the PV parameters the effect of thickness of the absorber layer is studied. The optimized thickness of $CH_3NH_3GeI_3$ and $FAMASnGeI_3$ based layer is found to be 200 nm and 300 nm respectively. Moreover, the optimized defect density of the perovskite absorber layer is 1×10^{14} cm^{-3} is obtained. Also, it has been found that the device PV parameters depend on the selection of the front electrode as well. In this study, the optimized work function of the front electrode is 4.3 eV. Hence, it can beconcluded that the multijunction device structure shows better photovoltaic performance as compare to the individual structure.

CHAPTER 6

CONCLUSION AND FUTURE SCOPE

CONCLUSION

This chapter discusses the significant conclusions drawn after analyzing the various Pb-free PSC structure. To optimize the performance of lead-free perovskite solar cells the numerical simulation method is adopted using SCAPS 1D. To design an effective solar cell, the impact of various material parameters on the perovskite solar cell performance is extremely essential. In the proposed work the lead-free methylammonium germanium halide ($CH_3NH_3GeI_3$) perovskite layer as a wide band gap layer is extensively used for the application of high efficiency multijunction solar cells. Similarly, $CsSnGeI_3$ and $FAMASnGeI_3$ as narrow bandgap perovskite layers are thoroughly used for high efficiency multijunction solar cells.

Initially, the optimization of standalone perovskite layers is performed by employing various charge transport layer. Further, the perovskite absorber layer defect density and the back contact electrode are optimized to achieve high device photovoltaic performance. The proposed research work provides the alternatives of lead-free wide and narrow bandgap perovskite layer, that will prove to be an efficient layer to achieve high device efficiency. For the wide bandgap applications, a lead-free double perovskite solar is also realized and optimized based on the charge transport layers and the thickness of the double perovskite solar cell.

Furthermore, the different hole transport layers are analyzed for wide and narrow bandgap perovskite layer combinations by correlating the built-in potential with the open circuit voltage of the solar cell. Using a similar concept, the suitable electron transport layer is also obtained. By optimizing these parameters, an efficient lead-free double-perovskite solar cell is realized.

To further improve the device performance of solar cell, a novel lead-free all-perovskite multijunction solar cell is also realized for the first time. In addition, the multijunction

solar cell is optimized based on the electron transport layer, hole transport layer and the thickness of the perovskite absorber layer. Further, the defect density and the front electrode work function of the all-perovskite multijunction solar cell are also optimized. The two different multijunction solar cell configurations are also proposed. The first multijunction configuration consists of a lead-free wide bandgap $CH_3NH_3GeI_3$ based perovskite structure, narrow bandgap lead-free $CsSnGeI_3$ based perovskite structure shows superior PV performance. It is observed that the all-perovskite multijunction solar cell exhibits superior photovoltaic performance as compare to their standalone counterparts. The multijunction solar cell is further optimized based on the defect density and it is elucidated that an increment of ~ 3 % PCE is achieved at the defect density of 1×10^{14} cm^{-3}. Additionally, to acquire a better PV performance the Φ_{BC} should be beyond 5 eV. The proposed multijunction perovskite solar cell possesses V_{OC}= 1.20 V, J_{SC}=25.99 mA/cm^2, FF=85.31% and η= 26.64% which is far better than that of $CsSnGeI_3$ and $CH_3NH_3GeI_3$ based and other perovskite solar cells.

The second lead- free all- perovskite multijunction solar cell is proposed and analysed with $CH_3NH_3GeI_3$ as wide bandgap perovskite layer and $FAMASnGeI_3$ as narrow bandgap perovskite layer. The effect of charge transport layer is also realized in which the Cu_2O as an HTL and ZnO as an ETL is obtained as an optimized charge transport layer. Further, the effect of thickness of both the perovskite absorber layer is studied and the optimized thickness of $CH_3NH_3GeI_3$ and $FAMASnGeI_3$ based layer is found to be 200 nm and 300 nm, respectively. The optimized value of defect density of the perovskite absorber layer is 1×10^{14} cm^{-3}. Also, it has been found that the device PV parameters depend on the selection of front electrode as well. In this study, the optimized work function of front electrode is found to be 4.3 eV. Hence, it is concluded that the multijunction solar cell device efficiency greatly depends on the selection of suitable charge transport layer, absorber layer thickness and its defect density, contacts work function and temperature of the solar cell. Hence, it is suggested that by optimizing these parameters one can attain highly efficient lead-free non-toxic solar cells. The results provide a significant insight for experimentalists to design an efficient lead-free perovskite solar cell.

FUTURE SCOPE OF THE WORK

In future, to further improve the device efficiency of lead-free perovskite solar cell the back surface field and interface recombination analysis can be analyzed. Since, the current lead-free double perovskite absorber layer $Cs_2AgBi_{0.75}Sb_{0.25}Br_6$ material is extremely less explored in the literature, hence one can perform some other analysis such as by implementing the interfacial and compositional engineering to surpass the device performance of $Cs_2AgBi_{0.75}Sb_{0.25}Br_6$ based perovskite layer beyond 20%. The numerical simulation method extended to some two-dimensional (2D) and three-dimensional (3D) platforms for the better understanding of the recombination mechanism, effect of grain boundaries and light scattering mechanisms on the device performance of lead-free perovskite solar cells. The role of crystallinity of the film in the perovskite structure is also determined by using nanowires, grain size and quantum dots configurations.

REFERENCES

[1] A. E. Becquere, “Mémoire sur le rayonnement chimique qui accompagne la lumière solaire et la lumière électrique / par,” *Comptes Rendus L’Academie des Sci.*, vol. 9, p. 145, 1839.

[2] International Renewable Energy Agency (IRENA), “Renewable Capacity 2019,” no. March, p. 3, 2019, [Online]. Available: www.irena.org/publications.

[3] International Renewable Energy Agency, “Renewable Energy Capacity Highlights,” *Irena*, vol. 00, no. March 2021, pp. 1–3, 2021, [Online]. Available: https://www.irena.org/publications/2021/March/Renewable-Capacity-Statistics-2021.

[4] A. B. J.J.M.Halls, C.A.Walsh, N.C. Greenham, E.A.Marseglia, R.H.Friend, S.C.Moratti, “Efficient photodiodes from interpenetrating polymer networks.,” *Letters to nature*, vol. 376, no. 6540. pp. 498–500, 1995.

[5] M. By, A. Vo, R. Hon, G. Ead, and F. R. S. Seep, “O f the Method of rendering very, fenfible the weak’ef Natural. . or Artificial Eleericity.”

[6] “Quantum Efficiency | PVEducation.” https://www.pveducation.org/pvcdrom/solar-cell-operation/quantum-efficiency (accessed Aug. 24, 2021).

[7] “Effect of parasitic Resistances | PVEducation.” https://www.pveducation.org/pvcdrom/solar-cell-operation/effect-of-parasitic-resistances (accessed Aug. 24, 2021).

[8] T. Ibn-Mohammed *et al.*, “Perovskite solar cells: An integrated hybrid lifecycle assessment and review in comparison with other photovoltaic technologies,” *Renew. Sustain. Energy Rev.*, vol. 80, no. June, pp. 1321–1344, 2017, doi: 10.1016/j.rser.2017.05.095.

[9] S. Rajput *et al.*, “Efficient Photodetector based on Sub-bandgap Transition in Silicon-ITO Distributed-Heterojunctions,” *J. Light. Technol.*, vol. 8724, no. c, pp. 1–1, 2021, doi: 10.1109/jlt.2021.3106451.

[10] P. Taylor, A. Gan, S. P. Singh, and N. Chaturvedi, “Influence of AlGaN and InGaN Back Barriers on the Influence of AlGaN and InGaN Back Barriers on the Performance of AlGaN / GaN HEMT,” no. June, pp. 37–41, 2015, doi: 10.1080/02564602.2015.1042930.

[11] A. W. Walker *et al.*, “Carrier recombination dynamics in Ga0.5In0.49P double hetrostructures to 500K,” *Semicunductor Science and Technology* (2020):055001.2020.

[12] Lenzmann, F.O., *et al.*, “Plasmonic light trapping in a a-SiH solar cell by front side Ag nanoparticle arrayA benchmark study” *Physica status solidi (a)* 210.8(2013):1571-1574.

[13] M. Lunz *et al.*, “Surface Plasmon Enhanced Energy Transfer between Donor and Acceptor CdTe Nanocrystal Quantum Dot Monolayers,” pp. 3341–3345, 2011.

[14] T. Jayenta, S. Singh, S. Masiul, and R. Get, “Flexible organic solar cells with graphene / PEDOT : PSS Schottky junction on PET substrates,” *Opt. - Int. J. Light Electron Opt.*, vol. 181, no. December 2018, pp. 984–992, 2019, doi: 10.1016/j.ijleo.2018.12.179.

[15] A. Kumar, S. Singh, V. Nand, G. Gupta, and B. Kumar, “Journal of Colloid and Interface Science Probing reversible photoluminescence alteration in CH 3 NH 3 PbBr 3 colloidal quantum dots for luminescence-based gas sensing application,” *J. Colloid Interface Sci.*, vol. 554, pp. 668–673, 2019, doi: 10.1016/j.jcis.2019.07.054.

[16] M. Mrinalini, N. Islavath, S. Prasanthkumar, and L. Giribabu, “Stipulating Low Production Cost Solar Cells All Set to Retail…!,” *Chem. Rec.*, vol. 19, no. 2, pp. 661–674, 2019, doi: 10.1002/tcr.201800106.

[17] A. Kojima, K. Teshima, Y. Shirai, and T. Miyasaka, “Organometal halide perovskites as visible-light sensitizers for photovoltaic cells,” *J. Am. Chem. Soc.*, vol. 131, no. 17, pp. 6050–6051, 2009, doi: 10.1021/ja809598r.

[18] J. H. Im, C. R. Lee, J. W. Lee, S. W. Park, and N. G. Park, “6.5% Efficient Perovskite Quantum-Dot-Sensitized Solar Cell,” *Nanoscale*, vol. 3, no. 10, pp. 4088–4093, 2011, doi: 10.1039/c1nr10867k.

[19] H. S. Kim *et al.*, “Lead iodide perovskite sensitized all-solid-state submicron thin film mesoscopic solar cell with efficiency exceeding 9%,” *Sci. Rep.*, vol. 2, pp. 1–7, 2012, doi: 10.1038/srep00591.

[20] Henry J. Snaith, Michael M. Lee, Joël Teuscher, Tsutomu Miyasaka, Takurou N. Murakami “Efficient hybrid solar cells based on meso-superstructured organometal halide perovskite,” vol. 338, no. November, pp. 643–648, 2012.

[21] J. H. Noh, S. H. Im, J. H. Heo, T. N. Mandal, and S. Il Seok, “Chemical management for colorful, efficient, and stable inorganic-organic hybrid

nanostructured solar cells," *Nano Lett.*, vol. 13, no. 4, pp. 1764–1769, 2013, doi: 10.1021/nl400349b.

[22] M. Boccard *et al.*, "Multiscale transparent electrode architecture for efficient light management and carrier collection in solar cells," *Nano Lett.*, vol. 12, no. 3, pp. 1344–1348, 2012, doi: 10.1021/nl203909u.

[23] S. N. Habisreutinger, T. Leijtens, G. E. Eperon, S. D. Stranks, R. J. Nicholas, and H. J. Snaith, "Carbon nanotube/polymer composites as a highly stable hole collection layer in perovskite solar cells," *Nano Lett.*, vol. 14, no. 10, pp. 5561–5568, 2014, doi: 10.1021/nl501982b.

[24] N. J. Jeon, J. H. Noh, Y. C. Kim, W. S. Yang, S. Ryu, and S. Il Seok, "Solvent engineering for high-performance inorganic-organic hybrid perovskite solar cells," *Nat. Mater.*, vol. 13, no. 9, pp. 897–903, 2014, doi: 10.1038/nmat4014.

[25] N. J. Jeon *et al.*, "Compositional engineering of perovskite materials for high-performance solar cells," *Nature*, vol. 517, no. 7535, pp. 476–480, 2015, doi: 10.1038/nature14133.

[26] E. H. Jung *et al.*, "Efficient, stable and scalable perovskite solar cells using poly(3-hexylthiophene)," *Nature*, vol. 567, no. 7749, pp. 511–515, 2019, doi: 10.1038/s41586-019-1036-3.

[27] H. S. Kim, A. Hagfeldt, and N. G. Park, "Morphological and compositional progress in halide perovskite solar cells," *Chem. Commun.*, vol. 55, no. 9, pp. 1192–1200, 2019, doi: 10.1039/c8cc08653b.

[28] "best-research-cell-efficiencies-rev210726.pdf." .

[29] X. Liu *et al.*, "Improvemnet of Cs-(FAPbI3)0.85(MAPbBr3)0.15D Quality via DMSO-Molecule-Control to Increase the Efficiency and Boost the Long-Term Stability of 1 cm 2 Sized Planar Perovskite Solar Cells," vol. 85, pp. 1–10, 2019, doi: 10.1002/solr.201800338.

[30] O. Schultz, "Beschreibung einiger ," *15*, pp. 652–656, 1900.

[31] H. S. Jung, G. S. Han, N. G. Park, and M. J. Ko, "Flexible Perovskite Solar Cells," *Joule*, vol. 3, no. 8, pp. 1850–1880, 2019, doi: 10.1016/j.joule.2019.07.023.

[32] C. Li, X. Lu, W. Ding, L. Feng, Y. Gao, and Z. Guo, "Formability of ABX 3 (X = F, Cl, Br, I) halide perovskites," *Acta Crystallogr. Sect. B Struct. Sci.*, vol. 64, no. 6, pp. 702–707, 2008, doi: 10.1107/S0108768108032734.

[33] F. Jiang *et al.*, "A two-terminal perovskite/perovskite tandem solar cell," *J. Mater. Chem. A*, vol. 4, no. 4, pp. 1208–1213, 2016, doi: 10.1039/c5ta08744a.

[34] J. H. Heo and S. H. Im, “CH3NH3PbBr3–CH3NH3PbI3Perovskite–Perovskite Tandem Solar Cells with Exceeding 2.2 V Open Circuit Voltage,” *Adv. Mater.*, vol. 28, no. 25, pp. 5121–5125, 2016, doi: 10.1002/adma.201501629.

[35] A. Rajagopal *et al.*, “Highly Efficient Perovskite–Perovskite Tandem Solar Cells Reaching 80% of the Theoretical Limit in Photovoltage,” *Adv. Mater.*, vol. 29, no. 34, pp. 1–10, 2017, doi: 10.1002/adma.201702140.

[36] G. E. Eperon *et al.*, “Perovskite-perovskite tandem photovoltaics with optimized band gaps,” *Science (80-.).*, vol. 9717, no. 6314, pp. 1–10, 2016.

[37] D. Zhao *et al.*, “Efficient two-terminal all-perovskite tandem solar cells enabled by high-quality low-bandgap absorber layers,” *Nat. Energy*, vol. 3, no. 12, pp. 1093–1100, 2018, doi: 10.1038/s41560-018-0278-x.

[38] J. Tong *et al.*, “Carrier lifetimes of >1 ms in Sn-Pb perovskites enable efficient all-perovskite tandem solar cells,” *Science (80-.).*, vol. 364, no. 6439, pp. 475–479, 2019, doi: 10.1126/science.aav7911.

[39] A. Ben Or and J. Appelbaum, “Dependence of multi-junction solar cells parameters on concentration and temperature,” *Sol. Energy Mater. Sol. Cells*, vol. 130, pp. 234–240, 2014, doi: 10.1016/j.solmat.2014.07.010.

[40] J. Madan, Shivani, R. Pandey, and R. Sharma, “Device simulation of 17.3% efficient lead-free all-perovskite tandem solar cell,” *Sol. Energy*, vol. 197, no. November 2019, pp. 212–221, 2020, doi: 10.1016/j.solener.2020.01.006.

[41] N. K. Noel *et al.*, “Lead-free organic-inorganic tin halide perovskites for photovoltaic applications,” *Energy Environ. Sci.*, vol. 7, no. 9, pp. 3061–3068, 2014, doi: 10.1039/c4ee01076k.

[42] L. Ma, F. Hao, C. C. Stoumpos, B. T. Phelan, M. R. Wasielewski, and M. G. Kanatzidis, “Carrier Diffusion Lengths of over 500 nm in Lead-Free Perovskite CH3NH3SnI3 Films,” *J. Am. Chem. Soc.*, vol. 138, no. 44, pp. 14750–14755, 2016, doi: 10.1021/jacs.6b09257.

[43] A. Iefanova, N. Adhikari, A. Dubey, D. Khatiwada, and Q. Qiao, “Lead free CH3NH3SnI3 perovskite thin-film with p-type semiconducting nature and metal-like conductivity,” *AIP Adv.*, vol. 6, no. 8, 2016, doi: 10.1063/1.4961463.

[44] U. Mandadapu, S. V. Vedanayakam, K. Thyagarajan, M. R. Reddy, and B. J. Babu, “Design and simulation of high efficiency tin halide perovskite solar cell,” *Int. J. Renew. Energy Res.*, vol. 7, no. 4, pp. 1604–1612, 2017.

[45] F. Anwar, R. Mahbub, S. S. Satter, and S. M. Ullah, “Effect of Different HTM

Layers and Electrical Parameters on ZnO Nanorod-Based Lead-Free Perovskite Solar Cell for High-Efficiency Performance," *Int. J. Photoenergy*, vol. 2017, 2017, doi: 10.1155/2017/9846310.

[46] F. Baig, Y. H. Khattak, B. Marí, S. Beg, A. Ahmed, and K. Khan, "Efficiency Enhancement of CH3NH3SnI3 Solar Cells by Device Modeling," *J. Electron. Mater.*, vol. 47, no. 9, pp. 5275–5282, 2018, doi: 10.1007/s11664-018-6406-3.

[47] K. Kumari, A. Jana, A. Dey, T. Chakrabarti, and S. K. Sarkar, "Lead free CH3NH3SnI3 based perovskite solar cell using ZnTe nano flowers as hole transport layer," *Opt. Mater. (Amst).*, vol. 111, no. November 2020, p. 110574, 2021, doi: 10.1016/j.optmat.2020.110574.

[48] S. Shao *et al.*, "Highly Reproducible Sn-Based Hybrid Perovskite Solar Cells with 9% Efficiency," *Adv. Energy Mater.*, vol. 8, no. 4, 2018, doi: 10.1002/aenm.201702019.

[49] M. H. Kumar *et al.*, "Lead-free halide perovskite solar cells with high photocurrents realized through vacancy modulation," *Adv. Mater.*, vol. 26, no. 41, pp. 7122–7127, 2014, doi: 10.1002/adma.201401991.

[50] C. C. Stoumpos *et al.*, "Hybrid germanium iodide perovskite semiconductors: Active lone pairs, structural distortions, direct and indirect energy gaps, and strong nonlinear optical properties," *J. Am. Chem. Soc.*, vol. 137, no. 21, pp. 6804–6819, 2015, doi: 10.1021/jacs.5b01025.

[51] T. Krishnamoorthy *et al.*, "Lead-free germanium iodide perovskite materials for photovoltaic applications," *J. Mater. Chem. A*, vol. 3, no. 47, pp. 23829–23832, 2015, doi: 10.1039/c5ta05741h.

[52] P. P. Sun, Q. S. Li, L. N. Yang, and Z. S. Li, "Theoretical insights into a potential lead-free hybrid perovskite: Substituting Pb2+ with Ge2+," *Nanoscale*, vol. 8, no. 3, pp. 1503–1512, 2016, doi: 10.1039/c5nr05337d.

[53] A. A. Kanoun, M. B. Kanoun, A. E. Merad, and S. Goumri-Said, "Toward development of high-performance perovskite solar cells based on CH3NH3GeI3 using computational approach," *Sol. Energy*, vol. 182, no. February, pp. 237–244, 2019, doi: 10.1016/j.solener.2019.02.041.

[54] N. Lakhdar and A. Hima, "Electron transport material effect on performance of perovskite solar cells based on CH3NH3GeI3," *Opt. Mater. (Amst).*, vol. 99, no. October 2019, p. 109517, 2020, doi: 10.1016/j.optmat.2019.109517.

[55] A. Hima and N. Lakhdar, "Enhancement of efficiency and stability of

CH3NH3GeI3 solar cells with CuSbS2," *Opt. Mater. (Amst).*, vol. 99, no. November 2019, p. 109607, 2020, doi: 10.1016/j.optmat.2019.109607.

[56] Y. Rong, L. Liu, A. Mei, X. Li, and H. Han, "Beyond efficiency: The challenge of stability in mesoscopic perovskite solar cells," *Adv. Energy Mater.*, vol. 5, no. 20, pp. 1–16, 2015, doi: 10.1002/aenm.201501066.

[57] T. Leijtens, G. E. Eperon, N. K. Noel, S. N. Habisreutinger, A. Petrozza, and H. J. Snaith, "Stability of metal halide perovskite solar cells," *Adv. Energy Mater.*, vol. 5, no. 20, pp. 1–23, 2015, doi: 10.1002/aenm.201500963.

[58] N. P. P. and X. C. Z. Ming-Gang Ju, Min Chen, Yuanyuan Zhou, Jun Dai, Liang Ma, "Towards eco friendly and stable perovskite material for photovoltiacs.pdf." pp. 1231–1241, 2018.

[59] Q. Tai *et al.*, "Efficient and stable perovskite solar cells prepared in ambient air irrespective of the humidity," *Nat. Commun.*, vol. 7, pp. 1–8, 2016, doi: 10.1038/ncomms11105.

[60] T. Niu *et al.*, "High performance ambient-air-stable FAPbI 3 perovskite solar cells with molecule-passivated Ruddlesden-Popper/3D heterostructured film," *Energy Environ. Sci.*, vol. 11, no. 12, pp. 3358–3366, 2018, doi: 10.1039/c8ee02542h.

[61] S. S. Mali, H. Kim, H. H. Kim, S. E. Shim, and C. K. Hong, "Nanoporous p-type NiOx electrode for p-i-n inverted perovskite solar cell toward air stability," *Mater. Today*, vol. 21, no. 5, pp. 483–500, 2018, doi: 10.1016/j.mattod.2017.12.002.

[62] J. . T. K. and M. G. K. In Chung, Jung-Hwan Song, Jino Im, John Androulakis, Christos D. Malliakas, Hao Li, Arthur J. Freeman, "CsSnI3 Semiconductor or metal high electrical conductivity and strong near infrared photoluminscence from a single material high hole mobility and phase transitions." pp. 8579–8587, 2012.

[63] T. Zhang, H. Li, H. Ban, Q. Sun, Y. Shen, and M. Wang, "Efficient CsSnI3-based inorganic perovskite solar cells based on a mesoscopic metal oxide framework via incorporating a donor element," *J. Mater. Chem. A*, vol. 8, no. 7, pp. 4118–4124, 2020, doi: 10.1039/c9ta11794f.

[64] K. P. Marshall, M. Walker, R. I. Walton, and R. A. Hatton, "Enhanced stability and efficiency in hole-transport-layer-free CsSnI 3 perovskite photovoltaics," *Nat. Energy*, vol. 1, no. 12, pp. 1–9, 2016, doi: 10.1038/nenergy.2016.178.

[65] M. Chen *et al.*, "Highly stable and efficient all-inorganic lead-free perovskite solar cells with native-oxide passivation," *Nat. Commun.*, vol. 10, no. 1, pp. 1–8, 2019, doi: 10.1038/s41467-018-07951-y.

[66] Raghvendra, R. R. Kumar, and S. K. Pandey, “Performance evaluation and material parameter perspective of eco-friendly highly efficient CsSnGeI3 perovskite solar cell,” *Superlattices Microstruct.*, vol. 135, no. May, p. 106273, 2019, doi: 10.1016/j.spmi.2019.106273.

[67] T. Islam, R. Jani, A. F. Islam, K. Shorowordi, and S. Chowdhury, “Investigation of CsSn0.5Ge0.5I3 on a Si/tandem solar device utilizing SCAPS simulation,” vol. 68, no. 2, pp. 618–625, 2021.

[68] A. N. El-Shazly, M. Y. Rezk, K. M. Gameel, and N. K. Allam, “Electrospun Lead-Free All-Inorganic Double Perovskite Nanofibers for Photovoltaic and Optoelectronic Applications,” *ACS Appl. Nano Mater.*, vol. 2, no. 11, pp. 7085–7094, 2019, doi: 10.1021/acsanm.9b01613.

[69] N. Ito *et al.*, “Mixed Sn-Ge Perovskite for Enhanced Perovskite Solar Cell Performance in Air,” *J. Phys. Chem. Lett.*, vol. 9, no. 7, pp. 1682–1688, 2018, doi: 10.1021/acs.jpclett.8b00275.

[70] T. Minemoto *et al.*, “Theoretical analysis of band alignment at back junction in Sn–Ge perovskite solar cells with inverted p-i-n structure,” *Sol. Energy Mater. Sol. Cells*, vol. 206, no. June 2019, p. 110268, 2020, doi: 10.1016/j.solmat.2019.110268.

[71] W. Gao *et al.*, “High-Quality Cs2AgBiBr6 Double Perovskite Film for Lead-Free Inverted Planar Heterojunction Solar Cells with 2.2 % Efficiency,” *ChemPhysChem*, vol. 19, no. 14, pp. 1696–1700, 2018, doi: 10.1002/cphc.201800346.

[72] M. Pantaler *et al.*, “Hysteresis-Free Lead-Free Double-Perovskite Solar Cells by Interface Engineering,” *ACS Energy Lett.*, vol. 3, no. 8, pp. 1781–1786, 2018, doi: 10.1021/acsenergylett.8b00871.

[73] K. M. and D. C. L. Martina Pantaler1, Selina Olthof2, “Bismuth-Antimony mixed double perovskite Cs2AgBi1-xSbxBr6 in solar cells,” *MRS Adv.*, vol. 4(64), no. May, pp. 3545–3552, 2019, doi: 10.1557/adv.201.

[74] M. A. M. H. Asif Hossain, Muhammad Mahmudul Hasan, MD Shaikh Rahman, “Fully Lead-Free All Perovskite Tandem Solar Cell with improoved device efficiency.pdf.” pp. 1221–1224, 2020.

[75] Q. Jiang *et al.*, “Surface passivation of perovskite film for efficient solar cells,” *Nat. Photonics*, vol. 13, no. 7, pp. 460–466, 2019, doi: 10.1038/s41566-019-0398-2.

[76] “Jiang, Qi, *et al.*, "Planar-Structure Perovskite Solar Cells with Efficiency beyond 21%”. *Advanced Materials* 29.46(2017):1703852

[77] Y. Wang *et al.*, “Thermodynamically stabilized b-CsPbI3–based perovskite solar cells with efficiencies >18%,” *Science (80-.).*, vol. 365, no. 6453, pp. 591–595, 2019, doi: 10.1126/science.aav8680.

[78] L. Zhou *et al.*, “Interface engineering of low temperature processed all-inorganic CsPbI 2 Br perovskite solar cells toward PCE exceeding 14%,” *Nano Energy*, vol. 60, no. March, pp. 583–590, 2019, doi: 10.1016/j.nanoen.2019.03.081.

[79] J. Y. Seo *et al.*, “Novel p-dopant toward highly efficient and stable perovskite solar cells,” *Energy Environ. Sci.*, vol. 11, no. 10, pp. 2985–2992, 2018, doi: 10.1039/c8ee01500g.

[80] G. Sathiyan *et al.*, “Dual effective dopant based hole transport layer for stable and efficient perovskite solar cells,” *Nano Energy*, vol. 72, no. March, p. 104673, 2020, doi: 10.1016/j.nanoen.2020.104673.

[81] M. Wang, H. Wang, W. Li, X. Hu, K. Sun, and Z. Zang, “Defect passivation using ultrathin PTAA layers for efficient and stable perovskite solar cells with a high fill factor and eliminated hysteresis,” *J. Mater. Chem. A*, vol. 7, no. 46, pp. 26421–26428, 2019, doi: 10.1039/c9ta08314f.

[82] K. M. Reza *et al.*, “Tailored PEDOT:PSS hole transport layer for higher performance in perovskite solar cells: Enhancement of electrical and optical properties with improved morphology,” *J. Energy Chem.*, vol. 44, pp. 41–50, 2020, doi: 10.1016/j.jechem.2019.09.014.

[83] J. H. Heo, H. J. Han, D. Kim, T. K. Ahn, and S. H. Im, “Hysteresis-less inverted CH3NH3PbI3 planar perovskite hybrid solar cells with 18.1% power conversion efficiency,” *Energy Environ. Sci.*, vol. 8, no. 5, pp. 1602–1608, 2015, doi: 10.1039/c5ee00120j.

[84] J. C. Yu *et al.*, “Highly efficient and stable inverted perovskite solar cell employing PEDOT:GO composite layer as a hole transport layer,” *Scientific Reports*, vol. 8, no. 1. 2018, doi: 10.1038/s41598-018-19612-7.

[85] D. Liu *et al.*, “Improved performance of inverted planar perovskite solar cells with F4-TCNQ doped PEDOT:PSS hole transport layers,” *J. Mater. Chem. A*, vol. 5, no. 12, pp. 5701–5708, 2017, doi: 10.1039/C6TA10212C.

[86] M. K. Sardashti, M. Zendehdel, N. Y. Nia, D. Karimian, and M. Sheikhi, “High Efficiency MAPbI3 Perovskite Solar Cell Using a Pure Thin Film of

Polyoxometalate as Scaffold Layer," *ChemSusChem*, vol. 10, no. 19, pp. 3773–3779, 2017, doi: 10.1002/cssc.201701027.

[87] Y. Zhang, M. Elawad, Z. Yu, X. Jiang, J. Lai, and L. Sun, "Enhanced performance of perovskite solar cells with P3HT hole-transporting materials: Via molecular p-type doping," *RSC Adv.*, vol. 6, no. 110, pp. 108888–108895, 2016, doi: 10.1039/c6ra21775c.

[88] J. Cao, B. Wu, J. Peng, X. Feng, C. Li, and Y. Tang, "Copper-copper iodide hybrid nanostructure as hole transport material for efficient and stable inverted perovskite solar cells," *Sci. China Chem.*, vol. 62, no. 3, pp. 363–369, 2019, doi: 10.1007/s11426-018-9386-5.

[89] W. Y. Chen *et al.*, "Low-cost solution-processed copper iodide as an alternative to PEDOT:PSS hole transport layer for efficient and stable inverted planar heterojunction perovskite solar cells," *J. Mater. Chem. A*, vol. 3, no. 38, pp. 19353–19359, 2015, doi: 10.1039/c5ta05286f.

[90] G. A. Sepalage *et al.*, "Copper(I) Iodide as Hole-Conductor in Planar Perovskite Solar Cells: Probing the Origin of J-V Hysteresis," *Adv. Funct. Mater.*, vol. 25, no. 35, pp. 5650–5661, 2015, doi: 10.1002/adfm.201502541.

[91] J. A. Christians, R. C. M. Fung, and P. V. Kamat, "An inorganic hole conductor for Organo-lead halide perovskite solar cells. improved hole conductivity with copper iodide," *J. Am. Chem. Soc.*, vol. 136, no. 2, pp. 758–764, 2014, doi: 10.1021/ja411014k.

[92] Y. G. Kim, K. C. Kwon, Q. Van Le, K. Hong, H. W. Jang, and S. Y. Kim, "Atomically thin two-dimensional materials as hole extraction layers in organolead halide perovskite photovoltaic cells," *J. Power Sources*, vol. 319, pp. 1–8, 2016, doi: 10.1016/j.jpowsour.2016.04.032.

[93] N. Arora *et al.*, "Perovskite solar cells with CuSCN hole extraction layers yield stabilized efficiencies greater than 20%," *Science (80-.).*, vol. 358, no. 6364, pp. 768–771, 2017, doi: 10.1126/science.aam5655.

[94] I. S. Yang, S. Lee, J. Choi, M. T. Jung, J. Kim, and W. I. Lee, "Enhancement of open circuit voltage for CuSCN-based perovskite solar cells by controlling the perovskite/CuSCN interface with functional molecules," *J. Mater. Chem. A*, vol. 7, no. 11, pp. 6028–6037, 2019, doi: 10.1039/c8ta12217b.

[95] M. Jung *et al.*, "Thermal Stability of CuSCN Hole Conductor-Based Perovskite Solar Cells," *ChemSusChem*, vol. 9, no. 18, pp. 2592–2596, 2016, doi:

10.1002/cssc.201600957.

[96] J. Kim, Y. Lee, A. J. Yun, B. Gil, and B. Park, “Interfacial Modification and Defect Passivation by the Cross-Linking Interlayer for Efficient and Stable CuSCN-Based Perovskite Solar Cells,” *ACS Appl. Mater. Interfaces*, vol. 11, no. 50, pp. 46818–46824, 2019, doi: 10.1021/acsami.9b16194.

[97] S. Ye *et al.*, “CuSCN-Based Inverted Planar Perovskite Solar Cell with an Average PCE of 15.6%,” *Nano Lett.*, vol. 15, no. 6, pp. 3723–3728, 2015, doi: 10.1021/acs.nanolett.5b00116.

[98] Neophytou, Marios, et al. "Enhancing the charge extraction and stability of perovskite solar cells using strontium titanate (SrTiO3) electron transport layer." ACS Applied Energy Materials 2.11 (2019): 8090-8097.

[99] A. Bera, K. Wu, A. Sheikh, E. Alarousu, O. F. Mohammed, and T. Wu, “Perovskite oxide SrTiO3 as an efficient electron transporter for hybrid perovskite solar cells,” *Journal of Physical Chemistry C*, vol. 118, no. 49. pp. 28494–28501, 2014, doi: 10.1021/jp509753p.

[100] S. Shi *et al.*, “Room-temperature synthesized SnO2 electron transport layers for efficient perovskite solar cells,” *RSC Adv.*, vol. 9, no. 18, pp. 9946–9950, 2019, doi: 10.1039/c8ra10603g.

[101] J. P. Correa Baena *et al.*, “Highly efficient planar perovskite solar cells through band alignment engineering,” *Energy Environ. Sci.*, vol. 8, no. 10, pp. 2928–2934, 2015, doi: 10.1039/c5ee02608c.

[102] Z. Rao *et al.*, “Revisit of amorphous semiconductor InGaZnO4: A new electron transport material for perovskite solar cells,” *J. Alloys Compd.*, vol. 789, pp. 276–281, 2019, doi: 10.1016/j.jallcom.2019.02.311.

[103] S. Ke *et al.*, “Pulsed laser deposition of amorphous InGaZnO4 as an electron transport layer for perovskite solar cells,” *J. Adv. Dielectr.*, vol. 9, no. 5, pp. 1–6, 2019, doi: 10.1142/S2010135X19500425.

[104] F. Xia *et al.*, “Efficiency Enhancement of Inverted Structure Perovskite Solar Cells via Oleamide Doping of PCBM Electron Transport Layer,” *ACS Appl. Mater. Interfaces*, vol. 7, no. 24, pp. 13659–13665, 2015, doi: 10.1021/acsami.5b03525.

[105] A. Guchhait *et al.*, “p-i-n Structured Semitransparent Perovskite Solar Cells with Solution-Processed Electron Transport Layer,” *J. Electron. Mater.*, no. 0123456789, 2021, doi: 10.1007/s11664-021-09104-2.

[106] N. A. A. Malek *et al.*, “Enhanced Charge Transfer in Atom-Thick 2H–WS2

Nanosheets' Electron Transport Layers of Perovskite Solar Cells," *Sol. RRL*, vol. 4, no. 10, pp. 1–11, 2020, doi: 10.1002/solr.202000260.

[107] X. L. Yijie Wang, Min Zhong, Wu Wang, Qiuyu Wang, Wenduo Wu, "Effects of ZnSe modification on the perovskitefilms and perovskite solarcells based on ZnO nanorod arrays.pdf." p. 143552, 2019.

[108] Niu, Haihong, et al. "Magnetron sputtered ZnO electron transporting layers for high performance perovskite solar cells." Dalton Transactions 50.19 (2021): 6477-6487.

[109] N. A. K. and J. O. Muhammad Imran, Hikmet Coskun, Furkan H. Isikgor, Li Bichen, "Highly efficient and stable inverted perovskite solar cell with 2D ZnSe depositing using a thermal evaporator for electon collection." p. 22713, 2018.

[110] N.-G. P. Namyoung Ahn , Dae-Yong Son , In-Hyuk Jang , Seong Min Kang , Mansoo Choi , "Highly Reproducible Perovskite Solar Cells with Average Efficiency of 18.3% and Best Efficiency of 19.7% Fabricated via Lewis Base adduct of lead(II) iodide." pp. 8696–8699, 2015.

[111] S. I. S. Woon Seok Yang, Jun Hong Noh, Nam Joong Jeon, Young Chan Kim, Seungchan Ryu, Jangwon Seo, "High-performance photovoltaic perovskite layers fabricated through coherent perfect absorber," vol. 348, no. 6240. pp. 1234–1237, 2015.

[112] J. H. Heo *et al.*, "Planar CH3NH3PbI3 perovskite solar cells with constant 17.2% average power conversion efficiency irrespective of the scan rate," *Adv. Mater.*, vol. 27, no. 22, pp. 3424–3430, 2015, doi: 10.1002/adma.201500048.

[113] Y. H. J. Ma, Jie Su, Zhenhua Lin, Long Zhou, Jian He, Jincheng Zhang, S. Liu, Jingjing Chang, "Improve the Oxide Perovskite Heterojunction Contact for Low Temperature High efficiency and stable all-inorganic CsPbI2Br perovskite solar cell." p. 104241, 2019.

[114] S. R. Guchhait, Asim, Goutam kumar Dallapati , aiananad Gopalan, Firgaus zbin suhaimi, Tapas DAS, V.G. Vasavi Dutt, Nimai Mishra, Chandreshwar Mahata, Avishek kumar, "p-i-n Structured Semitransparent Perovskite Solar Cells without solution processd electron transport layer." pp. 1543–186X, 2021.

[115] A. F. Palmstrom *et al.*, "Enabling Flexible All-Perovskite Tandem Solar Cells," *Joule*, vol. 3, no. 9, pp. 2193–2204, 2019, doi: 10.1016/j.joule.2019.05.009.

[116] A. Singh and A. Gagliardi, "Efficiency of all-perovskite two-terminal tandem solar cells: A drift-diffusion study," *Sol. Energy*, vol. 187, no. March, pp. 39–46, 2019,

doi: 10.1016/j.solener.2019.05.006.

[117] M. Burgelman, P. Nollet, and S. Degrave, “Modelling polycrystalline semiconductor solar cells,” *Thin Solid Films*, vol. 361, pp. 527–532, 2000, doi: 10.1016/S0040-6090(99)00825-1.

[118] M. Burgelman, K. Decock, S. Kheli, and A. Abass, “Author ’ s personal copy Advanced electrical simulation of thin fi lm solar cells,” *Thin Solid Films*, vol. 535, pp. 296–301, 2013.

[119] P. Shrivastava, “First-principles study of Cs 2 Ti 1 − x M x Br 6 (M = Pb , Sn) and numerical simulation of the solar cells based on,” no. November 2020, pp. 8049–8060, 2021, doi: 10.1002/er.6339.

[120] H. Zhou *et al.*, “Interface engineering of highly efficient perovskite solar cells,” *Science (80-.).*, vol. 345, no. 6196, pp. 542–546, 2014.

[121] M. I. Hossain, F. H. Alharbi, and N. Tabet, “Copper oxide as inorganic hole transport material for lead halide perovskite based solar cells,” *Sol. Energy*, vol. 120, pp. 370–380, 2015, doi: 10.1016/j.solener.2015.07.040.

[122] U. Mandadapu, S. V. Vedanayakam, and K. Thyagarajan, “Simulation and Analysis of Lead based Perovskite Solar Cell using SCAPS-1D,” *Indian J. Sci. Technol.*, vol. 10, no. 11, pp. 1–8, 2017, doi: 10.17485/ijst/2017/v10i11/110721.

[123] Y. H. Khattak, F. Baig, H. Toura, S. Beg, and B. M. Soucase, “CZTSe Kesterite as an Alternative Hole Transport Layer for MASnI3 Perovskite Solar Cells,” *J. Electron. Mater.*, vol. 48, no. 9, pp. 5723–5733, 2019, doi: 10.1007/s11664-019-07374-5.

[124] F. Azri, A. Meftah, N. Sengouga, and A. Meftah, “Electron and hole transport layers optimization by numerical simulation of a perovskite solar cell,” *Sol. Energy*, vol. 181, no. February, pp. 372–378, 2019, doi: 10.1016/j.solener.2019.02.017.

[125] M. S. Jamal *et al.*, “Effect of defect density and energy level mismatch on the performance of perovskite solar cells by numerical simulation,” *Optik (Stuttg).*, vol. 182, no. December 2018, pp. 1204–1210, 2019, doi: 10.1016/j.ijleo.2018.12.163.

[126] E. Lim, K. A. Peterson, G. M. Su, and M. L. Chabinyc, “Thermoelectric Properties of Poly(3-hexylthiophene) (P3HT) Doped with 2,3,5,6-Tetrafluoro-7,7,8,8-tetracyanoquinodimethane (F4TCNQ) by Vapor-Phase Infiltration,” *Chem. Mater.*, vol. 30, no. 3, pp. 998–1010, 2018, doi: 10.1021/acs.chemmater.7b04849.

[127] C. Zuo and L. Ding, “Solution-Processed Cu2O and CuO as Hole Transport Materials for Efficient Perovskite Solar Cells,” *Small*, vol. 11, no. 41, pp. 5528–5532, 2015, doi: 10.1002/smll.201501330.

[128] A. K. Kang, M. H. Zandi, and N. E. Gorji, “Simulation analysis of graphene contacted perovskite solar cells using SCAPS-1D,” *Opt. Quantum Electron.*, vol. 51, no. 4, pp. 1–9, 2019, doi: 10.1007/s11082-019-1802-3.

[129] R. Teimouri and R. Mohammadpour, “Potential application of CuSbS2 as the hole transport material in perovskite solar cell: A simulation study,” *Superlattices Microstruct.*, vol. 118, pp. 116–122, 2018, doi: 10.1016/j.spmi.2018.03.079.

[130] S. Bishnoi and S. K. Pandey, “Device performance analysis for lead-free perovskite solar cell optimisation,” *IET Optoelectron.*, vol. 12, no. 4, pp. 185–190, 2018, doi: 10.1049/iet-opt.2017.0135.

[131] K. Sobayel *et al.*, “A comprehensive defect study of tungsten disulfide (WS2) as electron transport layer in perovskite solar cells by numerical simulation,” *Results Phys.*, vol. 12, no. December 2018, pp. 1097–1103, 2019, doi: 10.1016/j.rinp.2018.12.049.

[132] J. A. Owolabi, M. Y. Onimisi, J. A. Ukwenya, A. B. Bature, and U. R. Ushielepan, “Investigating the Effect of ZnSe (ETM) and Cu 2 O (HTM) on Absorber Layer on the Performance of Pervoskite Solar Cell Using SCAPS-1D To cite this article :,” vol. 8, no. 1, pp. 8–18, 2020, doi: 10.11648/j.ajpa.20200801.12.

[133] S. I. Rahman, S. Faisal, S. Ahmed, and T. I. Dhrubo, “A comparative study on different HTMs in perovskite solar cell with ZnOS electron transport layer,” *5th IEEE Reg. 10 Humanit. Technol. Conf. 2017, R10-HTC 2017*, vol. 2018-Janua, no. October 2018, pp. 546–550, 2018, doi: 10.1109/R10-HTC.2017.8289019.

[134] A. Haddout, M. Fahoume, A. Qachaou, A. Raidou, M. Lharch, and N. Elharfaoui, “Influence of composition ratio on the performances of kesterite solar cell with double CZTS layers—A numerical approach,” *Sol. Energy*, vol. 189, no. July, pp. 491–502, 2019, doi: 10.1016/j.solener.2019.07.098.

[135] D. K. Maram, M. Haghighi, O. Shekoofa, H. Habibiyan, and H. Ghafoorifard, “A modeling study on utilizing ultra-thin inorganic HTLs in inverted p–n homojunction perovskite solar cells,” *Sol. Energy*, vol. 213, no. November 2020, pp. 1–12, 2021, doi: 10.1016/j.solener.2020.11.009.

[136] S. Z. Haider, H. Anwar, and M. Wang, “A comprehensive device modelling of perovskite solar cell with inorganic copper iodide as hole transport material,”

Semicond. Sci. Technol., vol. 33, no. 3, 2018, doi: 10.1088/1361-6641/aaa596.

[137] M. Shasti and A. Mortezaali, "Numerical Study of Cu2O, SrCu2O2, and CuAlO2 as Hole-Transport Materials for Application in Perovskite Solar Cells," *Phys. Status Solidi Appl. Mater. Sci.*, vol. 216, no. 18, pp. 1–10, 2019, doi: 10.1002/pssa.201900337.

[138] D. Jalalian, A. Ghadimi, and A. Kiani, "Modeling of a high performance bandgap graded Pb-free HTM-free perovskite solar cell," *Eur. Phys. J. Appl. Phys.*, vol. 87, no. 1, p. 10101, 2019, doi: 10.1051/epjap/2019190095.

LIST OF PUBLICATIONS

JOURNAL PUBLICATIONS (SCI)

- Singh, N., Agarwal, A., & Agarwal, M. (2020) Numerical simulation of highly efficient lead-free all-perovskite tandem solar cell, *Solar Energy*, *208*, 399-410.
- Singh, N., Agarwal, A., & Agarwal, M. (2021) Numerical simulation of highly efficient lead-free perovskite layers for the application of all-perovskite tandem solar cell, *Superlattices and Microstructures,*149,106750.
- Singh, N., Agarwal, A., & Agarwal, M. (2021) Performance evaluation of lead-free double-perovskite solar cell, *Optical Materials*,114,110964.

CONFERENCE PUBLICATIONS (SCOPUS)

- Singh, N., Agarwal, A., & Agarwal, M. (2020) Computational analysis of cesium based inorganic perovskite solar cells using SCAPS-1D, *AIP Conference Proceedings*. Vol. 2265. No. 1. AIP Publishing LLC.
- Singh, N., Agarwal, A., & Agarwal, M. (2020, May). Numerical analysis of lead-free methyl ammonium tin halide perovskite solar cell. In *AIP Conference Proceedings* Vol. 2220, No. 1, p. 130033. AIP Publishing LLC.
- Singh N., Agarwal A., Agarwal M. (2021) Performance Improvement of Inorganic Lead-Free Perovskite Solar Cell. In: Arunachalam V., Sivasankaran K. (eds) Microelectronic Devices, Circuits and Systems. ICMDCS 2021. Communications in Computer and Information Science, vol 1392. Springer, Singapore.